A HIGH RESOLUTION INVESTIGATION

OF VACUUM ULTRAVIOLET WAVELENGTH STANDARDS

by

Roy Charles Preston, B.Sc.

A Thesis submitted for the degree of

Doctor of Philosophy of the University

of London

National Physical Laboratory,
Teddington, Middlesex.

September, 1972.

A B S T R A C T

The design and construction of a 1.5m focal length high resolution echelle spectrometer is described for use in the vacuum ultraviolet between λ200 and λ100nm. The instrument has been constructed and used at the National Physical Laboratory to obtain the experimental results presented for the shift and width of GeII wavelength standards with change in spectral source operating conditions.

Particular care has been taken in the optical design in order to minimise residual geometrical aberrations by the use of ray-tracing. A realisable resolving power, not corrected for source or slit widths, of between 2.7 and $4.0.10^5$ in the wavelength region λ120 to λ250nm is demonstrated. As a result of the careful design and construction, wavelength shifts are presented which have an estimated uncertainty of about ± 3 parts in 10^8 or less.

A liquid nitrogen cooled hollow cathode lamp is described which has been constructed and used to observe the suitability of GeII emission lines, at about λ160nm, as secondary wavelength standards. Data on the wavelength shifts and widths are presented for carrier gas pressure and discharge current changes as well as other important source characteristics. A discussion of the possible mechanisms responsible for the observations is presented.

C O N T E N T S

INTRODUCTION

The physical and chemical properties of an atom are determined by the electrons which surround the nucleus. The radiation emitted by the atom, as a result of electronic transitions, provides one of the most powerful methods of investigating electronic structure. Study of the nucleus is also possible through its interaction with the electrons giving rise to hyperfine structure and isotope shift in the atomic emission lines.

Hence, considerable effort has always been put into the study of atomic spectroscopy. Different regions of the electromagnetic spectrum contain information about electronic structure. The visible and ultraviolet regions contain transitions between states of low principal quantum numbers in the neutral and first few ionised atomic species. This information is fundamental to the theories of electronic structure in the atom.

Measurement of wavelengths is a direct method of determining the electronic energy level separation in the atom. Extension to the highest accuracies available enables the nuclear structure to be investigated. Techniques of measurement in the visible region have been developed using high resolution interferometers to such a high degree that the wavelength of the orange line of ^{86}Kr is the present primary standard of length. This is accepted as a standard because of the belief that atomic structure does not differ between laboratories. However, this assumes that observations of the emission are under conditions where the atom is not perturbed by its microscopic or macroscopic environment. Hence, very careful investigations of such an emission spectral line are undertaken before it can be adopted as a wavelength standard.

The most common high resolution instrument used in the visible,

for spectral line studies and wavelength measurement, is the Fabry Perot interferometer. Degradation of the finesse with decrease in wavelength results from the difficulty of producing optical plates flat enough and the increased absorption in the high reflectivity thin film coating. Such interferometers decrease in resolving power in the ultraviolet and are not usable below λ200nm as a high resolution instrument. Two-beam interferometers, such as the Michelson, are very powerful instruments in the visible and, as will be discussed later, are the only ones potentially usable below λ200nm. The vacuum ultraviolet, below λ200nm, is the regime of concave grating spectroscopic instruments of large focal length (up to 10m) in order to realise high resolving powers, rarely exceeding 3.10^5.

Wavelength standards in the vacuum ultraviolet are at present based on either the Ritz combination principle or on measurements against accurate longer wavelength lines in different orders of a concave grating spectrograph. Both methods are susceptible to systematic errors. The Ritz combination principle, described by Edlén (1963), requires wavelength determinations over a large wavelength range. Different sources and instruments are often used for the different regions which can lead to systematic measurement errors. Comparison of wavelengths in different orders using a concave grating spectrograph can lead to coincidence errors when the grating is imperfect as described in previous work by Preston (1970a), which is reprinted in the Appendix.

As described in Chapter 4, the state of wavelength standards in the vacuum ultraviolet are not at all satisfactory. For example, germanium emission lines will be considered in detail and it will be shown that the present values of wavelengths are only very indirectly traceable to the ^{86}Kr primary standard. All recent measurements rely

on the determinations of wavelengths which were undertaken ten years ago. Many spectral emission sources employed in more recent term analysis and wavelength measurements are frequently completely different in character from the sources originally used for the reference wavelength measurements.

MacAdam (1936) used a reflection echelon to measure some copper lines down to λ148.8nm, this work represents the only direct interferometric wavelength measurement ever made. Pery-Thorne (1962) used a modified Michelson interferometer to obtain fringes down to about λ150nm, but this was not for wavelength measurements. The problems of optical surface production of suitable quality on a transmitting material, such as LiF, MgF_2 or CaF_2, have always been severe. Considerable advances have been made in recent years in the production, polishing and handling techniques applicable to these crystals and it now appears possible to achieve the desired tolerances on a beam splitter for a two beam interferometer. The research programme at N.P.L. is aimed at producing a Michelson interferometer, using such a beam splitter, to measure directly wavelengths between λ200 and λ100nm with respect to the ^{86}Kr primary standard, or any other suitable standard.

If absolute wavelength measurements are to be made it is first necessary to evaluate the suitability of spectral lines as secondary standards. Evaluation of the broadening and shift of lines with source excitation conditions is essential. It seems reasonable that as all spectroscopic equipment at present employed in the λ100 - λ200nm region use diffraction gratings; initial work using a very high resolution spectrometer should provide information on the suitability of spectral lines as secondary standards. Final absolute wavelength and very small wavelength shift measurements using the interferometer would be undertaken on spectral lines found to be

suitable.

The vacuum ultraviolet region requires very high resolving power instruments. To obtain a constant uncertainty in energy level separation the demand on wavelength measurement accuracy increases with decrease in wavelength according to the relation:-

$$\Delta\lambda = -\lambda^2 \Delta\bar{\nu}$$

where $\bar{\nu}$ and λ are the wavenumber and wavelength respectively. Thus the experimental limitations are more severe. Usually, concave grating instruments are constructed; of large radius of curvature to give sufficient dispersion and enable the grating width to be large enough to realise high resolving power, and still satisfy the basic relationship derived by Namioka (1959) for the optimum width of the grating.

For a 150mm wide grating with 1200 lines/mm, blazed for say λ450nm used in the 3rd order at λ150nm, the theoretical resolving power would be about 6.10^5. Such a grating would be used in, for example, a 21ft spectrometer where the optimum grating width is about 270mm, larger than the proposed grating. In order to realise such a resolving power the grating quality should be of the highest possible standard. Learner (1968) gives a graph of realisable resolving power versus wavelength for echelle gratings; indicating that below λ200nm the resolving power drops very sharply. Echelle gratings are usually of higher quality than concave gratings, hence it is unlikely that the figure of 6.10^5 could be realised. The enormous size of a 21ft spectrometer would lead to considerable dimensional stability problems when dealing with shifts of, say, 1 part in 10^7.

Although there is considerable advantage in the vacuum ultraviolet from using only one or two reflecting components; it was decided that, in view of the high reflectivity coatings now available and the dimensional stability problems, a higher resolution should be

obtainable using a plane echelle grating in a smaller instrument.

The purpose of this thesis is to describe the optical and mechanical design of a 1.5m echelle spectrometer. Optical design considerations are demonstrated by the use of ray-tracing in order to realise a resolving power of between 2.7 and $4.0.10^5$ in the region λ120 to λ250nm. The results of careful mechanical design of the spectrometer are shown by the reproducibility of the instrumental function to $\pm$2% over a period of many months. Capability of measurement of wavelength shifts smaller than 1 part in 10^7 is demonstrated by the investigation of GeII wavelength standards, at about λ160nm, emitted by a liquid nitrogen cooled hollow cathode lamp. A discussion of the results of shift measurements, which are considerably smaller than any previous reported results, will be given, which provides valuable information on the operating conditions of the lamp for realising wavelengths which are perturbed least by the lamp environment.

CHAPTER 1

THE SPECTROMETER DESIGN - OPTICAL

The basic optical design principles are explained in this chapter. Reasons for using an echelle grating are examined and the general optical system requirements are discussed. Optimisation of the main optical configuration is undertaken by the use of a ray-tracing computer programme written especially for this purpose. Finally, the predisperser design is considered in detail.

1.1 The echelle

Consider diffraction by a stepped diffraction grating, as shown in figure 1. It can be shown that:-

$$t\cos\theta\left(\cos\phi + \cos\phi'\right) - s\left(\sin\phi + \sin\phi'\right) = m\lambda \quad (1)$$

describes the relation between the angle of diffraction, ϕ, angle of incidence, ϕ', both measured in the same direction, wavelength, λ, order, m, step length, t, and height, s, where θ is the angle of incidence in the x-y plane. Now if the distance between the apices of the steps is d then:-

$$d\sin\psi = t, \quad d\cos\psi = s$$

where ψ is called the blaze angle defined from figure 1; and if we consider rays in the plane normal to the rulings where $\theta = 0$, equation (1) reduces to:-

$$d\left\{\sin\left(\psi - \phi'\right) + \sin\left(\psi - \phi\right)\right\} = m\lambda \quad (2)$$

which is the usual diffraction grating equation.

At this stage it is interesting to see from equation (1) that the $\cos\theta$ term introduces a rotation of the image of an object slit. If an object point on the entrance slit moves away from the centre then equation (1) shows that because θ increases and λ, m, t, s and ϕ' are constants then ϕ must change. Differentiating equation (1), for the case when $\phi' = 0$, with respect to θ yields:-

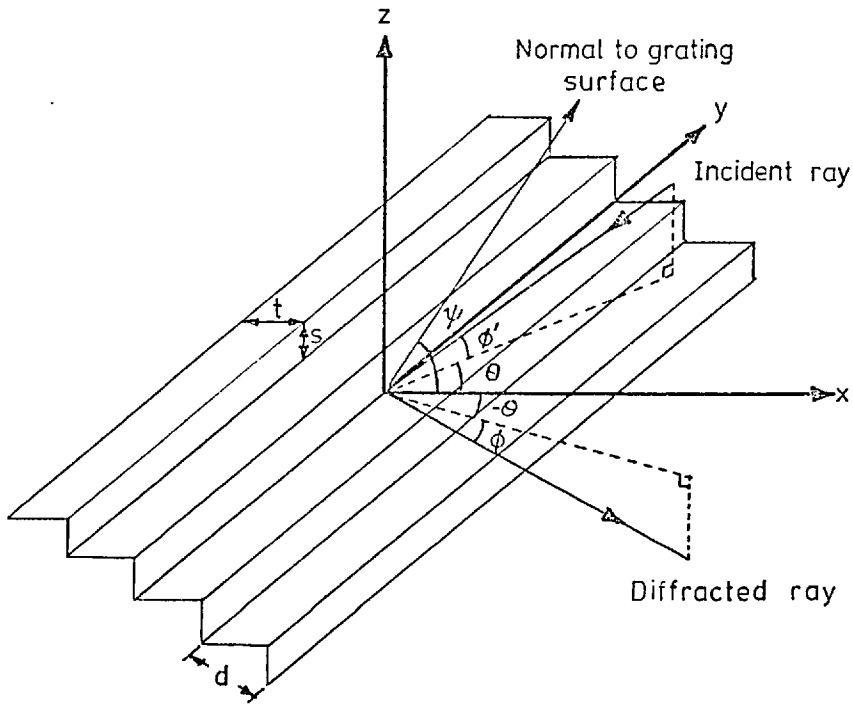

FIGURE 1. THE DIFFRACTION GRATING

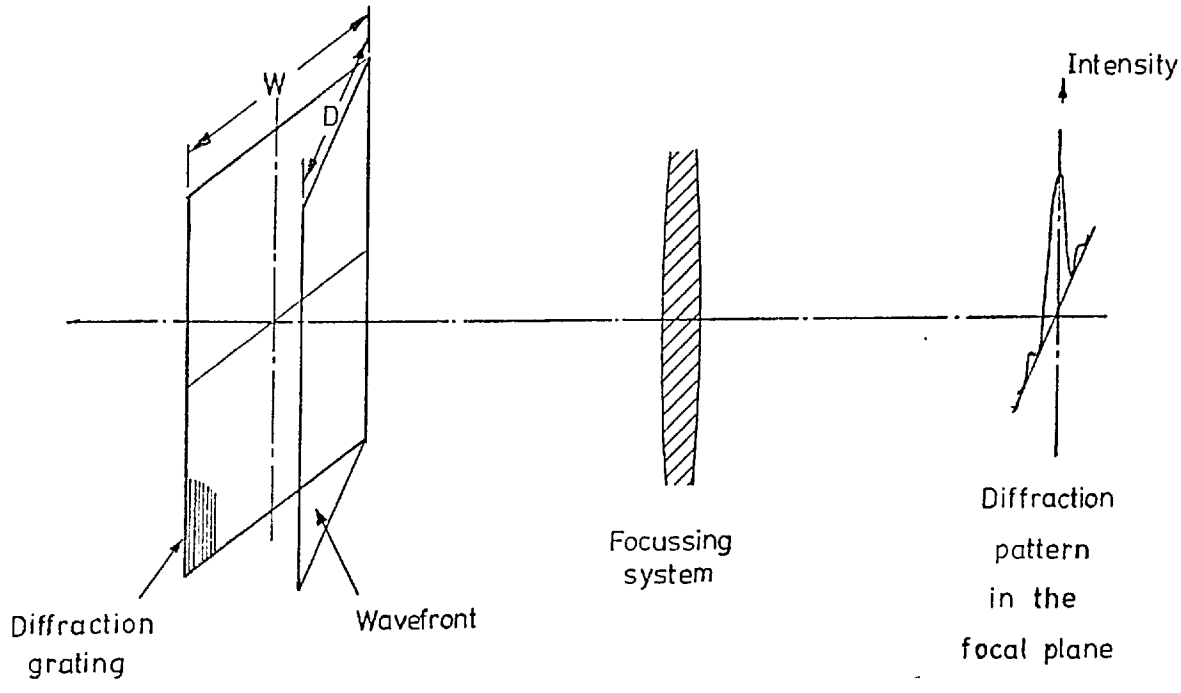

FIGURE 2. DIFFRACTED WAVEFRONT AND PATTERN IN THE FOCAL PLANE

$$\frac{d\phi}{d\theta} = \frac{-t \sin\theta \,(1 + \cos\phi)}{t \cos\theta \sin\phi + s \cos\phi} \qquad (3)$$

An increase in θ must be associated with a change in the angle of diffraction. In general, it is found that the curvature of the image, from a straight entrance slit, is concave to increase in wavelength. This is one of the two reasons for using curved slits in a plane grating spectrometer, as will be discussed later.

The theoretical maximum resolving power of a diffraction grating at wavelength, λ, is given in terms of the Rayleigh criterion as $\frac{\lambda}{\Delta\lambda}$, where $\Delta\lambda$ is the wavelength difference between the central maximum and the first minimum in the diffraction pattern of the projected grating aperture, as shown in figure 2. For the case of a grating used in autocollimation, the effective grating width, D, is:-

$$D = W \cos\alpha \qquad (4)$$

where W is the total grating width and $\alpha = \psi - \phi$, which is the angle of diffraction measured from the grating normal. The angular distance between central maximum and first minimum in the diffraction pattern is $\Delta\alpha$, where:-

$$\Delta\alpha = \frac{\lambda}{D} \qquad (5)$$

and, from the grating equation (2), the inverse angular dispersion is:-

$$\frac{\Delta\lambda}{\Delta\alpha} = \frac{d \cos\alpha}{m} \qquad (6)$$

From equations (4), (5) and (6) the maximum resolving power becomes:-

$$\frac{\lambda}{\Delta\lambda} = \frac{2W \sin\alpha}{\lambda} \qquad (7)$$

Equation (7) shows that high resolving power is obtained, for a particular wavelength, by either a) using a large grating width, or b) employing a large angle of diffraction. The inverse angular

dispersion is given from equations (6) and (2) as:-

$$\frac{\Delta\lambda}{\Delta\alpha} = \frac{\lambda}{2\tan\alpha}$$

Thus, large angles of diffraction lead to smaller inverse angular dispersion, and hence a smaller instrument focal length can be employed.

Factors a) and b), above, are satisfied by the use of an echelle grating. Typically, this may have 300 lines/mm used at an angle of diffraction between 50° and 70°. Correspondingly high blaze angle, ψ, and extremely good groove formation leads to very high efficiencies. A grating width between 100mm and 250mm can be employed to satisfy a).

At a wavelength of λ546.1nm a typical resolving power, for a 254mm wide echelle blazed at 63°, is, from equation (7), approximately 8.10^{5}. Theoretical resolving power varies inversely with wavelength and hence at about λ100nm we would expect a theoretical resolving power in excess of 4.10^{6}. However, this has never been realised in practice. We will see that in the present instrument the limitation is set by the aberrations of the optics.

1.2 General

A plane grating is usually illuminated in parallel light and therefore requires a collimating and focussing mirror.

One of the earliest mountings ever employed, and still widely used, is that of Ebert (1889) which consists of a single large concave mirror used both as collimator and camera mirror. From a simple ray diagram of such a system it is seen that extreme rays from the entrance slit traverse paths which are anti-symmetrical about the longitudinal axis of the spectrograph. This is the fundamental reason for the success of this type of mounting, because the coma introduced at each mirror reflection tends to cancel out.

Another version of the single mirror system is the Ebert-Fastie mount, described by Fastie (1952) and Jarrell (1955), which uses what is called the 'up and over' system where the slit is in the plane at right angles to the dispersion plane and above or below the grating. This produces a wide spectrum on the opposite side of the grating. One of the major disadvantages of such a system used as a spectrometer or monochromator is that the exit slit must be rotated with change of wavelength such that the slit rotation, Φ, angle of diffraction, α, and the angle between incident and diffracted beams in a direction parallel to the grating rulings, θ, are related by:-

$$\Phi = \tan^{-1}\left(2 \tan\alpha \tan\theta\right)$$

When a high blaze angle grating is used, better correction of the residual coma can be obtained using two separate mirrors, as discovered by Czerny and Turner (1930). It is this configuration that forms the basis of the instrument that has been constructed at N.P.L.

Employing a high blaze angle echelle, and consequently high diffracted orders, necessitates the limitation of the bandwidth of the radiation incident on the echelle in order to prevent overlapping orders. The free spectral range, which defines the required bandwidth, is given approximately by:-

$$\frac{\lambda}{m}$$

Thus at λ120nm, where this is most important, the free spectral range, where orders can be about 45, is as small as 2.7nm. A bandwidth less than this value is allowed into the spectrometer by the use of an off-axis Wadsworth mounted concave grating used as a predisperser.

It is useful, at this stage, to draw up a table of order, inverse dispersion, theoretical resolving power and free spectral range as a function of wavelength for the spectrometer. Such a table

is shown in table 1, for a 1.5m focal length instrument and using a 63° blaze, 303 lines/mm, echelle.

Attainment of the theoretical resolving power, given in table 1, is not possible as will be discussed later. To approach this value as closely as possible a ray tracing computer programme was developed by Preston (1970b) in order to optimise the optical configuration. The results already published by Preston (1970c) refer to calculations for a 52° blaze echelle. Both these references are reprinted in the Appendix. This particular grating was an early echelle which suffered from very prominent Rowland ghosts and a Fourier transform analysis of the wavefront exhibited an asymmetrical line profile, as shown in the previous publication by Preston (1970a). The ray-tracing results for a new 63° blaze echelle are outlined in section 1.3, but most parameters in the configuration are unchanged. The wavefront obtained from this echelle in a Twyman-Green interferometer was found to be extremely good and no calculations have been done on the wavefront because they would reflect the other optical element imperfections in the interferometer, rather than those of the grating. When a grating exhibits such a good wavefront in the visible, it is doubtful what value a Fourier transform analysis of its wavefront would be, when it is intended to use it in the vacuum ultraviolet. Apart from this, the observed profile is the convolution of many other aberrations, all of which are optimised in the final focussing of the exit slit, none of which are involved in the Fourier transform calculations.

In order to observe very small wavelength shifts, less than 1 part in 10^7, good mechanical and thermal stability are required. Hence, the optics are mounted on an optical bench within the vacuum tank, and linked to a concrete block through bellows in the tank. The whole system is supported on anti-vibrational mounts. A polythene sheet tent encloses the vacuum tank and concrete block but excludes the pumps.

Wavelength λ nm	Order m	Inverse Linear Dispersion nm/mm	Theoretical Resolving Power x 10^5	Free Spectral Range nm
600	9	0.1081	5.86	75.0
550	10	0.0914	6.51	61.1
500	11	0.0831	7.16	50.0
450	13	0.0511	8.46	37.5
400	14	0.0607	9.11	30.8
350	16	0.0534	10.42	23.3
300	19	0.0411	12.37	16.6
250	23	0.0324	14.97	11.4
200	28	0.0304	18.23	7.4
150	38	0.0206	24.74	4.1
100	56	0.0152	36.45	1.8

TABLE 1. Spectral order, m, focal plane inverse linear dispersion, theoretical resolving power and free spectral range as a function of wavelength for a 206mm wide 63.43° blaze echelle with 316 grooves/mm in a 1.5m focal length spectrometer. The echelle angle of incidence has been altered to bring the diffracted order, which most nearly satisfies the blaze condition, to the exit slit.

Temperature control of the air around the spectrometer using heaters and circulating fans maintains the temperature stable to about $\pm 0.03^{\circ}C$.

1.3 Ray-tracing

The optical configuration of the main optics, shown in figure 3, was optimised using a ray-tracing programme specifically written for this purpose. The calculations are outlined in an N.P.L. report and publication (Preston (1970b,c)). The results published refer to calculations for the 52° blaze echelle.

The ray-tracing serves to minimise the residual coma in the focal plane image by optimising the off-axis angle of the focussing mirror and examine the suitability of curved slits. Details of the optical configuration, such as separation of the mirrors, angle between incident and diffracted beams, are unchanged for a different blaze angle grating. The calculations undertaken for the 52° echelle showed the focussing mirror off-axis angle to be 3.625°, for a collimator off-axis angle of 2.274°, in order to minimise residual coma, and 100mm radius of curvature slits required. These findings were substantiated by the very small residual coma in the image and the constancy of line profile with slit length found by experiment.

However, the larger blaze grating enables the off-axis angle of the collimator to be reduced to a value of 1.959° half angle. The calculations were performed for the full grating aperture presented to the collimating mirror which is 101mm wide by 128mm high. Results showed the optimum focussing mirror off-axis angle to be about 3.6°, very close to the value obtained for the 52° echelle. This was found to be the best value when the echelle was set up in the spectrometer.

When the grating width was reduced, as described later, to 120mm and hence the aperture to 58.7mm at the collimator, the calculations

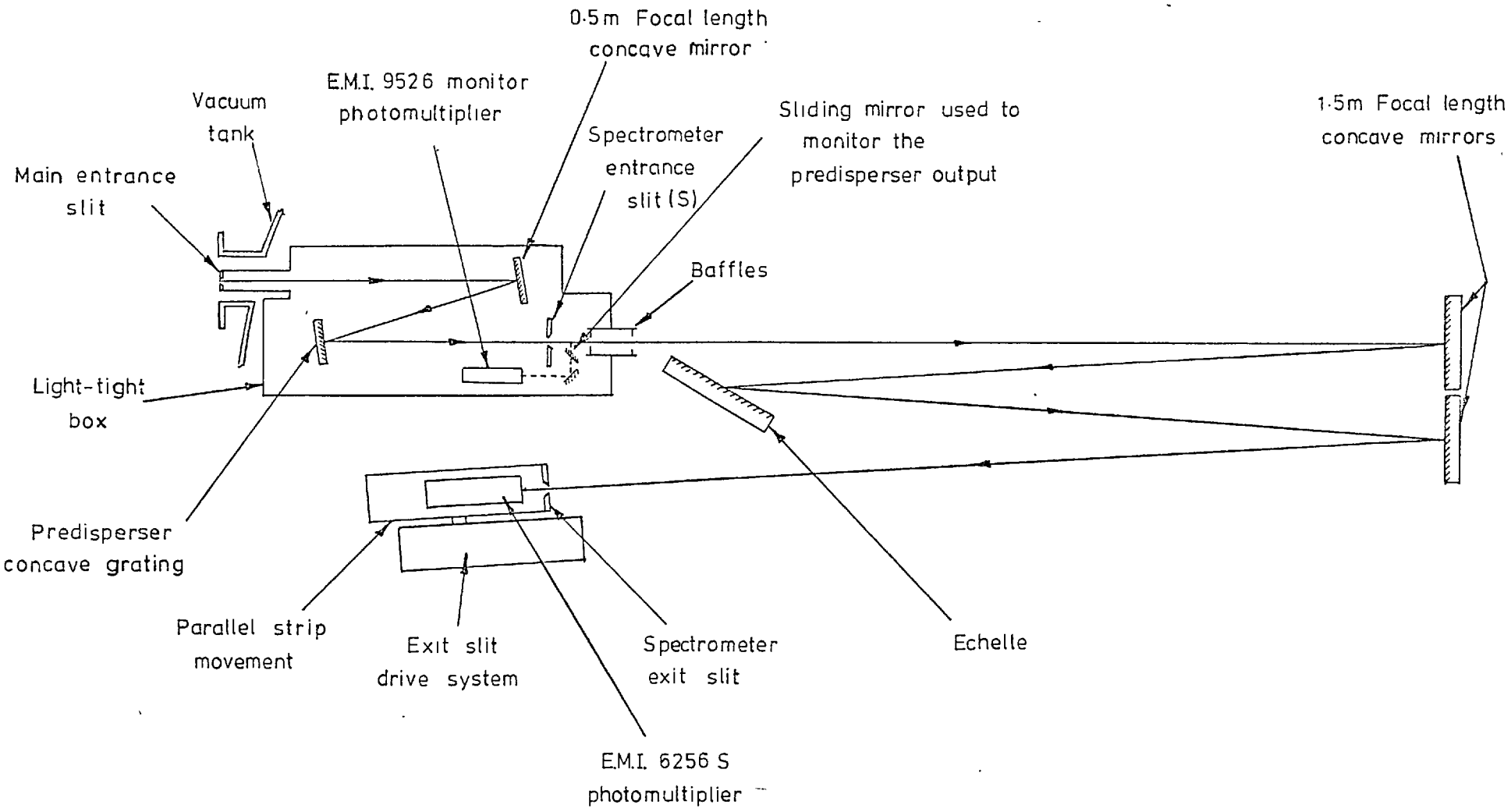

FIGURE 3. THE SPECTROMETER OPTICAL LAYOUT

indicated that a rather smaller value of off-axis angle for the focussing mirror was required, at about 3.3°. In practice, no significant change in line profile was observed when the angle was kept at 3.6°. The radius of curvature of 100mm for the curved slits was found to be still satisfactory as this is defined by the instrument focal length and the angle between the incident and diffracted beams.

The following parameters refer to the optical configuration used with the 63° blaze echelle with restricted aperture:-

Off-axis angle of collimating mirror	1.959°,
Angle between incident and diffracted beams	7.548°,
Distance between the centres of the mirrors	162.2mm,
Distance from mirrors to grating	1215mm,
Off-axis angle of focussing mirror	3.6°,
Radius of curvature of slits	100mm.

1.4 Predisperser

The off-axis Wadsworth mount, used for the predisperser, consists of a concave mirror (1m radius of curvature) producing parallel radiation incident on the concave grating (0.75m radius of curvature). The latter produces an image of the entrance slit at a point distant, r', from the grating surface in the direction of the diffracted ray. Let α and α' be the angles of diffraction and incidence respectively measured from the grating normal and R be the radius of curvature of the grating. We have the following relation (Stroke (1967)) for the Wadsworth mount focus condition giving the position of the focal plane r' as:-

$$r' = \frac{R \cos^2 \alpha}{\cos \alpha + \cos \alpha'} \qquad (8)$$

Let us define axes x and y, as shown in figure 4, such that x is the direction of the diffracted beam and y is normal to this, with the co-ordinate system centred on the grating centre when $\alpha = 0$. Also let a tie bar, of length ℓ, be attached to the grating along the normal to its surface with P its extremity. The angle between the x-axis and the normal is therefore α. Now the focal plane must always be coplanar with the predisperser exit slit S (which is the spectrometer entrance slit). The x co-ordinate of S (r'_s) is given in terms of the angle between the diffracted and incident beams, α_o, by using equation (8) as:-

$$r'_s = R \frac{1}{1 + \cos\alpha_o} .$$

When the grating is rotated to choose a different wavelength at the slit S the grating must be translated in the x direction such that its centre is a distance:-

$$r'_s - R.\left[\frac{\cos^2\alpha}{\cos\alpha + \cos\alpha'}\right]$$

from the centre of the co-ordinate system, in order to maintain focus. The co-ordinates of the point P are (x_p, y_p) where:-

$$x_p = \ell\cos\alpha + R\left[\frac{1}{1 + \cos\alpha_o} - \frac{\cos^2\alpha}{\cos\alpha + \cos\alpha'}\right] \quad (9)$$

$$y_p = \ell\sin\alpha. \quad (10)$$

The grating used is a Bausch and Lomb replica with 600 grooves/mm blazed at $2^o4'$. Geometry of the predisperser is such that $\alpha - \alpha' = \alpha_o = 18^o10'$. In order to evaluate the locus of the point P, such that the first order spectra of a chosen wavelength is in focus at the slit S, a relationship between α, α' and λ is first found. This is simply

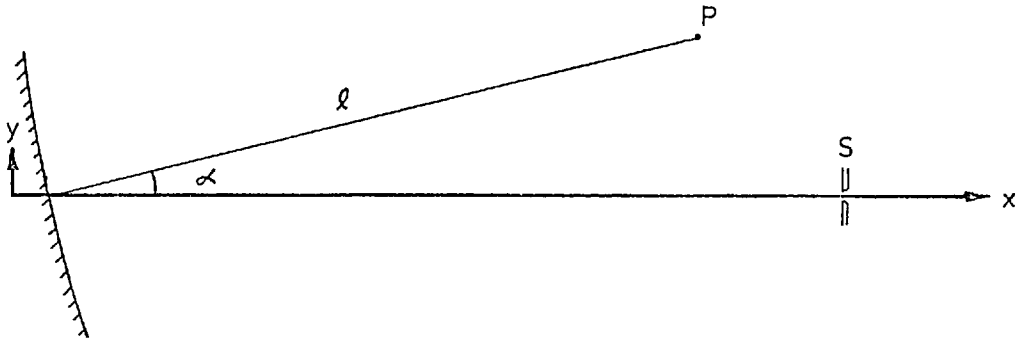

FIGURE 4. PREDISPERSER GRATING

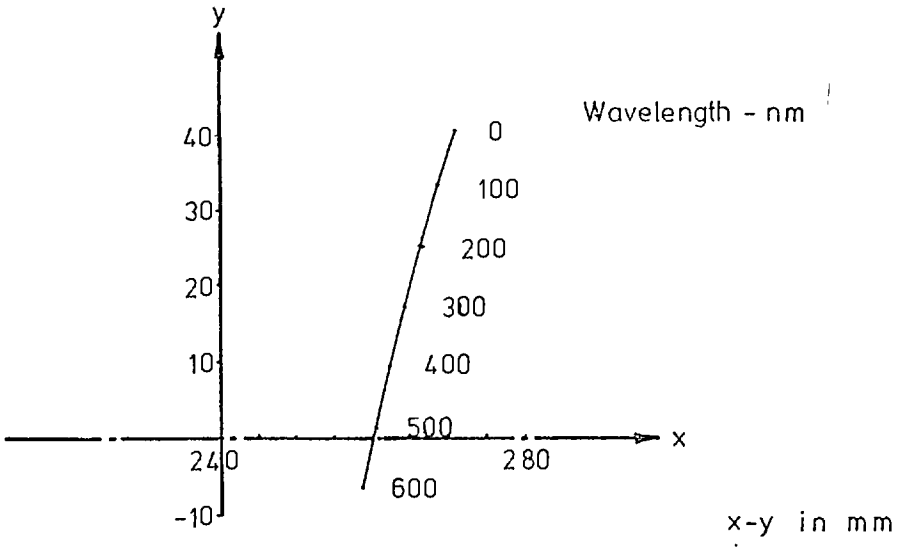

FIGURE 5. LOCUS OF THE PREDISPERSER GRATING NORMAL POINT, P, WITH $\ell = 260$ mm

derived from the grating equation (2), putting $\alpha = \psi - \phi$ and $\alpha' = \psi - \phi'$, as:-

$$\frac{\alpha + \alpha'}{2} = \sin^{-1}\left[\frac{\lambda}{3{\cdot}3.10^{4}.\cos 9^{\circ}5'}\right].$$

Table 2 gives the values of α and α' corresponding to wavelength intervals of λ100nm. The co-ordinates of the point P (x_p, y_p) are also given in the table using equations (9) and (10) with ℓ = 260mm. A full scale plot of the locus of P is given in figure (5). Although it appears that this locus is not a straight line, such an approximation is possible over a band of $\pm$ λ100nm, with very little degradation in focus outside this region. In practice the locus of P used was a straight line tangential at λ150nm.

Inverse dispersion at the slit S is given by differentiation of equation (2) with respect to $\alpha = \psi - \phi$ as:-

$$\frac{d\lambda}{d\alpha} = \frac{d\cos\alpha}{m},$$

where m, the order, = -1 and d = $\frac{1}{600}$mm. The inverse linear dispersion is given, using equation (8), by:-

$$\frac{d\lambda}{dy} = -\frac{\cos\alpha + \cos\alpha'}{4{\cdot}5.10^{5}.\cos\alpha}.$$

Using the values of α and α', given in table (2), shows that the change in inverse linear dispersion at the slit S between zero order and λ600nm is approximately 3%. At λ200nm the inverse dispersion is 4.31nm/mm. The locus of P (figure (5)) shows that P moves 49.0mm for λ600nm change in wavelength; which gives an effective inverse dispersion at P of 12.2nm/mm. With 1 digit on the external readout (see section 2.1) representing 0.025mm movement at P, then the counter readout corresponds to 0.305nm/digit. An experimental value of

λ nm	α'	α	x_p mm	y_p mm
0	- 9° 5'	9° 5'	271.1	41.0
100	-10°49'	7°21'	268.7	33.3
200	-12°34'	5°36'	266.6	25.4
300	-14°19'	3°51'	264.4	17.5
400	-16° 4'	2° 6'	262.4	9.5
500	-17°49'	21'	260.5	1.6
600	-19°35'	-1°25'	258.8	- 6.4

TABLE 2. The angles of incidence (α') and diffraction (α) are given for the off-axis Wadsworth mounted concave grating of the predisperser. The corresponding co-ordinates of the point 260mm along the grating normal are also given.

0.301nm/digit was actually found at λ200nm. The major source of this discrepancy arises from the fact that the angle α_o between incident and diffracted beams varies as the grating is rotated (and translated), in order to maintain symmetrical illumination of the echelle, and its true value is probably different from $18^{\circ}10'$.

The predisperser exit slit (main spectrometer entrance slit S) is curved, of radius of curvature 100mm (see section 1.3), with its centre of curvature in the negative y direction in figure 4. As a result of this, it is necessary to use a curved entrance slit for the predisperser. Owing to the demagnification of the predisperser mirror (1m radius of curvature) and the grating (0.75m radius of curvature), the curvature of the entrance slit must be approximately 133mm, in order to obtain good imaging onto the echelle entrance slit. The width of this slit is usually set at 0.1mm and thus there is considerable overlap of the image in the slit plane S, allowing for slight changes of the image curvature as a result of the dispersion at the predisperser grating.

The bandwidth of radiation transmitted through a 10μm slit S, with an inverse dispersion of 4.31nm/mm, would be approximately 0.04nm assuming an infinitely narrow predisperser entrance slit. However, for the 0.1mm slit used, the bandwidth will be approximately 0.32nm, which is still more than adequate to prevent overlapping of orders in the spectrometer.

CHAPTER 2

THE SPECTROMETER DESIGN - MECHANICAL AND GENERAL

The mechanical design of the spectrometer is described in this chapter. Spectral image scanning and the signal detection methods are described in detail. The last two sections deal with the photon-counting system and efficiency of the overall spectrometer.

2.1 Predisperser

In order to prevent overlapping orders in the focal plane of the spectrometer as a result of the small free spectral range, as seen in table 2, it is necessary to limit the bandwidth of the radiation into the spectrometer. In the present instrument this is accomplished by the use of a concave mirror and concave grating in an off-axis Wadsworth mounting. This particular form of mounting has the advantage of being stigmatic. Figure 3 shows the layout of the predisperser.

The optical system described in detail in section 1.4 requires that the 1m radius of curvature concave mirror produces a parallel beam incident on the 0.75m radius of curvature concave grating. Selection of the desired wavelength at the main spectrometer slit S is accomplished by rotation of the grating, which is also translated in the line joining the grating centre and slit S in order to maintain the focal plane coincident with S. Symmetrical illumination of the echelle is maintained during these movements by rotation of the predisperser mirror. This movement is achieved using a mechanical linkage and an angle halving arrangement between the grating and mirror. Rotation and translation of the grating is accomplished by the movement of a point 260mm along a tie bar, parallel to the grating normal, by a merton nut leadscrew and carriage.

The precision ground leadscrew of 0.5mm pitch is driven by gears

with a reduction of 2:1, and outside the vacuum tank the drive is linked to a counter which clocks up 1 digit for 0.1 turn. Thus we have:-

$$1 \text{ digit readout} \equiv \frac{1}{40} \text{ mm displacement of P.}$$

This represents an inverse dispersion of 0.3nm/digit at the exit plane and, as seen from section 1.4, is virtually independent of wavelength. Movement of the point, P, on the grating normal by 50mm gives a continuous wavelength selection at S from 0 to λ650nm with a bandpass of about 0.4nm using a narrow slit, S, and 0.1mm wide entrance slit.

A small plane mirror is used to direct the exit beam via another plane mirror onto a small 9526S E.M.I. photomultiplier with its window coated with the phosphor sodium salicylate. The mirror is run on a small linear ball race which allows it to be moved, into the exit beam, from outside the vacuum tank. On the grating side of the exit slit, a facility is provided to bring a small beam-splitter into the beam to observe the auto-collimated beam from the main optics.

The whole of the predisperser is enclosed in a light-tight box with anti-transmitting apertures in its side to allow gas (from a differentially pumped lamp) to be pumped away. Optical baffles are used between the entrance slit and concave mirror, between the grating and exit slit and after the exit slit. A single baseplate supports the predisperser and this is mounted on three vertical adjusting screws for levelling and alignment purposes.

2.2 Echelle mount

The echelle is mounted in a cell which rests on radial VEE's in a turntable. The turntable is supported by a large thrust race and is turned using a precision lapped leadscrew and merton nut, which drives a flat stainless steel band wrapped around the perifery of the turntable. The pitch of the leadscrew is 0.5mm and is driven from outside

the vacuum tank by a 1000:1 reduction gearbox and servo-motor with digital readout of angular position.

Apart from the tilt of the grating and levelling screws the whole grating and turntable can be translated at right angles to the tank axis in order to alter the off-axis angle of the collimating mirror.

2.3 Mirrors

Main mirrors of the spectrometer are 3m radius of curvature with the following specification:-

Collimating mirror	165mm wide, 165mm high, 30mm thick;
Focussing mirror	150mm wide, 165mm high, 30mm thick.

Both mirrors are made of Cer-vit low expansion glass. The surfaces were polished to 1/20 wave in the visible to within 10mm of the edge. Surface finish is better than 2nm. They were both coated with Al + MgF_2 for optimum reflectivity at λ120nm. The mirrors were made and coated under a contract with Acton Research Corporation in the U.S.A.

The mounts for the mirrors allowed the following degrees of freedom:-

1. Focus control by translation of the whole mirror and mount parallel to the tank axis. This is controlled from outside the tank, with digital readout where 1 digit represents 5μm mirror travel.

2. Rotation about a horizontal axis perpendicular to the tank axis i.e. to tilt the beam in a vertical direction.

3. Rotation about a vertical axis through the centre of the mirror face.

4. Lateral translation, perpendicular to the tank axis, of the focussing mirror to alter the mirror spacing.

2.4 Slits

Both the main spectrometer slits are Hilger and Watts type F1386 symmetrically opening. These are specially cleaned of manufacturing oils and fitted with 100mm radius of curvature jaws made of 'PITHO', a special small grain size steel. The jaws are symmetrically opening and can be set using a micrometer type adjustment. The slit mount allows rotation of the slit about an axis normal to the slit plane through its centre.

2.5 Exit slit system

Scanning of the image of the spectral line in the focal plane of the spectrometer is accomplished by movement of the exit slit and photomultiplier parallel to the focal plane in steps of 0.5μm.

It was thought necessary to move the photomultiplier with the exit slit so that transmitted light through the slit would fall on the same area of phosphor. This prevents any non-uniform detector response, Freeman and Talim (1970), across its surface from producing non-linearities in the output intensity of the profile.

An E.M.I. 6256S venetian blind 13 stage photomultiplier, with fused silica window coated with the phosphor sodium salicylate, is mounted behind the slit. A mu-metal shield is used around the tube and its dynode chain, attached to the base, is potted in a suitable compound to facilitate heat dissipation. The latter was not found to be significant unless the E.H.T. was left on for more than about 4 hours, after which time the dark current would be rising significantly. Both the exit slit and photomultiplier are suspended by a parallel strip movement consisting of four thick phosphor bronze strips 50mm wide by 92.7mm long which were rigidly clamped at both ends.

The assembly of slit and photomultiplier are pushed in discrete steps to scan the image. The drive for this movement is obtained from

an anvil, bearing on the side of a wedge, which is pushed by a micrometer screw driven through reduction gears by a small stepping motor. The whole of the drive is enclosed in an air-tight box enabling ordinary lubrication to be used. The linear drive is transmitted through this box using a double bellows arrangement, to prevent forces being exerted on the wedge when the spectrometer is evacuated. The stepping motor performs 20 steps per revolution, the reduction gears are ratio 5:1 and the micrometer pitch is 0.5mm with a wedge ratio of 10:1. Thus 1 step of the motor represents 0.5μm slit movement. Limit relays on the micrometer and a rotational relay on the stepping motor are used for control of the drive (see section 2.9). A total movement of 2.5mm is available.

The whole of the exit slit system (slit, photomultiplier, parallel strip movement and drive unit) is mounted on a carriage for focussing, which is driven by a precision ground leadscrew and nut of 0.5mm pitch. This control is brought outside the vacuum tank using reduction gears and couplings to give a direct readout of position with 1 digit representing 5μm focus control with a total movement of 80mm. Lateral translation of the whole system is provided which allows the off-axis angle of the focussing mirror to be changed. Also, rotation of the whole exit slit system and translation carriages allow the photomultiplier-slit axis to pass through the centre of the focussing mirror after changing the lateral translation.

The parallel strip movement was tested for overall parallelism using a Michelson laser interferometer and fringe counting techniques and it was found that parallelism is of the order of 1 part in 2000 (distance moved by two ends of the strip movement differed by about 1 part in 2000 for the 2.5mm scanning distance involved) which is more than adequate for the accuracy required. The average value of the step size was evaluated and found to be 0.4985 $\pm$ 0.0005μm over the whole of

the 2.5mm travel. Facilities are available for continual monitoring of the exit slit position in the focal plane by the use of a Michelson laser interferometer but this has not been found necessary.

2.6 Mountings and the vacuum tank

All of the optical components are mounted on a large optical bench which lies with its top surface 179.5mm below the optical axis and 100mm below the tank centre-line axis. The bench is made of magnesium which was used because it has a high internal damping coefficient and it was hoped this would prevent any vibrational resonances. A flat optical bench supported near its ends would be susceptible to such effects. No evidence of resonances has ever been observed in practice.

The optical bench is kinematically supported on balls which rest on three substantial pillars which pass through the vacuum tank wall, via bellows seals, onto a large concrete block. This block also carries the vacuum tank and is mounted on four large springs and oil dampers to provide vibration isolation. The resonant frequency of this system in the vertical plane is about 1.7 hertz.

Considerable care was taken during the design in order to minimise differential thermal expansion in the component mounts by the use of similar metals at critical points. In general, stainless steel was used as the main manufacturing material; suitably stabilised by heat-treatment where necessary. Where mechanical rotary lead-throughs are used, flexible couplings prevent tank evacuation forces from causing changes in optical alignment.

Both the end caps of the vacuum tank can be removed to give access to the various optical components. Also, there are a number of smaller access ports to enable various parts of the spectrometer to be reached without removing the end caps. The inside of the vacuum tank

has been coated with a low vapour pressure black epoxy paint to reduce scattered light.

2.7 Pumping system

The vacuum tank, of approximate volume $0.8m^3$, is pumped by an Edwards 1500l/sec. oil diffusion pump and liquid nitrogen cold trap which is backed by a 450l/min. rotary pump and molecular sieve foreline trap. A reservoir volume of about $0.06m^3$ in the backing line allows the system to be pumped for short periods without the use of the backing pump, and also allows the diffusion pump to be left on overnight (not pumping the tank) when the backing pump is isolated, but still running. These latter points allow temperature stability of the outside of the tank to be maintained whilst not putting the optics at risk of gradual or accidental degradation from pump oils. The butterfly valve between the diffusion pump and the tank is pneumatically operated and is automatically closed in the event of chilled water, mains power or compressed air supply failures or if a leak develops in a part of the vacuum system.

Typical ultimate pressure for the spectrometer is about 2.10^{-6} torr but this depends on the type of light source being used. The upper limit for the working pressure is about 5.10^{-4} torr and is governed by the photomultiplier E.H.T.

2.8 Temperature control and measurement

As already mentioned, the temperature of the spectrometer is maintained stable at $23.5^{\circ}C$ by controlling the surrounding air temperature.

A polythene tent is used to surround the vacuum tank but excluding all sources of heat such as the diffusion and backing pumps. The room temperature outside the tent is maintained between 20 and $22^{\circ}C$.

The temperature of the vacuum tank is sampled at six points by thermistors which were amply insulated from the surrounding air such that they detected the tank and not the air temperature. These thermistors form opposite elements in a bridge circuit whose out of balance voltage is used to change the ON-OFF time ratio of a triac control circuit driving heaters. Heaters of the form of banks of 30W resistors are placed beneath the concrete block and the air around the vacuum tank within the tent is thoroughly stirred using fans. The triggering circuit for the triac is synchronised to mains frequency and switches power only at zero voltage which with basically resistive load means that no radiative or mains borne radio frequency interference is produced.

Another thermistor is placed in the vacuum tank behind the grating and is used to monitor its temperature. Typically, if the laboratory temperature varies by $1^{o}C$ during a working day, the grating temperature varies by about $0.03^{o}C$. This is more than adequate for most shift measurements so far undertaken.

2.9 Image scanning and signal detection

As already mentioned, the spectral line profile is scanned by moving the exit slit and photomultiplier across the focal plane in steps of 0.5μm. Two methods of recording the output are employed.

Figure 6 shows a block diagram of the electronics. Photon counting is used for photomultiplier signal handling. The anode output pulses are amplified with a x16 gain amplifier and then pass into an integral discriminator with its level set at 200mV. This corresponds to an E.H.T. of 1.6kV, further details are given in section 2.10. One output of the discriminator feeds a ratemeter which allows an analogue signal to be recorded on the y-axis of an x-y recorder. The main output feeds a 25 MHz scaler and timer-display unit. Initiation of the timer

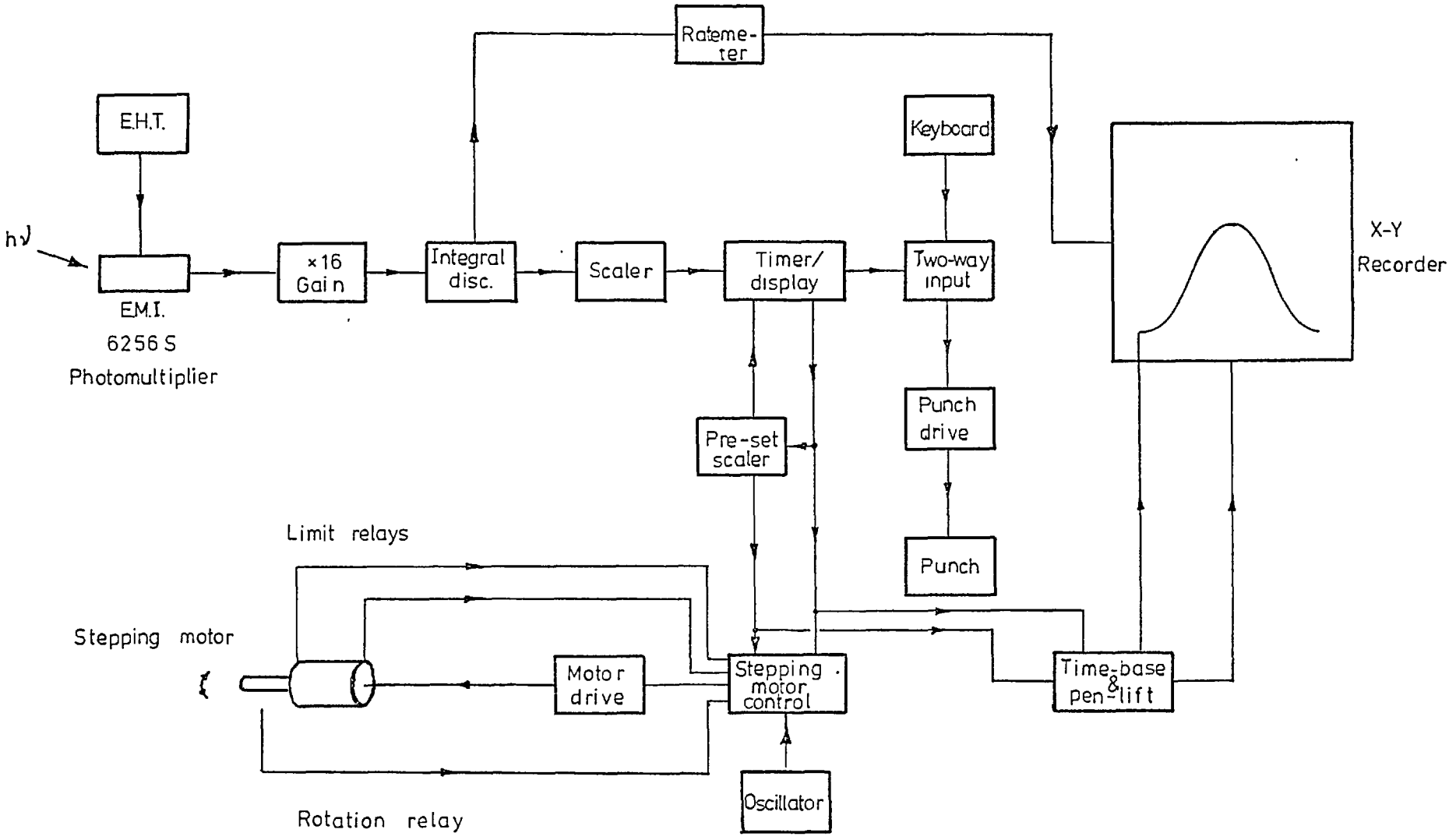

FIGURE 6. BLOCK DIAGRAM OF THE ELECTRONICS

unit, set at say 1 second integration, accumulates the pulses for 1 second and then supplies a pulse to the stepping motor drive unit which advances the exit slit by 0.5μm. During the time required to step (30msec) the accumulated data in the scaler is read by the timer display unit and the information presented to a paper tapepunch using BS interface. In parallel with the punch is an alpha-numeric keyboard for adding further information to data tapes. When the integration and punching cycle has finished another integration cycle is started. This process continues until the preset scaler, which receives a pulse at the beginning of the accumulation period, indicates the required preset number of steps in the scan have been made, at which time it prohibits further cycles.

When the accumulate is first started, a time base controlling the x-axis of the recorder is initiated and the pen lowered onto the paper. At the end of the preset number of steps the pen is lifted and the time base reset. As well as stopping the stepping motor, the system automatically reverses it and an internal oscillator produces pulses to allow the system to return to the start of the scan. End stop relays are used to indicate the extremities of the scan and can be used as reference starting points. Also a rotational relay on the stepping motor shaft allows a continual check on the scan. One closure of the relay represents 20 steps. Both the relay output and step number are presented on numerical indicators.

Typical scans of 160 steps producing about 40 data points on the upper 50% of the line profile with 1 second integration time per step are employed. Dark current count rate is usually 10-30 counts/sec. at an E.H.T. of 1.6kV. Profiles with a distribution peak of about 200 counts/sec. can be handled by repeat scans of the profile. If the shift due to say discharge current change is being examined, a symmetrical set of scans taken at the different currents is obtained until

sufficient accuracy has been achieved. This could represent up to a total of 19 scans or as few as 5.

2.10 Pulse counting

Figure 7 shows the dynode chain resistors and anode circuit for the exit slit photomultiplier. Because the photomultiplier is used inside the spectrometer vacuum tank all the electronic components shown in the figure are 'potted' in a suitable compound at the base of the tube in order to facilitate power dissipation (between 1.5 and 2 watts) and to reduce the possibility of arcing. The latter could also occur between pins at the tube base and hence the E.H.T. was never switched on unless the pressure in the spectrometer was below about 5.10^{-4} torr.

The anode pulses are transmitted through coaxial cable to the amplifier and pulse handling equipment as shown in figure 6. The photomultiplier is a 13 stage venetian blind E.M.I. type 6256S which has a low dark current and peak photocathode response at λ400nm corresponding to the fluorescent emission from sodium salicylate used as the ultraviolet sensor. The venetian blind dynode structure does not lend itself to particularly fast response but in this particular application where low light levels are encountered, this is not important. The observed anode pulse at the amplifier for a single photoelectron at 1.6kV is shown in figure 8. Although this has a total width of 40ns the correction for coincidences is negligible for count rates below 10^5 counts/sec.

The amplifier output passes into a fast discriminator which produces a standard output pulse for every input pulse if it satisfies preset input conditions set up on the unit. These are either:-

Integral mode where an output is obtained for every input pulse that exceeds a certain discriminator level;

or:-

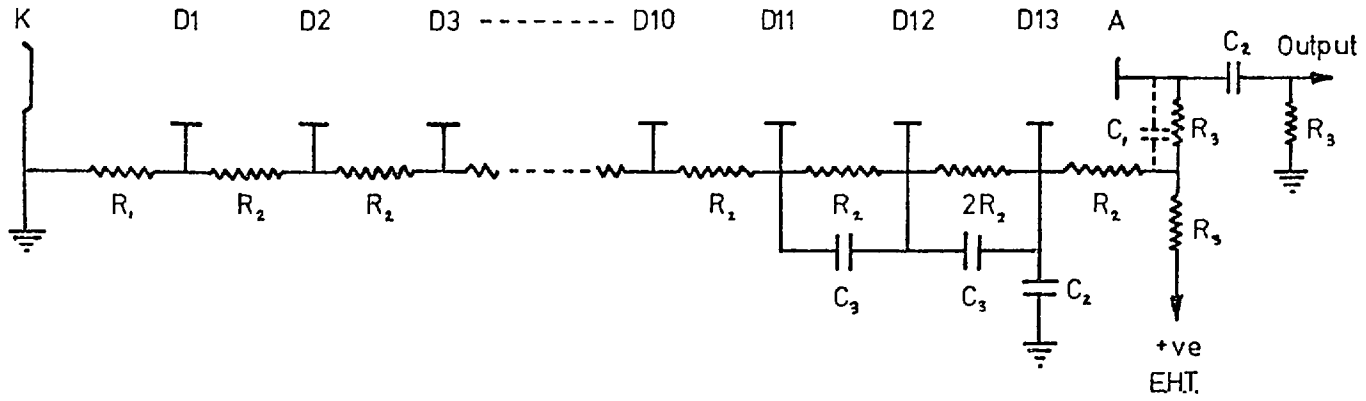

Components :-

R_1 = 150 kΩ		C_1 = 8 pF	
R_2 = 100 kΩ		C_2 = 0·005 μF	3 kV Wkg.
R_3 = 47 Ω		C_3 = 0·001 μF	600 V Wkg.

FIGURE 7. E.M.I. 6256 S PHOTOMULTIPLIER DYNODE CHAIN

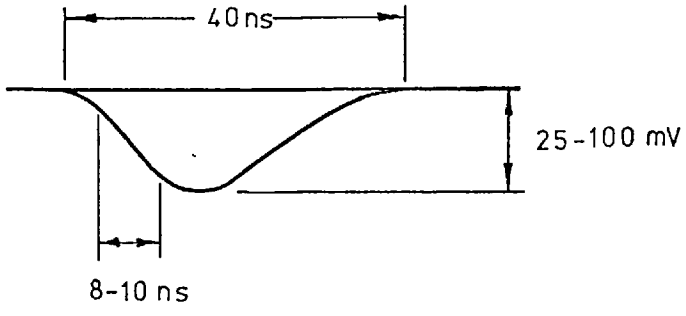

FIGURE 8. TYPICAL OUTPUT PULSE FROM A SINGLE PHOTOELECTRON

Differential mode which produces an output if the input is above a certain level but is below this level plus another level i.e. produces an output if the pulse height is within a preset window.

Thus if N(v) is the number of pulses with amplitude between v and v + dv then we have:-

Integral mode:-

$$\text{Output} = \int_{V}^{\infty} N(v)dv$$

where V is the level above which an output pulse is obtained.

Differential mode:-

$$\text{Output} = \int_{V}^{V+dV} N(v)dv$$

where V is the lower discrimination level and dV is the window width.

In order to make maximum use of photon counting it is necessary to evaluate the optimum discriminator settings. A series of experiments were performed in order to decide:-

a. the lower level of the integral mode operation in order to obtain the best value for signal to noise ratio;

b. the best E.H.T.;

c. whether or not Poisson statistics are obeyed for the observed dark current, this enables measurements to be made at low light levels which will not contain systematic errors due to peculiar changes in dark

current.

The photomultiplier was set up so that it could be illuminated with λ435.8nm radiation. Used in the integral mode, the observed count rate with a constant illumination and then with no illumination (background) were evaluated for different discriminator levels. This was done at 1.6 and 1.9kV E.H.T. and the results shown in figure 9 for the integral pulse height distributions.

Using the differential mode, we can examine the integral distributions in more detail. What we are looking for is evidence of a single photoelectron effect in the pulse height distributions. The latter would manifest itself in a 'bump' in the distributions situated at the single photoelectron pulse height value. Figures 10a, b and c show differential pulse height distributions for a 2.5mV window corresponding to 1.6, 1.9 and 2.0kV E.H.T. respectively. Figure 10d shows a repeat of 1.9kV E.H.T. distribution for a larger intensity of illumination. There is evidence in the 1.9 and 2.0kV curves for a bump in the distribution.

The position of this 'bump' is calculable using the relation giving the amplitude of the anode current pulse i_a as (see E.M.I. photomultiplier catalogue):-

$$i_a = \frac{G\,p\,e}{\tau\sqrt{2\pi}} \exp\left[-\frac{1}{2}\left(\frac{t}{\tau}\right)^2\right] \qquad (11)$$

where G is the photomultiplier gain,

p is the number of photoelectrons generated in time t,

τ is related to the width at half maximum amplitude of the anode pulse by:-

$$\tau = \frac{\text{Half max. amp. width}}{2.36},$$

e is the electronic charge.

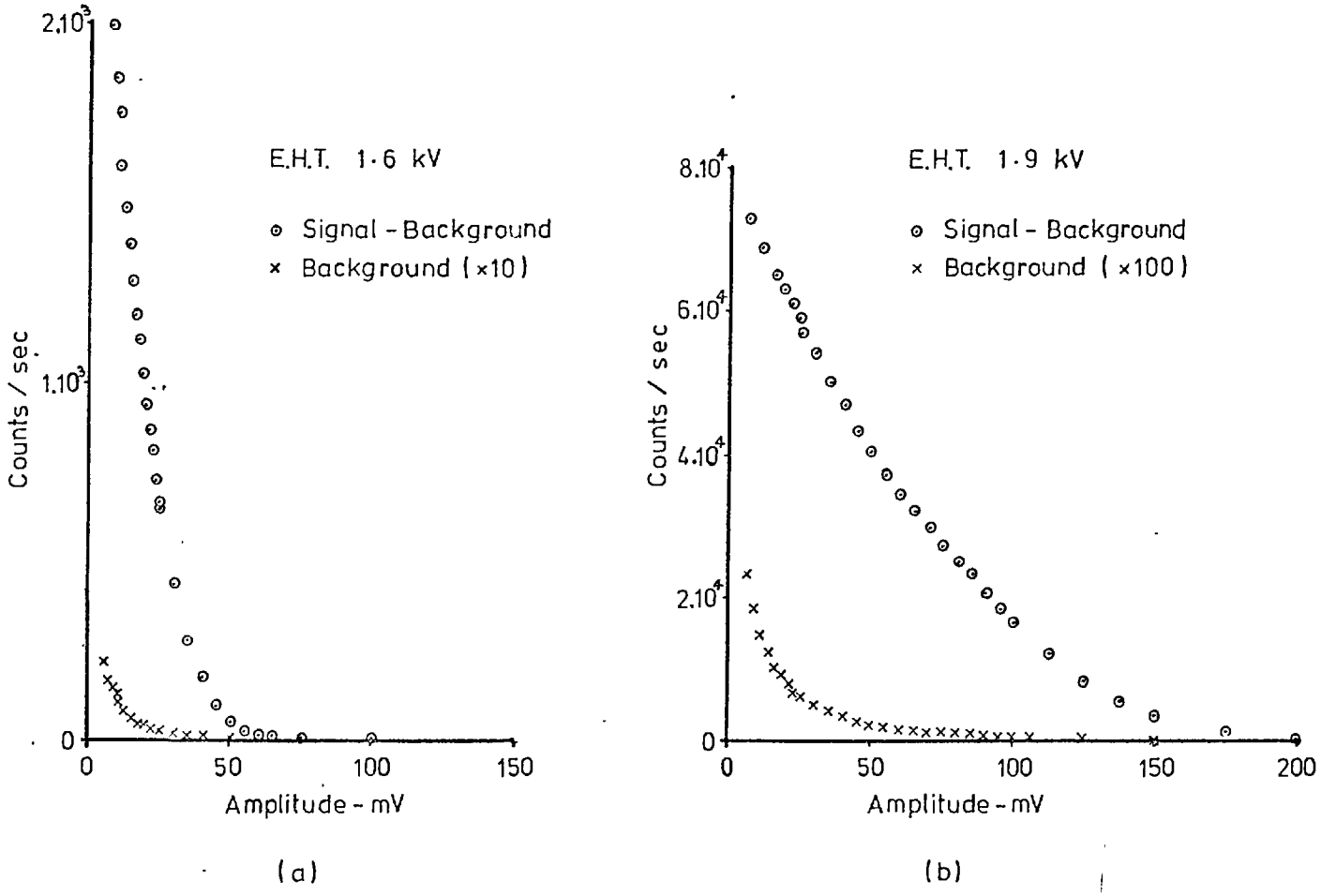

FIGURE 9. INTEGRAL PULSE HEIGHT DISTRIBUTIONS FOR E.M.I. 6256 S PHOTOMULTIPLIER

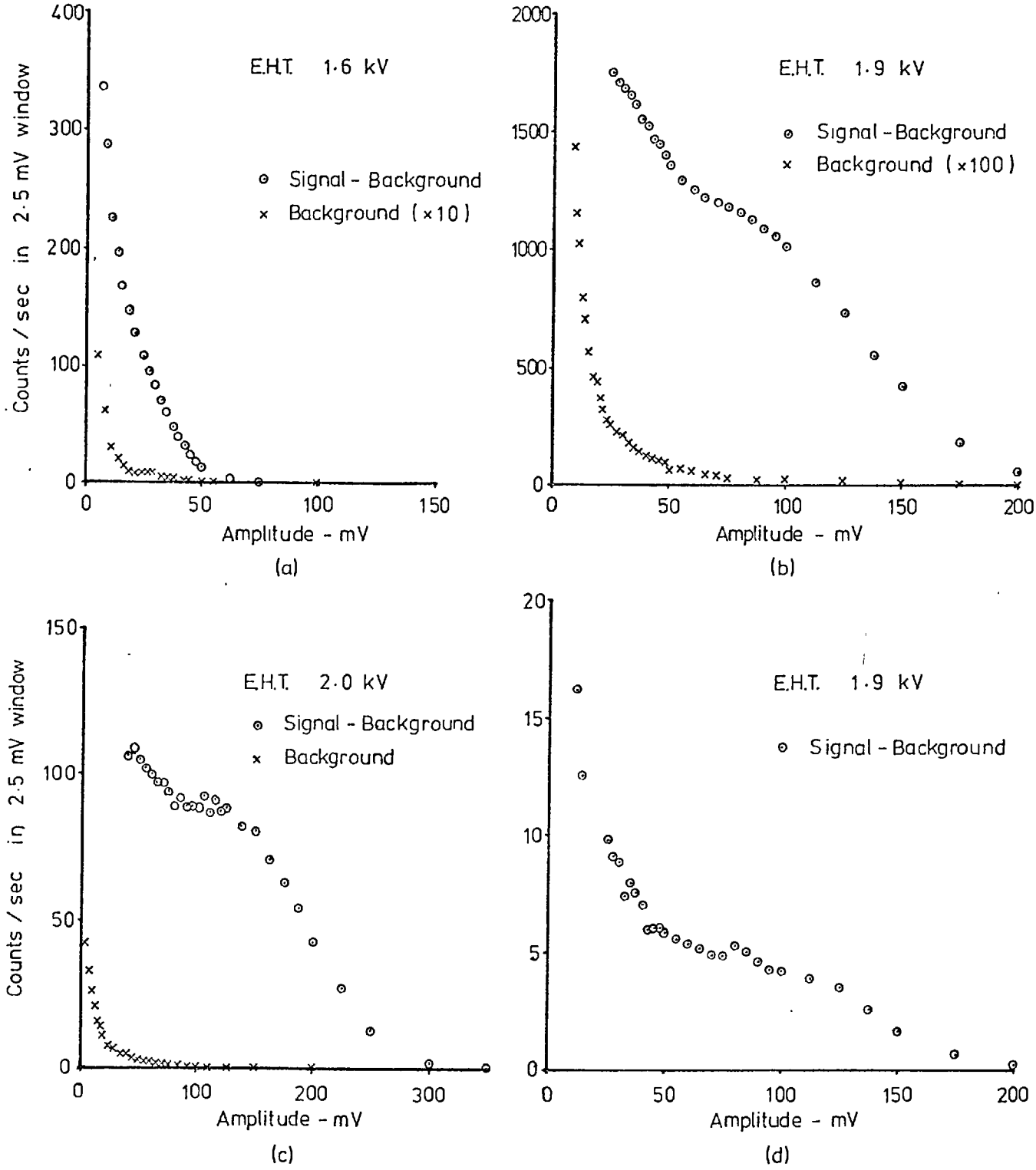

FIGURE 10. DIFFERENTIAL PULSE HEIGHT DISTRIBUTIONS FOR E.M.I. 6256 S PHOTOMULTIPLIER

Provided C_1, R_3 in figure 7 are such that $C_1R_3 \gg \tau$, then the output pulse will be realised. Now for the particular photomultiplier used, the internal capacitance shunting the anode is 8pF. Hence $C_1R_3 \simeq 40$ns. Using the manufacturers value for the half maximum amplitude width of 15ns, the above requirement is satisfied. The gain, G, is obtained from the manufacturers cathode sensitivity of 66μA/Lumen and the overall sensitivity of 2000A/Lumen at 1.55kV E.H.T. as:-

$$G = 3.03.10^7 \text{ for } 1.55\text{kV E.H.T.}$$

Putting p = 1 and t = 0 we obtain the anode current pulse i_a for a single photoelectron, from equation (11), as:-

$$i_a \simeq 0.3\text{mA}.$$

Using a value of C_1 = 8pF, defined by the photomultiplier, the output pulse will be 15mV. Using the manufacturers values of the variation of gain with E.H.T., we obtain values for the gain and anode pulse height versus E.H.T. given in table 3.

E.H.T. kV	Anode Pulse mV	Gain, x 10^7
1.55	15	3.0
1.60	19	3.8
1.80	57	11.4
1.90	95	19.0
2.00	126	25.0

TABLE 3. E.M.I. 6256S photomultiplier pulse height and gain, derived from the data supplied by E.M.I., as a function of E.H.T.

Comparing the values of the single photoelectron pulse heights given in table 3 with the differential pulse height distributions shown

in figure 10, we see that the observed 'bump' is not very far from the calculated positions. Hence, we may conclude that this is probably a result of single photoelectron events. Thus the lower discriminator level should be set somewhere on the lower side of the 'bumps'.

Figure 11 shows a plot of (Integral Signal - Background)/ Background as a function of the discriminator level. This shows a broad maximum indicating that the discriminator level should be set to eliminate the large number of low amplitude pulses. A level of 50mV appears reasonable for the 1.9kV E.H.T. and can be scaled to other E.H.T. values using table 3.

An investigation into the optimum E.H.T. was accomplished by changing the discriminator level such that when the photomultiplier is illuminated with light the same count rate is observed for different E.H.T. values. Table 4 gives the results obtained and also enables an estimate of the relative change in gain between E.H.T. values. This is normalised to the value of $3.8.10^7$ for the gain at 1.6kV from table 3.

E.H.T. kV	Discriminator Level mV	Background Count Rate C/Sec.	Gain $\times 10^7$
1.6	11	25.0	3.8
1.7	19	25.1	6.5
1.8	31	25.1	10.7
1.9	50	23.2	17.3
2.0	75	26.6	25.8

TABLE 4. Observed background count rate corresponding to an integral discriminator setting which produces the same signal count rate for the different E.H.T's for the E.M.I. 6256S photomultiplier. The last column gives the gain derived from the discriminator settings based on the value of $3.8.10^7$ at 1.6kV given by E.M.I.

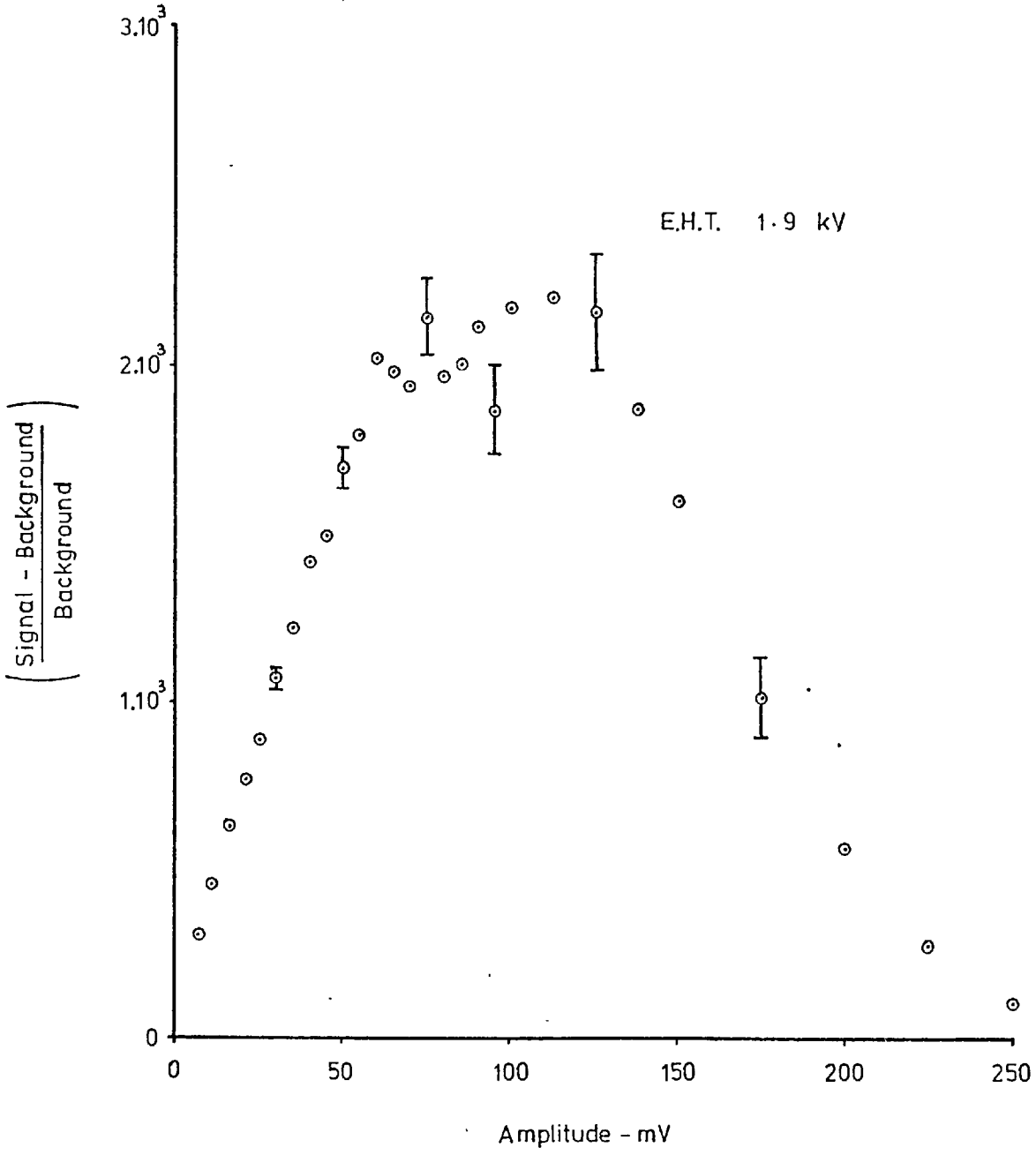

FIGURE 11. PLOT, USING INTEGRAL MODE, OF THE RATIO OF SIGNAL-BACKGROUND TO BACKGROUND VERSUS PULSE HEIGHT

The background count rates shown in table 4 do not differ significantly and hence there is little to choose between the E.H.T. values. The advantage in using 1.6kV is the smaller thermal heating of the dynode chain in the vacuum system. A lower heat dissipation maintains the dark current constant for a longer time and also reduces any thermal drift in the spectral line position.

Observations of the integral background count rate using 1.9kV E.H.T. and 50mV discriminator setting were made in order to determine whether there is any significant departure from Poisson statistics. Observing the count at intervals of 10 seconds for a total of about 30 minutes showed that the standard deviation of the mean was within 20% of the square root of the mean and there were no observed systematic changes in background count rate. Hence one may conclude that measurements made at very low count rates should not be susceptible to sudden changes in count rate.

2.11 Efficiency

An overall efficiency of the spectrometer can be estimated for the case where the source is not imaged onto the predisperser entrance slit. It is easily seen that, provided the source fills the optical system aperture, there is no luminosity gain in using a lens or mirror for imaging the source onto the entrance slit. There is in fact a loss in overall efficiency as a result of the extra optical element. The major disadvantage lies in the fact that the intensity distribution across the aperture follows that across the source, hence leading to the possibility of change in illumination producing apparent wavelength shifts as discussed later.

Figure 12 shows the predisperser entrance slit of width w, and height h_1. The source is placed at a distance x away and the aperture of the predisperser optics is F_1 in the horizontal dispersion plane

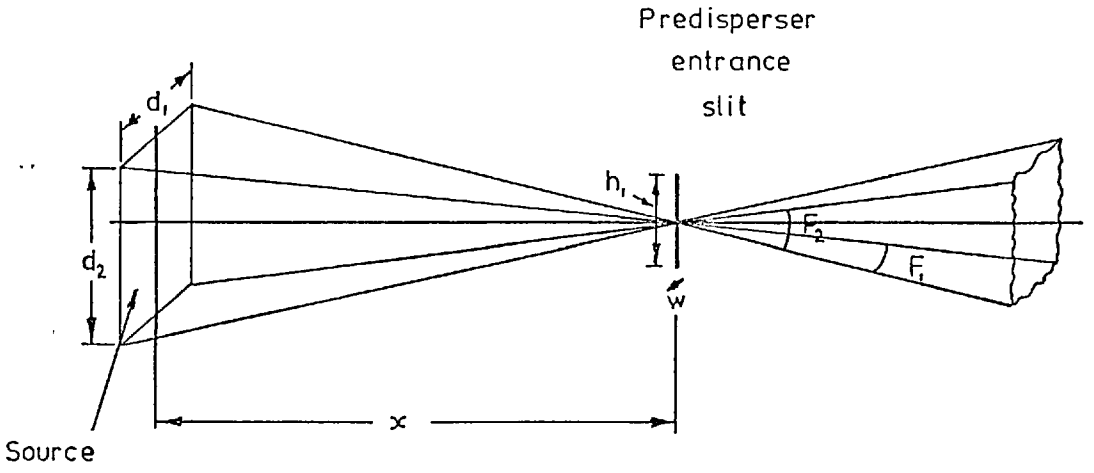

FIGURE 12. PREDISPERSER ENTRANCE SLIT ILLUMINATION PARAMETERS

(parallel to the slit width) and F_2 in the vertical plane.

If d_1 and d_2 are the widths of the source observed in the horizontal and vertical directions then $F_1 = \frac{d_1}{x}$ and $F_2 = \frac{d_2}{x}$. The area of the source used is $d_1\ d_2$, where we assume $h_1 \ll d_2$. The solid angle that the slit subtends at the source is $w_1\ h_1 \cdot \frac{1}{4\pi x^2}$ where $h_1 \ll x$. If $P(\lambda)$ is the radiant power/cm^3/4π steradians/unit bandwidth of the source, then the transmitted power through the predisperser entrance slit, for a source length of 1, is:-

$$P(\lambda)\ \frac{w_1\ h_1}{4\pi}\ F_1\ F_2\ 1,$$

where we assume $1 \ll x$.

Referring to the general optical layout shown in figure 3, it is now possible to follow the transmitted radiation through the optical system.

The power incident on the main spectrometer entrance slit is:-

$$P(\lambda)\ \frac{w_1\ h_1}{4\pi}\ F_1\ F_2\ R_1\ E_1\ 1$$

where R_1 and E_1 are the reflectivity and efficiency of the predisperser concave mirror and grating respectively.

The image of the predisperser entrance slit on the main slit will be of width Mw_1 and height Mh_1 where M is the predisperser magnification. If the main entrance slit has width w_2 and height greater than Mh_1 then the transmitted power will be:-

$$P(\lambda)\ \frac{w_1\ h_1}{4\pi}\ F_1\ F_2\ R_1\ E_1\ \frac{w_2}{Mw_1}\ 1.$$

Hence we have assumed no aberrations in the predisperser optics, i.e. no spread of the image; which is true if $w_1 \gg w_2$.

If the collimating mirror, focussing mirror and echelle reflectivities and efficiency are R_2, R_3 and E_2 respectively then the power transmitted through an exit slit of width w_3 would be:-

$$P(\lambda)\ \frac{w_2\ h_1}{4\pi}\ F_1\ F_2\ \frac{R_1\ E_1}{M}\ R_2\ R_3\ E_2\ \frac{w_3}{w_2}\ A\ l$$

where A is a factor defining the spread of the image in the focal plane. This involves the geometrical aberrations, slits, focussing errors, grating aberrations and the spectral emission characteristics of the source. An estimate neglecting source contributions can be made from the ray-tracing and the resolution tests.

The values of F_1 and F_2 are, in practice, defined by the size of the echelle used and the focal length of the main spectrometer.

Using a sodium salicylate phosphor of efficiency p%, photo-multiplier cathode efficiency q% and collection efficiency c% then the number of pulses per second at the anode is:-

$$N(\lambda)\ \frac{w_3\ h_1}{4\pi}\ \frac{F_1\ F_2}{M}\ R_1\ E_1\ R_2\ R_3\ E_2\ \frac{Alpcq}{10^6}\ \text{counts/sec.} \qquad (12)$$

where $N(\lambda)$ is the number of photons emitted by the source/cm^3/4π steradians/sec. in a bandwidth narrower than the spectrometer bandwidth (which is the case in the present instrument where narrow emission lines are observed).

Before evaluating the output count rate it should be noted that R_1, R_2, R_3, E_1 and E_2 are strong functions of wavelength whilst p is a weak function.

Let us assume the following values for the parameters:-

F_1, F_2 Apertures defined by the echelle, F_1 = 1/30, F_2 = 1/16;

h_1 Predisperser entrance slit height = 0.2cm;

w_3 Main spectrometer exit slit width = 8μm;

M Predisperser magnification = $\frac{27.5}{50}$ = 0.75;

l	Source length = 1cm;
R_1, R_2, R_3	Mirror reflectivities = 0.75 at λ160nm;
E_1	Predisperser grating efficiency, which near blaze at λ160nm is approximately 0.3;
E_2	Echelle efficiency = 0.3 at λ160nm. (Bausch and Lomb (1972));
A	Image spread function from ray-tracing $\simeq$0.3;
p	Phosphor efficiency = 50% (Samson (1967));
c	Collection efficiency = 40%;
q	Quantum efficiency of photocathode = 20%.

Substituting into equation (12) gives:-

Number of Anode pulses $\simeq N(\lambda).2.10^{-11}$ counts/sec.

The overall efficiency is very low, hence the observed signals are very small and measurements are restricted to the stronger emission lines.

C H A P T E R 3

ALIGNMENT, MEASUREMENT TECHNIQUES AND TESTING

A description of the optical alignment techniques used to set up the spectrometer are described. Determination of the shift and width of the observed profile is explained. Some line profiles of various spectral lines are given as well as a curve of the resolving power, defined by the half maximum intensity width of the observed profile, versus wavelength.

Illumination of the spectrometer optics is important when the instrument is to be used for monitoring wavelength shifts with source operating condition changes. Ideally, the relative illumination of the optics aperture should not change during measurements. However, this is not possible when the source is not imaged onto the entrance slit. Section 3.4 describes the results of extensive tests undertaken to investigate the possibility of systematic shifts occurring as a result of spectrometer illumination changes.

3.1 Optical alignment and adjustment

Initially, the various mirror and grating mounts, translation slides, slit adjustments, rotary lead-throughs etc. were set up and tested mechanically. A brief outline of the optical alignment will now be given.

The predisperser optical components were assembled in their mounts and their alignment set according to the theory given in section 1.4 and 2.1. A helium/neon laser beam was used to centre the components. The concave grating normal tie bar was adjusted to lie symmetrically between the incident and diffracted beams, when the zero order passed through the exit slit. The grating was then rotated to bring the first order beam to the exit slit and the image centred on

the slit by rotation of the grating about its normal. A telescope was used to set the exit slit vertical (using the ends of the slit arc as reference) by removing the main collimating mirror mount and illuminating the slit with a medium pressure mercury lamp. The grating and entrance slit of the predisperser were adjusted to give an approximate focus at the exit slit. Monitoring the exit slit illumination with the telescope, the rotation of the entrance slit was adjusted for alignment with the exit slit at the zero order and checked at λ546nm. Using the monitor photomultiplier, the predisperser output was observed after having solved problems of scattered light by the use of suitably placed black baffles. An attempt to repeat all the settings more accurately was thwarted by the image of the entrance slit appearing to have a bright narrow line down its centre. This was found to be a result of longitudinal reflections off the top and bottom of the entrance slit tube in the plane of the entrance slit. These reflections were completely removed by turning fine grooves of a suitable profile along the bore of the tube.

The echelle grating, concave mirrors and exit slit system were set up according to the results of the ray-tracing calculations which include mechanical limitations of the optical elements and their mounts. The direction of the exit slit and photomultiplier axis was such as to point towards the focussing mirror. Removing the predisperser grating and opening the main entrance slit (predisperser exit slit), the laser beam was passed into the system, set at 179.5mm above the optical bench, and the predisperser height adjusted to suit. With the collimator set at 1498mm from the entrance slit, the beam was directed to hit its centre. Rotational adjustment was then made on the mirror to send the beam back to hit the side of the entrance slit at the same height.

With the centre of the echelle set to the desired distance from

the entrance beam (according to the geometrical limitations), the beam was directed at the grating centre by rotation of the collimating mirror about a vertical axis. The grating rotation was changed such that a diffracted order returned to the collimating mirror and the tilt of the grating set such that the incident and diffracted beams were in the same plane. The height of other diffracted beams above the optical bench was checked and the grating rotation about its normal altered to bring them all to the same height. At the same time, the tilt of the grating was altered to bring the diffracted beams back to the correct height above the optical bench. It was not possible to observe the zero order, and hence make this setting simpler, but no problems were experienced in achieving the desired alignment of orders.

Now the echelle rulings were normal to the optical bench; a diffracted order was used to set the focussing mirror at the correct height and its centre 162.2mm from the collimating mirror centre. Tilt of the mirror and angular rotation were adjusted to send the reflected beam back to the exit slit at the correct height and with the correct off-axis angle (according to the ray-tracing). The exit slit height was now adjusted and set 1498mm from the focussing mirror.

Having initially set up the main optics, the echelle was replaced by a plain narrow mirror and the collimator focussed by autocollimation using the medium pressure mercury lamp to illuminate the entrance slit. Replacing the echelle and predisperser grating, diffracted orders were observed through the exit slit using the telescope after first removing the photomultiplier. The exit slit length was reduced to 1mm and the system approximately focussed. With the 10mm long slit, the slit rotation was adjusted to give uniform illumination along its length. An ^{198}Hg electrodeless lamp was now used to fully illuminate the optics and the λ546nm line observed through the system. Observing the echelle through the exit slit (wide) as the echelle was

slowly rotated, the intensity distribution change across the aperture was checked to see if the aperture was gradually illuminated uniformly.

Having set everything up and tested the optics by eye, the photomultiplier was assembled behind the exit slit. Final focus and slit alignments were made using hyperfine structure from a natural mercury filled cell used in the electrodeless lamp. The λ435.8nm line was found to be very suitable for this purpose.

During the course of this setting up procedure the predisperser grating and echelle rotations were noted corresponding to different orders and wavelengths. A calibration of the predisperser yielded an inverse dispersion of 0.30nm/digit between λ640 and λ289nm, where one digit represents one unit on the external control readout. The echelle rotation, p, corresponding to the observation of particular wavelengths and orders was noted and used to obtain a relation to calculate the order and rotational position for any other wavelength to be observed. Both calibration of the predisperser and echelle rotation were repeated when the spectrometer was evacuated.

A repeat calibration of the predisperser inverse dispersion showed the readout to represent:-

0.301nm/digit at λ100nm,

0.297nm/digit at λ400nm.

In order to find the order, m; digital readout position, p; for any wavelength, λnm, the following relation was found for the 63° blaze echelle:-

$$m = \text{nearest integer to } \frac{5648}{\lambda}$$

$$p = 25.592 + 4.0158\,(\theta - 58.33^\circ)$$

$$\text{where} \quad \theta = \sin^{-1}\left(\frac{n\lambda.10^{-3}}{6.3152}\right) - 3.774^\circ.$$

3.2 Determination of width and shift

As will be mentioned in section 3.3, it is not possible to obtain the true emission profile from the observations because of a lack of a known spectral emission profile, in the λ100 to λ200nm wavelength region, which can be used to evaluate the instrumental function. Hence, all measurements undertaken on the line profiles refer to the observed profile which is the convolution of instrument and source functions. However, from the point of view of secondary wavelength standards, this is not a severe limitation until interferometers and narrow band width lasers are readily available in the vacuum ultra-violet.

The total observed full width at half maximum intensity was taken directly from the x-y recorder traces of the profiles and needs no further elaboration.

The shift was determined from the line profile obtained from the digital output of the timer display unit. This information gave a reading of count-rate every 0.5μm (1 step) as the slit and photo-multiplier traversed the line profile. Typically 160 steps were made for one scan of the line. There could be up to 20 scans in a complete run to obtain a single shift measurement.

A programme was written, to run on the N.P.L. KDF9 computer, in ALGOL which allowed the centre of gravity of the observed line profile to be determined. A brief description of the programme will be given.

Information of run code, number of scans in the run, number of data points in a scan, wavelength and two control parameters are fed into the computer. The experimental count-rates are now read and assigned to a variable array, with the scan number and step number as parameters. Each scan is now treated separately and the peak of the profile found in order to locate the maximum intensity (as a count rate). Two modes of operation are now available. The programme can evaluate

the centre of gravity of the profile between two levels, as a percentage of the maximum, defined in the first data tape. Also, it can automatically evaluate the centre of gravity below a preset level, also defined in the first data tape, gradually encompassing more of the lower part of the profile. Intervals of 5% of the maximum are used. It also evaluates the centre of gravity in slices of 10% from the peak to zero intensity.

3.3 Instrumental resolving power

Profiles of various emission lines were observed for the 52° and 63° blaze echelles. Figures 13-19 show the scans of lines from different sources. The microwave source used to excite the NI line at λ120nm shows the problem experienced with Rowland ghosts using the 52° blaze echelle. At these short wavelengths these result from the ghost separation from the parent line being proportional to wavelength and the ghost intensity proportional to the inverse square of the wavelength. When this sort of error is present the shape of the line profile can be significantly changed by the form of the error as shown by Preston (1970a). This is a particularly bad grating and for this reason the 63° echelle was used for all the subsequent investigations, and did not exhibit any observable Rowland or other forms of ghosts.

Scans of the ^{198}Hg profile at λ184.9nm using the 63° echelle revealed that this line was self-reversed and that on decreasing the mercury number density by cooling the end of the cell in dry-ice enabled the width to be decreased. The λ209.5nm line of GeI excited in the hollow cathode lamp described in section 5.1 also showed considerable absorption. GeII lines showed less broadening, but as will be shown later, the width of these lines is always a function of discharge conditions. No emission line observed with the spectrometer was found to have a profile which was narrow enough and sufficiently

FIGURE 13.

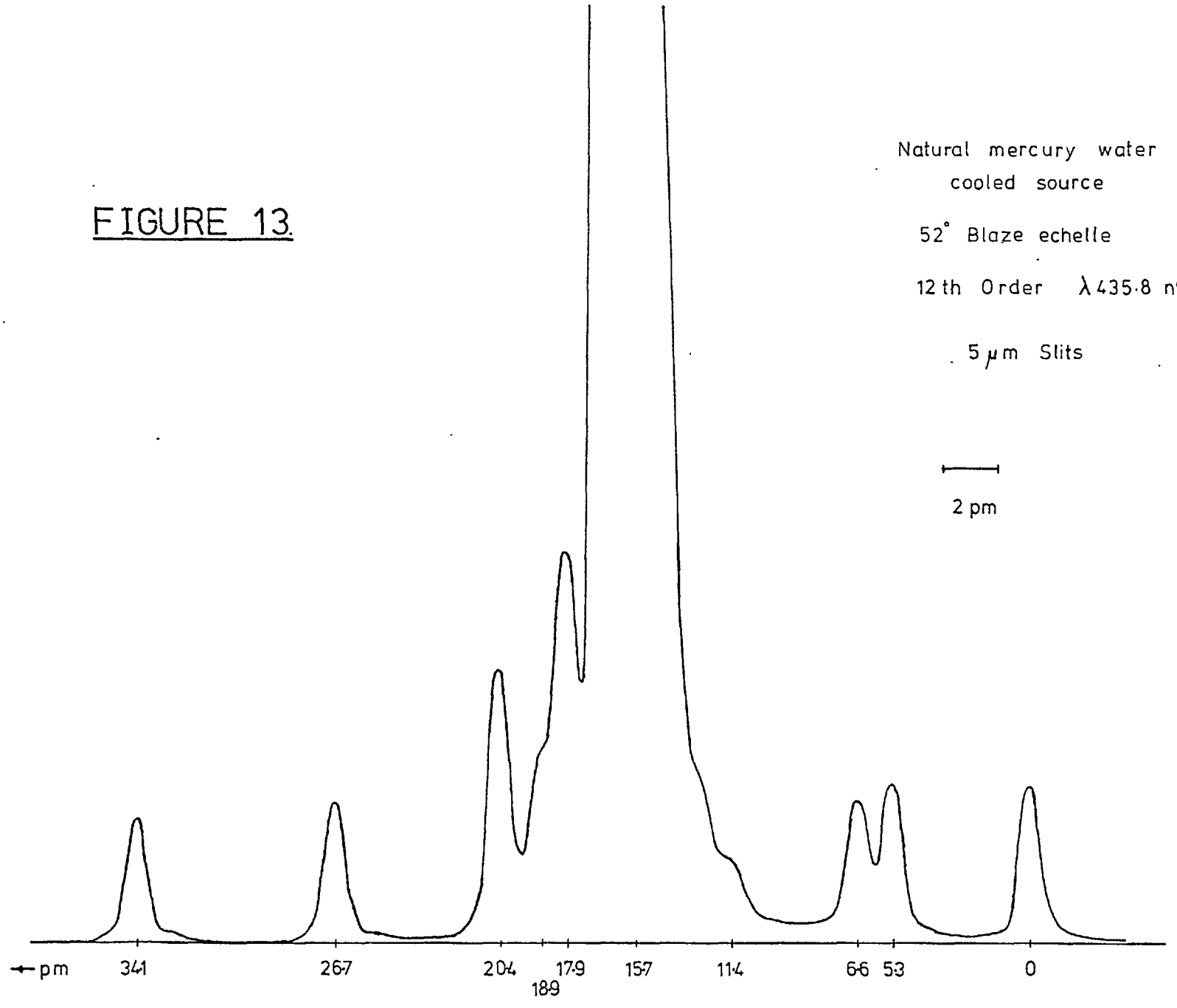
Natural mercury water cooled source
52° Blaze echelle
12 th Order λ 435·8 nm
5 μm Slits
2 pm
←pm
34·1
26·7
20·4
17·9
189
15·7
11·4
6·6
5·3
0

FIGURE 14.

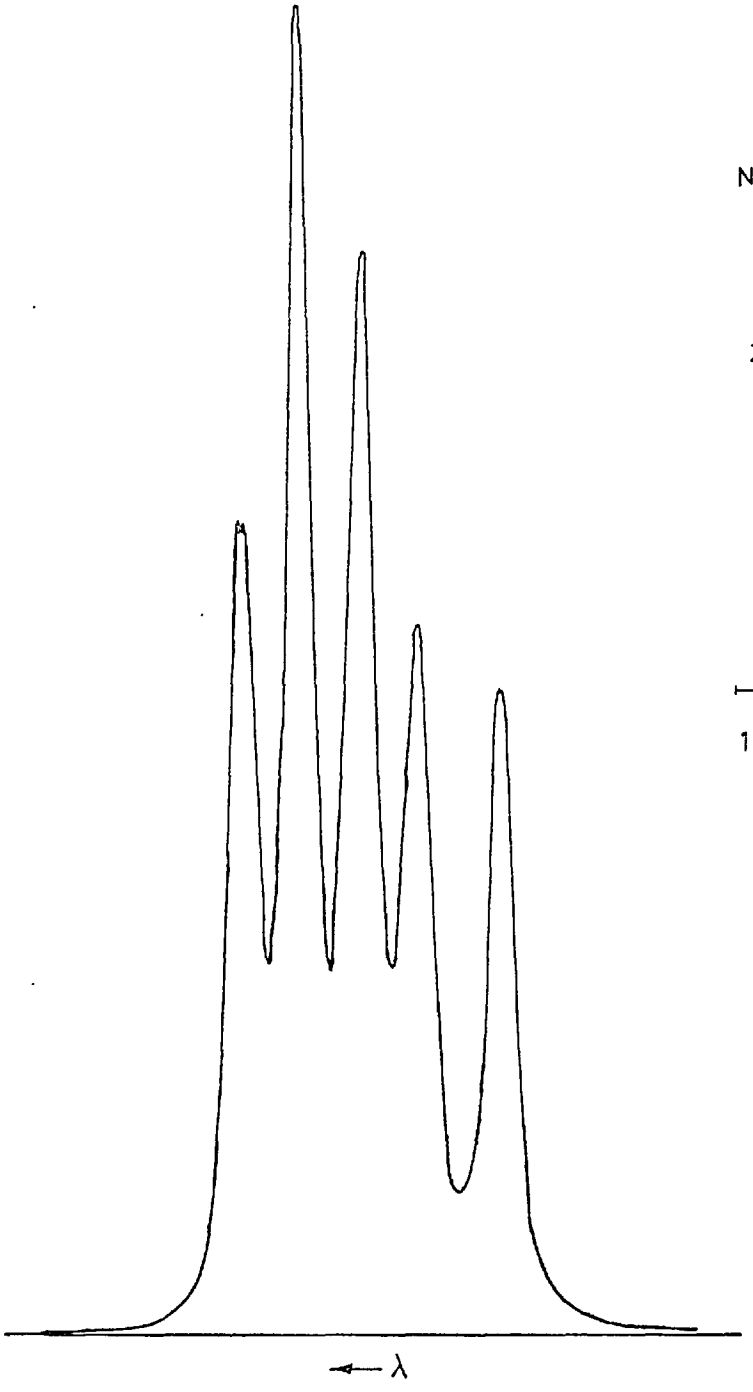

Natural mercury uncooled source

52° Blaze echelle

20 th Order · λ253·7 nm

5 μm slits

1 pm

FIGURE 15.

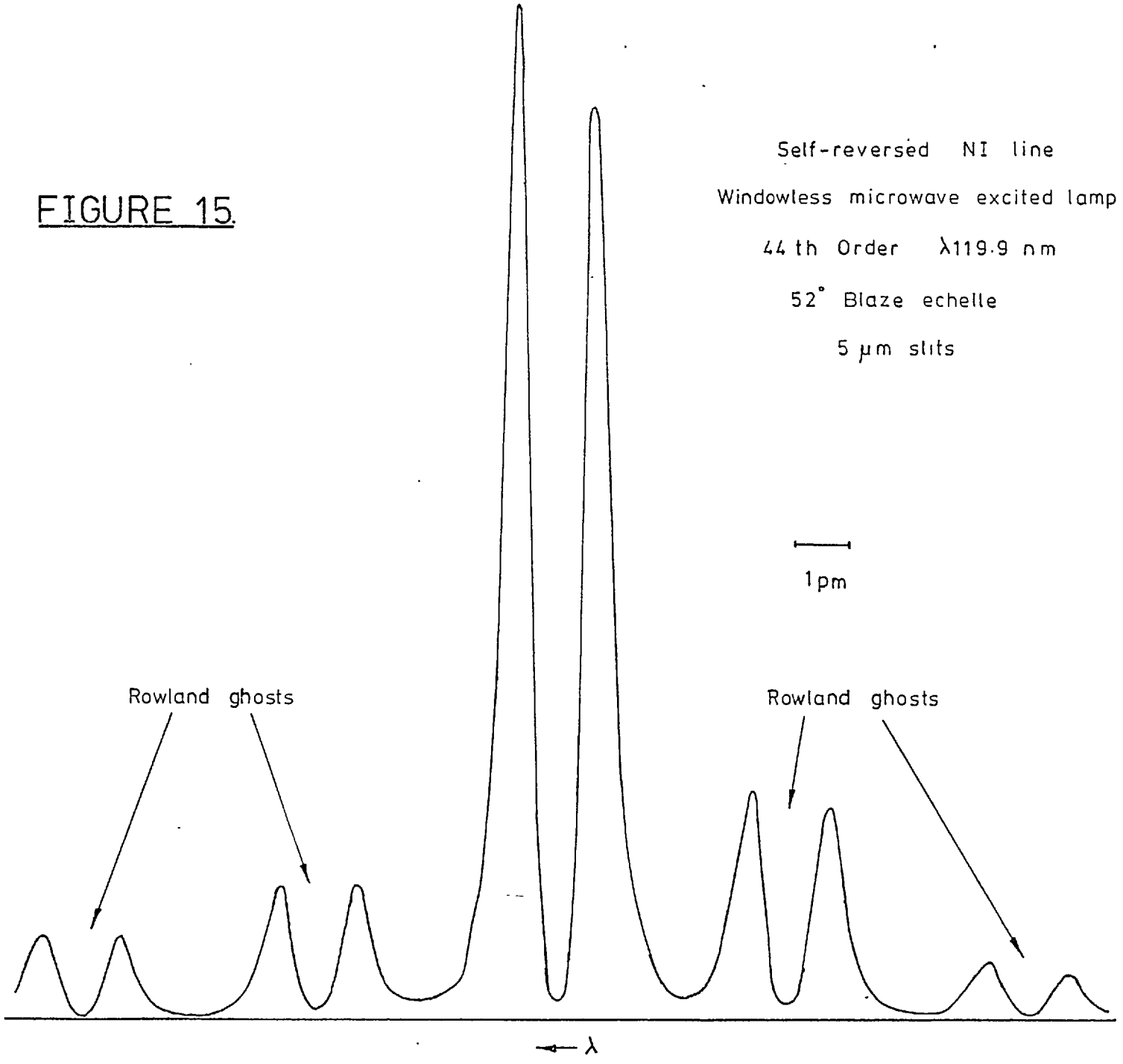
Self-reversed NI line
Windowless microwave excited lamp
44 th Order λ119.9 nm
52° Blaze echelle
5 μm slits
1pm
Rowland ghosts
Rowland ghosts
λ

FIGURE 16.

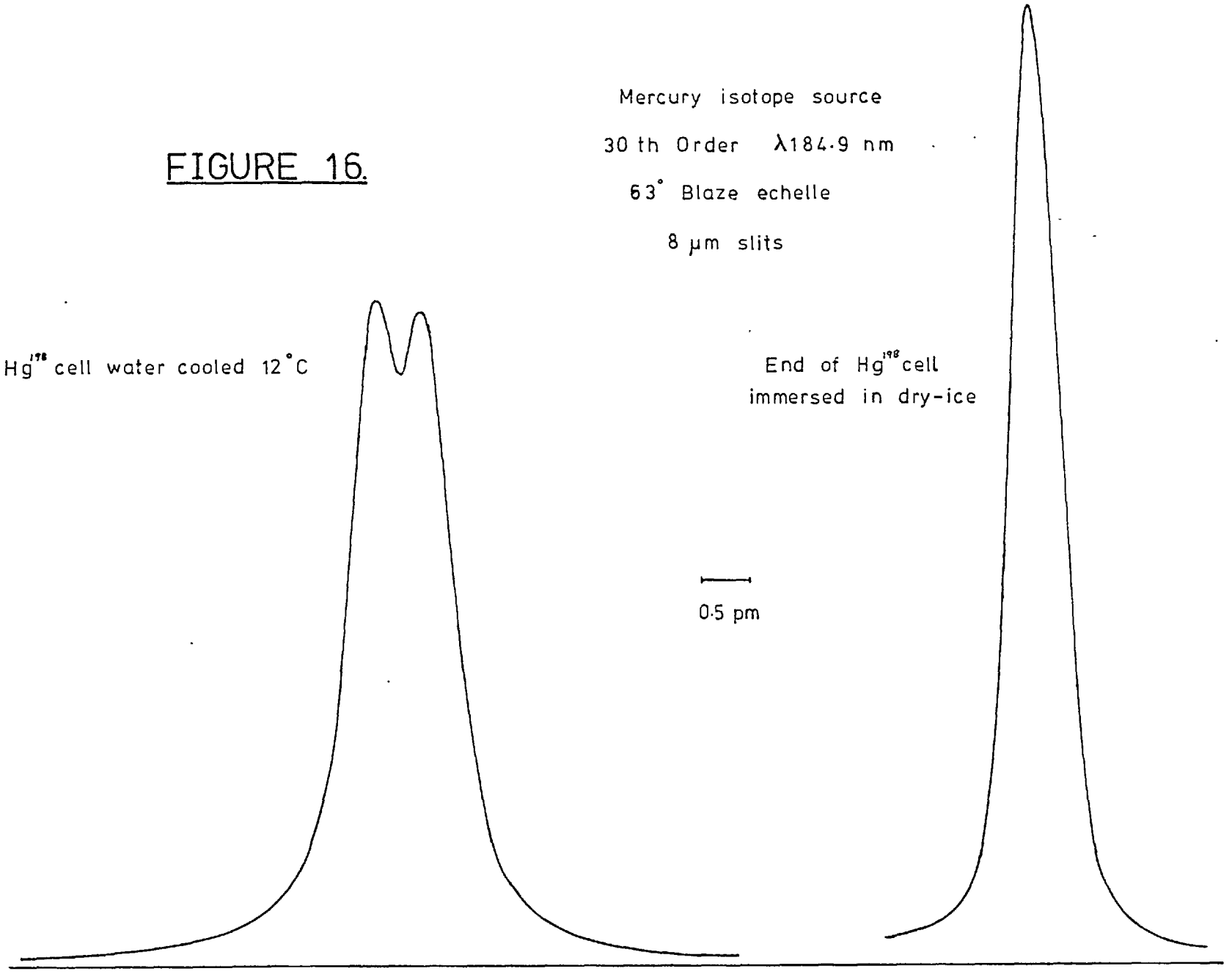
Mercury isotope source
30 th Order λ184·9 nm
63° Blaze echelle
8 μm slits
Hg198 cell water cooled 12°C
End of Hg198 cell immersed in dry-ice
0·5 pm

FIGURE 17.

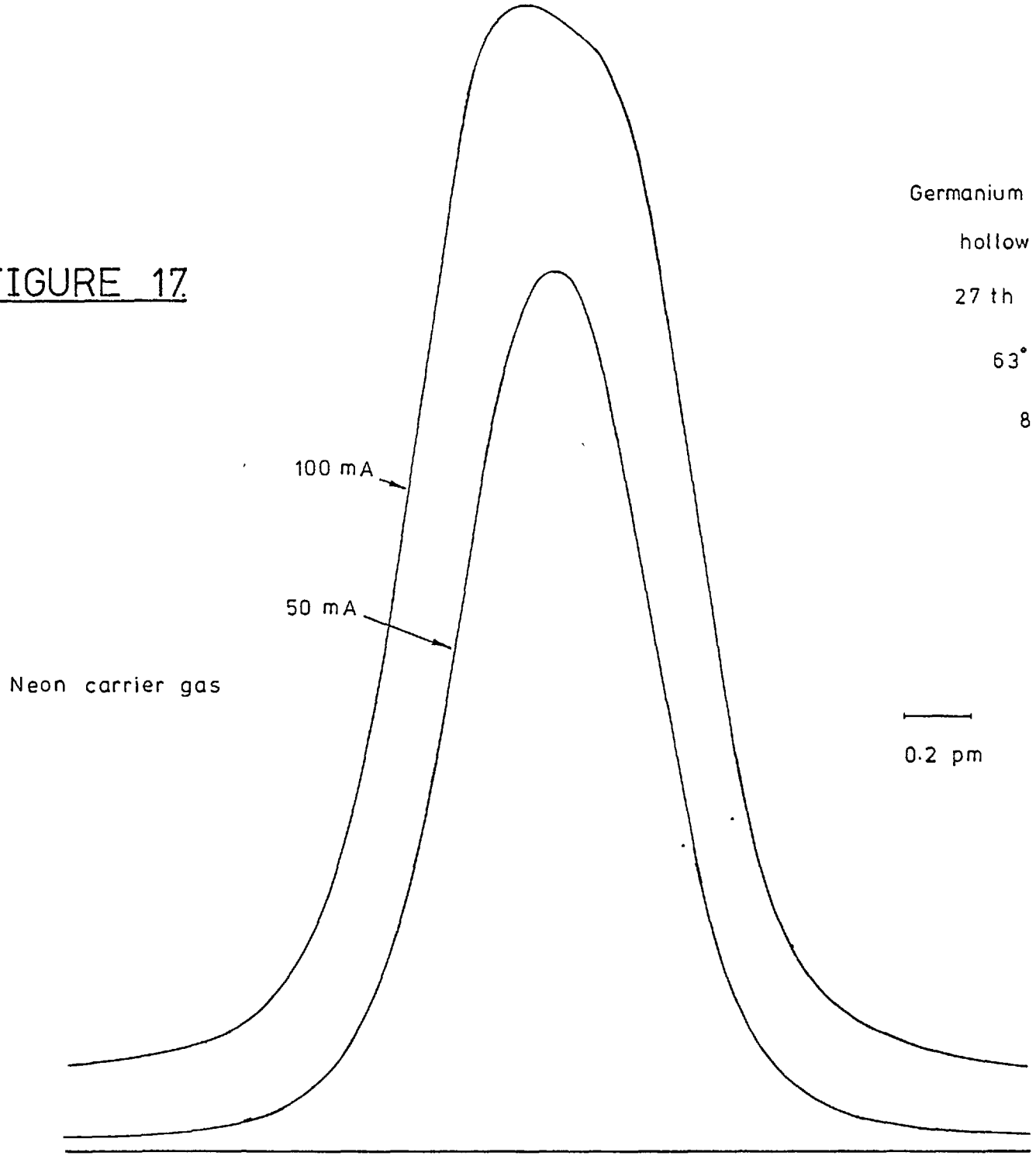
Germanium liquid nitrogen cooled
hollow cathode source
27 th Order GeI λ209.5 nm
63° Blaze echelle
8 μm slits
100 mA
50 mA
Neon carrier gas
0.2 pm

FIGURE 18.

Germanium liquid nitrogen cooled

hollow cathode source

35 th Order Ge II λ160·2 nm

63° Blaze echelle

8 μm slits

Neon carrier gas

Discharge current 50 mA

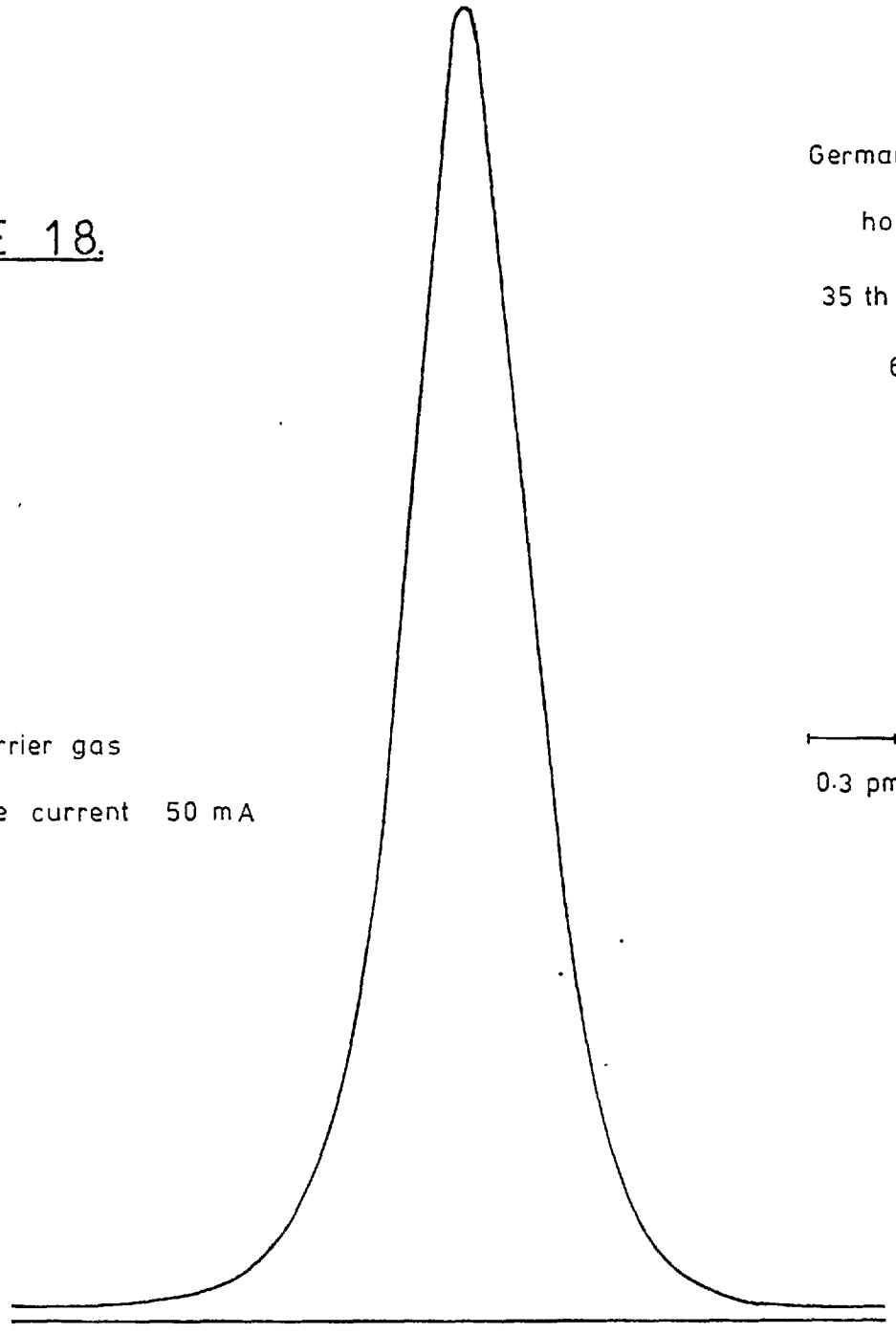

0·3 pm

FIGURE 19.

Germanium liquid nitrogen

cooled hollow cathode source

44 th Order Ge II λ126.2 nm

63° Blaze echelle

8 μm slits

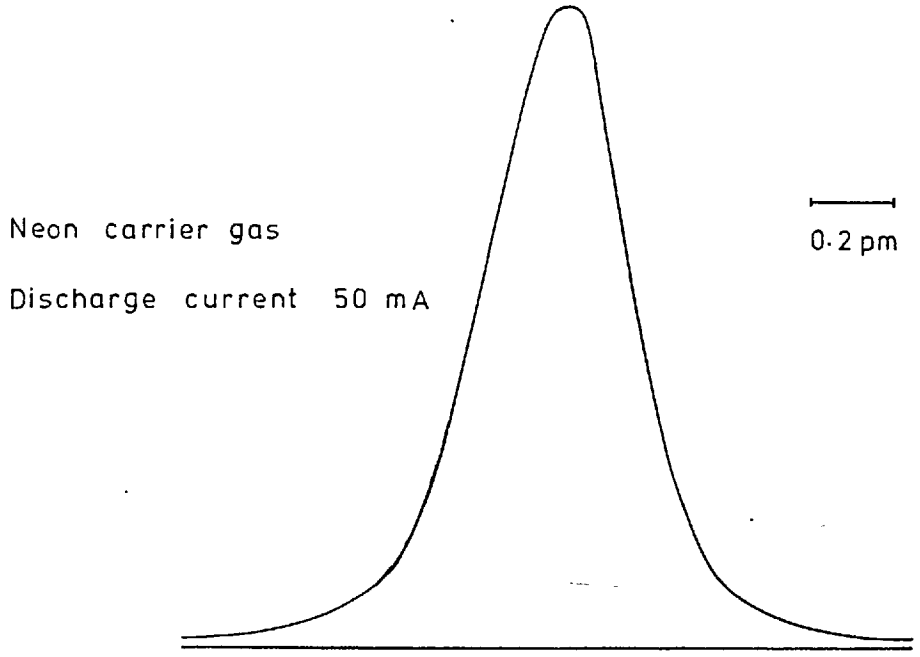

intense to enable the instrumental function to be determined. Various other possibilities were considered in order to obtain a known profile. One method was the possibility of using a rare gas absorption line and another one that of observing a CO molecular transition. The latter would lead to no broadening due to absorption but would still have a large Doppler width.

A plot of observed resolving power versus wavelength for the narrowest observed lines is shown in figure 20. No correction for slits or Doppler broadening has been made. The limit set by the slits is shown by the straight line. This is well below the diffraction limit of resolving power defined by equation (7) which is illustrated as a parabolic variation. The experimental curve is seen to fall off with decrease in wavelength in a manner similar to that predicted by Learner (1968). This is probably a result of the grating and mirror aberrations increasing compared with the wavelength.

The observations of the λ160.2nm line profile of GeII exhibited a small amount of asymmetry as a result of residual geometrical aberrations in the image. The difference between the centre of gravity of the upper 80 to 50% of the line profile and the 80 to 10% was about +0.4 steps i.e. the red wing of the profile was slightly extended.

3.4 Systematic shifts due to spectrometer illumination changes

In the present optical system where, as we have seen, the geometrical aberrations of the optics are important factors in the instrumental profile; illumination of the whole of the optical aperture is essential. Initially, the full grating width and height were used with the entrance beam apertures in the horizontal and vertical directions of f/19.2 and f/15.6 respectively.

A water cooled ^{198}Hg R.F. excited lamp was set up on an x-y co-ordinate table. The discharge confined in a fused silica capillary

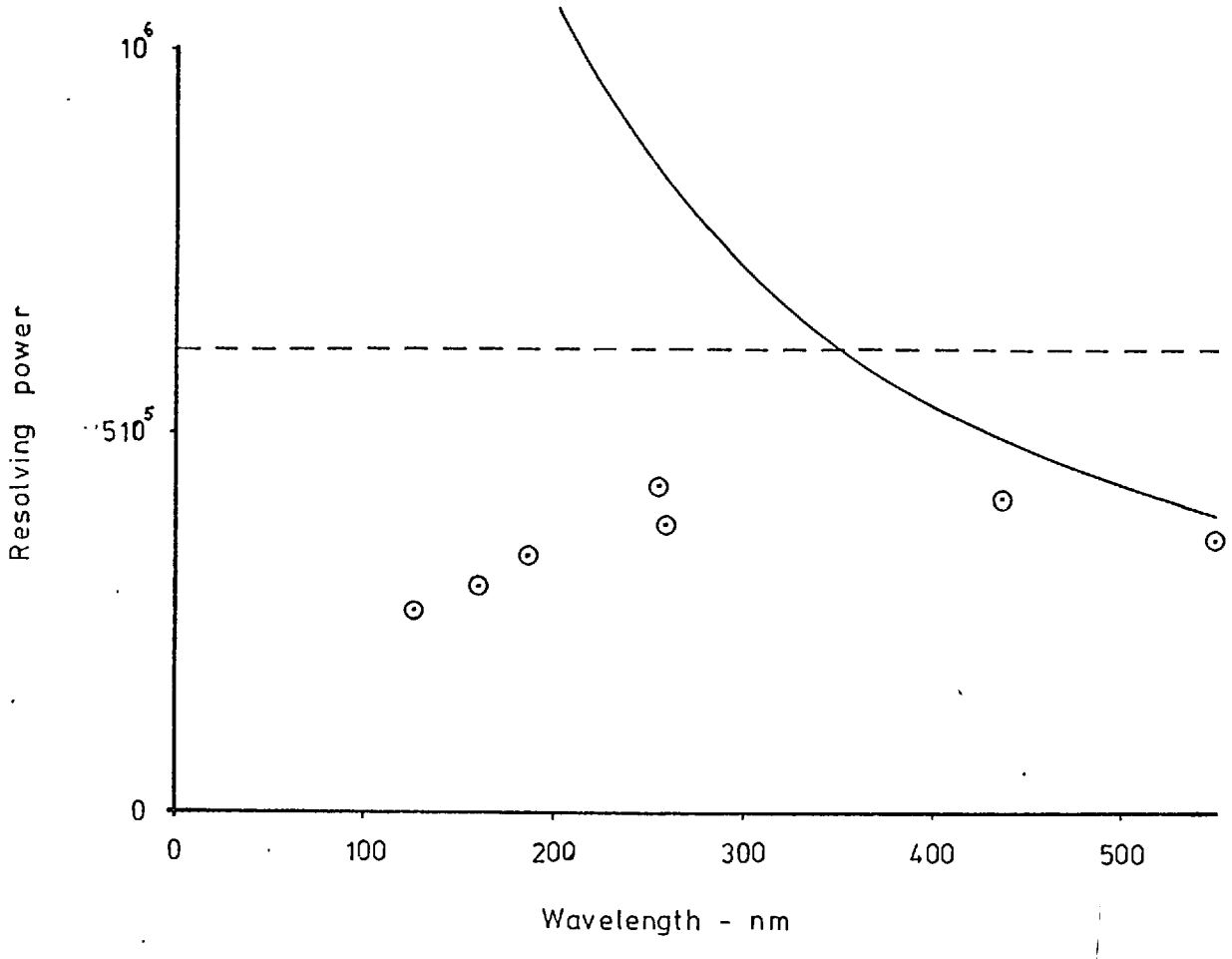

——— Diffraction limit

— — — Slit width limit

⊙ Observed - based on the observed profile full width at half maximum intensity

FIGURE 20. OBSERVED AND THEORETICAL RESOLVING POWER

was between 4 and 5mm diameter and was observed at λ253.7nm. With the source parallel to the entrance slit and 70mm away, the optics was just illuminated in the horizontal (dispersion) plane. Scanning of the source across the aperture showed a parabolic intensity change and a spectral profile shift which could amount to 2 steps (1μm) for 1mm source movement. There was an inflexion in the shift position curve corresponding to the peak intensity. Setting the source 140mm away showed a shift of up to about 2.5 steps per mm source movement.

The source horizontal and scanning in a vertical direction (parallel to the slit) produced a shift of less than 1 step per mm in the focal plane. Here, different parts of the slits are being illuminated although all the optical elements are being filled.

Re-setting the lamp parallel to the slit and fully illuminating the predisperser, the predisperser grating was rotated such that the echelle was not fully illuminated. Change of illumination from one side of the echelle to the other, with a change of 50% in intensity of the peak of the profile, showed an overall shift of about 3 steps.

Measurements of these systematic shifts showed that large errors could arise in the absolute position of the line profile as a result of optical illumination changes. During these investigations problems were experienced with positive column striations which tended to 'run' along the tube especially when the oscillator current was changed. Care had to be exercised in order to ensure these did not occur during measurements.

In order to test the suitability of the system for measurement of relative wavelength shifts when the source was run under different excitation conditions, a number of shifts of λ253.7nm profile were obtained for change of oscillator current from 71-88mA. This current change corresponded to 25% intensity change. Offsetting the source, to reduce the profile intensity by 15%, was found not to change the

relative shift due to current change by more than 0.1 steps. Using cooling water temperatures of 7.1°C and 15.1°C the overall shift with current change was found to be 0.3 ± 0.1 steps and 0.5 ± 0.1 steps respectively, corresponding to red shifts of 4 and 6.5 parts in 10^8. The uncertainties quoted only refer to the repeatability of the set of measurements made. The shifts are probably caused by self-absorption in the lamp. A similar shift result was obtained when the lamp was used horizontally. Analysis of the results showed that the upper half of the profile shifted less than the lower half i.e. the asymmetry of the profile increased with increase in discharge current (red wing increased in intensity).

During the course of these measurements, problems of temperature stability of the spectrometer were encountered. The thermal drift rate of the image was typically 0.05 steps/minute, which was too large. Consequently, a temperature control system was built and installed as already described in section 2.8.

The results obtained with the λ253.7nm line for both systematic shifts and spectral shifts lead to the following conclusions:-

1. The absolute position of the spectral line is strongly dependant on optical illumination.

2. Provided the relative illumination of different parts of the optics are not affected by discharge conditions, wavelength shifts can still be evaluated successfully.

3. Provision for focussing the source onto the entrance slit would improve the problem with respect to relative changes in discharge conditions, but the further reflection would reduce the overall efficiency.

At this point in the measurements it was clear that investigations of systematic shifts must be undertaken with the source whose wavelength

shifts are to be investigated. This is because the spatial variation of intensity in the ^{198}Hg lamp and the proposed cylindrical hollow cathode source are vastly different. The first has cylindrical symmetry parallel to the slit length whilst the other has it normal to the slit length and dispersion plane, where we assume observations are made along the hollow cathode axis of symmetry. Positive column striation instability in the R.F. source also leads to the possibility of errors.

The germanium hollow cathode lamp (described later in section 5.1) was attached to the spectrometer by an adaptor plate which, by the use of a sliding o'ring seal, allowed the source to be translated horizontally and vertically across the field of view, thus altering the spectrometer illumination. A magnesium fluoride window separated the lamp from the adaptor plate.

Observations of the λ160.2nm line of GeII were now undertaken. Considerably lower signals were observed compared with the HgI λ253.7nm line (ratio of about 400 when the hollow cathode was run at 50mA and using 0.6 torr of neon as carrier gas). During the following period of about 9 months, various measurements were made to ascertain the source of possible systematic shifts to be encountered in the hollow cathode as a result of illumination changes in the spectrometer. Some of these will now be summarised.

Initially the whole of the echelle aperture was used with no limitation on slit height. This meant that the region of the source observed was a 3mm wide slice over the whole of the hollow cathode diameter (10mm) parallel to the entrance slit. Using neon as a carrier gas, the wavelength shifts corresponding to various neon pressure changes were observed for different translations of the lamp. No systematic shift was observed greater than about 0.3 steps. However, the grating

width was restricted to 120mm, thus reducing the effective aperture in the dispersion plane at the predisperser entrance slit to f/30 and the effective source width to 2mm. Restriction of the grating width did not appear to degrade the observable resolving power of the spectrometer.

A set of wavelength shifts corresponding to a discharge current change from 50 to 100mA were made for neon as a carrier gas at a pressure of 1.5 torr. When the source was translated through a distance of about 3mm perpendicular to the slit, any systematic shift present was found to be less than 0.3 steps. The centre of gravity of the profile for 0.6 torr carrier gas pressure was found to vary by less than 0.15 steps for the 3mm source movement.

Using argon as a carrier gas a large number of wavelength shift measurements were made for a change in discharge current of 50-100mA with 1.16 torr of argon. Translation of the source through about 5mm perpendicular to the entrance slit yielded a scatter of 0.6 steps in the measurements but indicated no systematic shift present greater than 0.3 steps. A second similar set of data showed systematic shifts less than 0.2 steps.

During all the previous measurements, the predisperser had always been set such that maximum intensity was observed when the exit slit was centred on the line profile. The change in predisperser output intensity with predisperser wavelength setting did not exhibit a broad flat peak, this is because the image of the predisperser entrance slit on the main spectrometer slit was probably not wide enough. At this point, a wavelength shift for neon pressure change at three different predisperser grating rotations (illuminating the

echelle differently) was evaluated. These differed from each other by a factor of 2.5. At the time it was not realised how significant it was that helium had been used in the hollow cathode lamp prior to doing this test. It will be seen later that the desorption of helium in the lamp probably caused the large discrepancy between the different results. However, it was decided to increase the width of the predisperser entrance slit from 0.1 to 0.15mm and reduce its height to 2mm. Flat-topped output intensity of the predisperser was obtained and this also restricted the observations of the hollow cathode to the central region 2mm wide and 6mm high. Changing the predisperser grating rotation was found to change the wavelength shift results by less than 0.3 steps.

Apart from the controlled changes of the source translation and predisperser settings, many changes of parameters arose from the following procedures:-

Removal of the lamp to clean the magnesium fluoride window. Replacement of the lamp to within ± 1mm was accomplished and the setting optimised by scanning the lamp across the entrance aperture whilst monitoring the peak of the predisperser output. The change in intensity over the central 3mm movement was less than 3%.

The predisperser was re-set after monitoring another wavelength and its setting optimised using the same technique as for the lamp translation.

Rotation of the echelle and re-positioning after observing other wavelengths.

Re-focus of the exit slit system.

As a result of these changes and settings, it was concluded that if

systematic errors are present then they are probably less than 0.3 steps in most measurements. Signal to noise limitations prevent the absolute determination of their magnitude. It must be realised that any systematic errors in the pressure and current change versus shift curves given later are probably a result of discharge spatial changes as well as any inherent instrumental limitation.

An assessment of all the measurements undertaken leads to the conclusion that an uncertainty of $\pm$ 0.4 steps must be assigned to the mean shift observed at the maximum pressure in the pressure change versus wavelength shift curves given later in order to allow for systematic and random errors. The uncertainty in the case of the current change versus wavelength shift is probably about $\pm$ 0.3 steps.

CHAPTER 4

GERMANIUM WAVELENGTH STANDARDS

In this chapter, the reasons for using germanium emission lines as wavelength standards are given with special emphasis on the first ionised spectra because most of the emission lines occur in the vacuum ultraviolet. The history of wavelength measurements in germanium is given with a brief description of methods and equipment used. Results of measurements on the ground-state doublet, λ160.2nm and λ164.9nm, in GeII will be given in detail and the unsatisfactory state of the measurements will be indicated.

4.1 The suitability of germanium as a source of wavelength standards

A suitable emission secondary wavelength standard must satisfy a number of criterion:-

1. Possess a number of reasonably well separated lines throughout the wavelength range of interest. The first ionised spectra of germanium has multiplets at λ109, 116, 124, 154, 160, 194, 196nm.

2. Easily excited, with sufficient intensity, in a simple discharge tube. This has been shown to be the case in the present work.

3. Be sufficiently heavy atom to minimise the Doppler width to a tolerable level (say $\frac{\Delta\lambda}{\lambda} \simeq 2.10^{-6}$) when cooled to liquid nitrogen temperatures. For germanium, with atomic weight A = 72 and at 77K, we have:-

$$\frac{\Delta\lambda}{\lambda} = 7.4.10^{-7}.$$

Although it is unlikely that this value could be achieved, the Doppler width is sufficiently small.

4. Either exhibit minimum observable hyperfine structure or isotope shift in the elements naturally occurring state or be

available as an isotope with even atomic weight, A, and even atomic number, Z.

Hyperfine structure arises from the combination of the nuclear spin angular momentum with the electronic angular momentum. Nuclear spin is zero when A and Z are even. However, isotope shifts can arise from the finite nuclear mass changing the electronic energy levels (mass shift); the effect decreases rapidly with increase in mass. Different isotopes have different nuclear charge distributions which can also give rise to electronic energy level shifts (field shift); this effect increases with atomic weight.

Germanium has Z = 32 and four even atomic weight isotopes with A = 70, 72, 74 and 76 and a single odd isotope with A = 73 of abundance 7.8% and nuclear spin 9/2. Isotope shifts would be expected to be small because of its position in the periodic table. Very high resolution work in the visible wavelength range has shown that both these effects are very small as will be discussed later.

5. Exhibit a wavelength and line profile which are not strongly dependant on source conditions. This will be discussed later for the case of germanium.

Figure 21 shows an energy level diagram and illustrates that most of the observable vacuum ultraviolet transitions in GeII are transitions to the ground state doublet $4p^2\ ^2P_{1/2,3/2}$. These lines are expected to suffer from self-absorption and self-reversal as will be discussed later. A history of wavelength measurements in the spectrum of germanium will now be given to show the progress that has been made in the past.

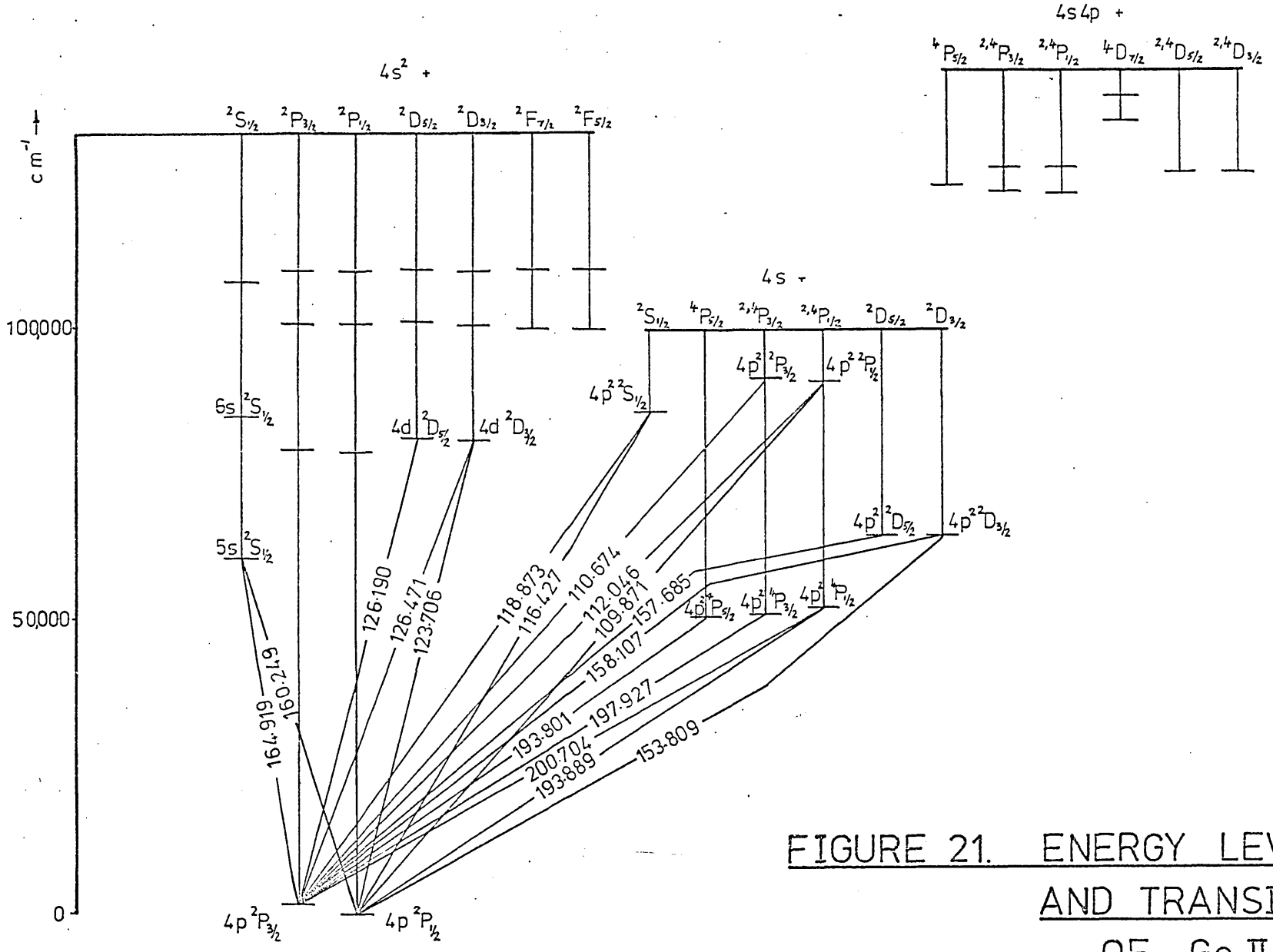

FIGURE 21. ENERGY LEVELS AND TRANSITIONS OF Ge II

4.2 History of germanium wavelength measurements

The energy levels of neutral germanium (referred to as the arc or first spectra and GeI) are such that all are accessible from observations of transitions in the visible wavelength region. Hence, the vacuum ultraviolet wavelength region transitions are directly calculable using the Ritz combination principle. The first ionised spectra (spark or second spectra, GeII) has its ground terms which are only accessible by observation of vacuum ultraviolet transitions. Hence, direct measurement of at least two lines in the short wavelength region is essential. However, the separation of the ground term can be obtained from series limits in the GeI spectra.

Very early measurements on the GeI spectra were undertaken by Rowland and Tatnall (1895), Richter (1928), Gartlein (1928), Rao (1929), M.I.T. (1939), Kiess (1940) and Van den Bosch and Klinkenberg (1941). There was poor agreement between the different observations. Deverall et al. (1954) used an atomic beam to investigate isotope shifts and obtained some very precise measurements of a few visible and near ultraviolet wavelengths. The GeII spectra was first investigated by Lang (1928, 1929), Rao and Narayon (1928), Kiess (1940) and extended by Gartlein (1950) which formed the basis of data given by Moore (1952).

Van Veld and Meissner (1956) measured forty-three GeI lines between λ201.9 and λ468.5nm using a Fabry Perot interferometer. They used a hollow cathode lamp to excite the spectra run with neon or helium as carrier gases with currents between 20 and 200mA. The standard line used was the λ546.07532nm line of ^{198}Hg excited in a Meggers' electrodeless discharge tube run at 250 MHz. Using these measurements to obtain energy levels, the Ritz combination principle was applied to calculate twenty-nine lines between λ169.1 and λ199.8nm with an estimated uncertainty of $\pm$ 4.10^{-5}nm. A comparison of six wavelengths between λ259 and λ327nm obtained with the hollow cathode

and the atomic beam (Deverall et al. (1954)) showed differences of between - 8.10^{-6}nm and + 16.10^{-6}nm. Another interesting measurement made was seven determinations of the wavelength of λ422.7nm using different sources and instruments. The total scatter of the results was only 2.10^{-5}nm.

Andrew and Meissner (1957, 1958) extended the vacuum ultraviolet calculations to 84 lines, with the addition of some further visible and infrared wavelength measurements. Meissner et al. (1958) actually compared the calculated vacuum ultraviolet lines with accurate measurements using the University of Chicago 21 ft. concave grating spectrograph. The same type of hollow cathode lamp was used, run at 160mA and with neon as carrier gas at a pressure of 1 torr. With an uncertainty of ± 2.10^{-4}nm, agreement with the Ritz standards was obtained with the exception of about 9 lines which, for various reasons, were rejected. Using the GeI standards, measurement of 12 GeII lines was made which included the λ164.9nm and λ160.2nm ground state transitions.

Their results were:-

$$164.9191 \pm 2.10^{-4}\text{nm}$$

$$160.2485 \pm 2.10^{-4}\text{nm}.$$

A very extensive investigation of GeI was carried out by Andrew and Meissner (1959a) from λ154.6 to λ1125.2nm using concave grating instruments and interferometers. Various arc and hollow cathode sources were employed to excite different regions of the spectrum. This work brought the total number of GeI lines to 475 with the determination of 94 new energy levels.

The spark spectra of germanium between λ474 and λ715nm was measured by Andrew and Meissner (1959b). A germanium low pressure arc as used in the previous work on GeI (Andrew and Meissner (1959a)) was

used in conjunction with the 30 ft. concave grating instrument at Purdue and with a Fabry Perot interferometer which produced accuracies of $\pm 3.10^{-3}$ and $\pm 5.10^{-4}$nm respectively. The main purpose of the work was for energy level determinations and term analysis.

Further very accurate measurements in the arc spectra were made in the infrared between λ1125.5 and λ1928.4nm by Humphreys and Paul (1960, 1961). Kaufman and Andrew (1962) have made extensive very accurate measurements between λ422.7 and λ1200nm. They used a high frequency electrodeless lamp with germanium halides or germanium oxide and a carrier gas to excite the lines. Fabry Perot interferometers were used for the measurements and the green ^{198}Hg line was used as standard. Data was given on the shift of the 6p energy levels obtained from wavelength measurements on eight different lamps with respect to the hollow cathode. Shifts of up to 0.035cm^{-1} were observed with GeI_4 and xenon at 2.8 torr as carrier gas, whereas a shift of less than 0.005cm^{-1} was observed with $GeBr_4$ and neon at 46 torr, but double this was observed with 4 torr. Vacuum ultraviolet Ritz standards were calculated to give uncertainties as small as $\pm 3.10^{-5}$nm and these results represent the foundations of most vacuum ultraviolet measurements undertaken since. Twenty-three GeII lines were also measured and new energy levels and wavelengths in the vacuum region were calculated based on the $4s^2\,5s\ ^2S_{1/2}$ level taken from the work of Wilkinson and Andrew (1963), which was unpublished at the time. Estimated uncertainties (not including that of the vacuum ultraviolet measurement) of the calculations produced new wavelengths to better than $\pm 9.10^{-5}$nm.

Shenstone's (1963) work on the term analysis of GeII using hollow cathode and spark sources produced the essentially reference work on intensities and classification. The 21 ft. spectrograph at Princeton was used in conjunction with a hollow cathode run at currents

as high as 2.2A and a spark source. Measurements were made between $\lambda 60$ and $\lambda 1000$nm and enabled many more Ritz standards to be calculated in the vacuum ultraviolet.

Wilkinson and Andrew (1963) made measurements of GeII lines excited in both cooled and uncooled hollow cathode lamps with a 21 ft. spectrograph. The GeI lines given by Kaufman and Andrew (1962) were used for calibration purposes which led to uncertainties of $\pm 2.10^{-4}$nm above $\lambda 235$nm and $\pm 1.10^{-4}$nm below $\lambda 204$nm. Ground-state splitting of the $4p\ ^2P_{1/2,3/2}$ level was obtained from the $\lambda 200.7$nm and $\lambda 193.8$nm lines as:-

$$1767.36 \pm 0.03\text{cm}^{-1}$$

and the $5s\ ^2S_{1/2}$ level was found to be:-

$$62403.11 \pm 0.03\text{cm}^{-1}.$$

Ritz standards below $\lambda 160$nm were calculated based on the wavelength measurements. Final results for the ground-state doublet of interest were:-

$$164.91920 \pm 1.10^{-4}\text{nm}$$
$$160.24841 \pm 1.10^{-4}\text{nm}.$$

The arc spectrum of silicon (SiI) was investigated by Radziemski and Andrew (1965). Various sources were used for the excitation of different wavelength regions, these included a hot hollow cathode (run at 800mA with 10-20 torr of helium or neon), microwave lamp, and an arc type source, the latter run up to 1 atmosphere. For the latter, source level shifts with carrier gas pressure were presented. GeI lines, as given by Kaufman and Andrew (1962), were used as standards on the grating instruments used. Ritz standards for SiI were calculated with uncertainties less than 2.10^{-4}nm in the vacuum ultraviolet.

Kaufman, Radziemski and Andrew (1966) used the N.B.S. 10.7m

Eagle spectrograph to measure the vacuum ultraviolet emission spectra of SiI. They used 2450 MHz excited sources with $SiCl_4$ and and $GeCl_4$ and a carrier gas of argon/helium mixture. Between λ164 and λ210nm, GeI lines were used as standards. As a result of this work, other wavelengths, including the λ164.9nm line of GeII, which appeared strongly, were also measured. Their determination was:-

$$164.91943 \pm 1.10^{-4}\text{nm}.$$

SiI measurements were compared with the calculations of Radziemski and Andrew (1965) and most were found to agree to within $\pm 1.10^{-4}$nm whilst the rest were within $\pm 2.10^{-4}$nm. It was thought that Stark shifts were responsible for some of the deviations. This work showed that there did not appear to be any systematic shifts between the $GeCl_4$ electrodeless lamp wavelengths used as standards and the GeO and $GeBr_4$ and hollow cathode lamp used for the GeI Ritz standards of Kaufman and Andrew (1962).

Kaufman and Ward (1966) used a water cooled copper hollow cathode lamp containing germanium and silicon in conjunction with the N.B.S. 10.7m Eagle spectrograph to measure the CuI and CuII spectra. Helium carrier gas, at pressures between 1 and 4 torr, was used with traces of nitrogen and/or carbon dioxide to bring out the germanium and silicon spectra. Discharge currents between 300 and 600mA were employed. GeI lines of Kaufman and Andrew (1962) were used as standards as well as CuII and SiI lines. A direct measurement of the two GeII lines yielded:-

$$164.91942 \pm 10.10^{-5}\text{nm}$$

$$160.24864 \pm 6.10^{-5}\text{nm}.$$

As a result of measurements of other GeII vacuum ultraviolet lines, new calculations were made to determine these two wavelengths, using data from Kaufman and Andrew (1962), Wilkinson and Andrew (1963)

and Shenstone (1963), which yielded:-

$$164.91942 \pm 6.10^{-5}\text{nm}$$

$$160.24863 \pm 6.10^{-5}\text{nm}.$$

The splitting of the ground state term $4p\ ^2P$ was found to be:-

$$1767.356 \pm 0.005\text{cm}^{-1}$$

which agreed with the value found by Wilkinson and Andrew (1963). This work represents the latest on GeII. The last two measurements of the λ164.9nm line (those of Kaufman, Radziemski and Andrew (1966) and Kaufman and Ward (1966)) used the same spectrograph and yielded wavelengths remarkedly similar to each other despite the fact that microwave excitation was used in one case and water cooled copper hollow cathode used in the other. They both differ by about 2.10^{-4}nm from the previous measurement of Wilkinson and Andrew (1963) where hollow cathodes were used (no data on operating conditions was specified but was probably similar to the work of Van Veld and Meissner (1956)). All of these measurements rely on the GeI lines in the vacuum ultraviolet calculated by Kaufman and Andrew (1962).

Recently, Minnhagen (1971), measured the wavelengths of ArII lines on the N.B.S. 10.7m spectrograph excited in a high frequency pulsed source. The GeI standards of Kaufman and Andrew (1962) were used in the calibration of the spectrograph. Kaufman and Minnhagen (1972) have used a similar source and the same spectrograph to measure the NeI spectra. Various systematic shifts were observed, which were as large as 3.10^{-4}nm, between the GeI lines and ArII. All vacuum ultraviolet wavelength standards rely on Ritz combination principle calculations and are only indirectly traceable to the primary ^{86}Kr standard. Information on the suitability of spectral lines as wavelength standards and the shifts with source conditions is very sparse. It is evident that direct measurements with respect to the primary

standard would yield very much more reliable and accurate wavelengths. However, their suitability must first be established, it is with this in mind that the echelle spectrometer was constructed.

CHAPTER 5

EXPERIMENTAL RESULTS

The design and construction of a liquid nitrogen cooled hollow cathode lamp is described for the excitation of the GeII spectra. Results of measurements on important lines in the vacuum ultraviolet are given and show extremely small wavelength shifts, less than 1.5 parts in 10^7, with change in source operating conditions.

All measurements made with the hollow cathode lamp were systematically tabulated. This included operating conditions and the running time. The use of such a record proved extremely valuable when examining the possible sources of wavelength shifts.

5.1 The hollow cathode lamp

A number of different designs of hollow cathode lamp, whose cathode was capable of being cooled to liquid nitrogen temperatures (77K), were constructed. Problems of sealing the cathode holder to a cooling system and still maintain a vacuum-tight seal represented the major difficulty; combined with the requirement of having the cathode close to the spectrometer entrance slit (about 60mm separation). The simplest form developed was found to be the most satisfactory and consisted of a glass to Kovar seal with a copper plug, silver soldered to the Kovar, to hold the cathode.

Figure 22 shows the hollow cathode lamp used on the echelle spectrometer. The cylindrically symmetrical anode-cathode is viewed along the axis of symmetry through the anode. The cathode is a germanium block made by melting germanium in a graphite crucible, under vacuum, using an induction furnace. After being cast, the block was ground to its final size with a bore of 10mm diameter. Although the carbon multiplet at λ165nm was observed as an impurity in the spectra it was never very strong. The anode consists of 2mm diameter aluminium

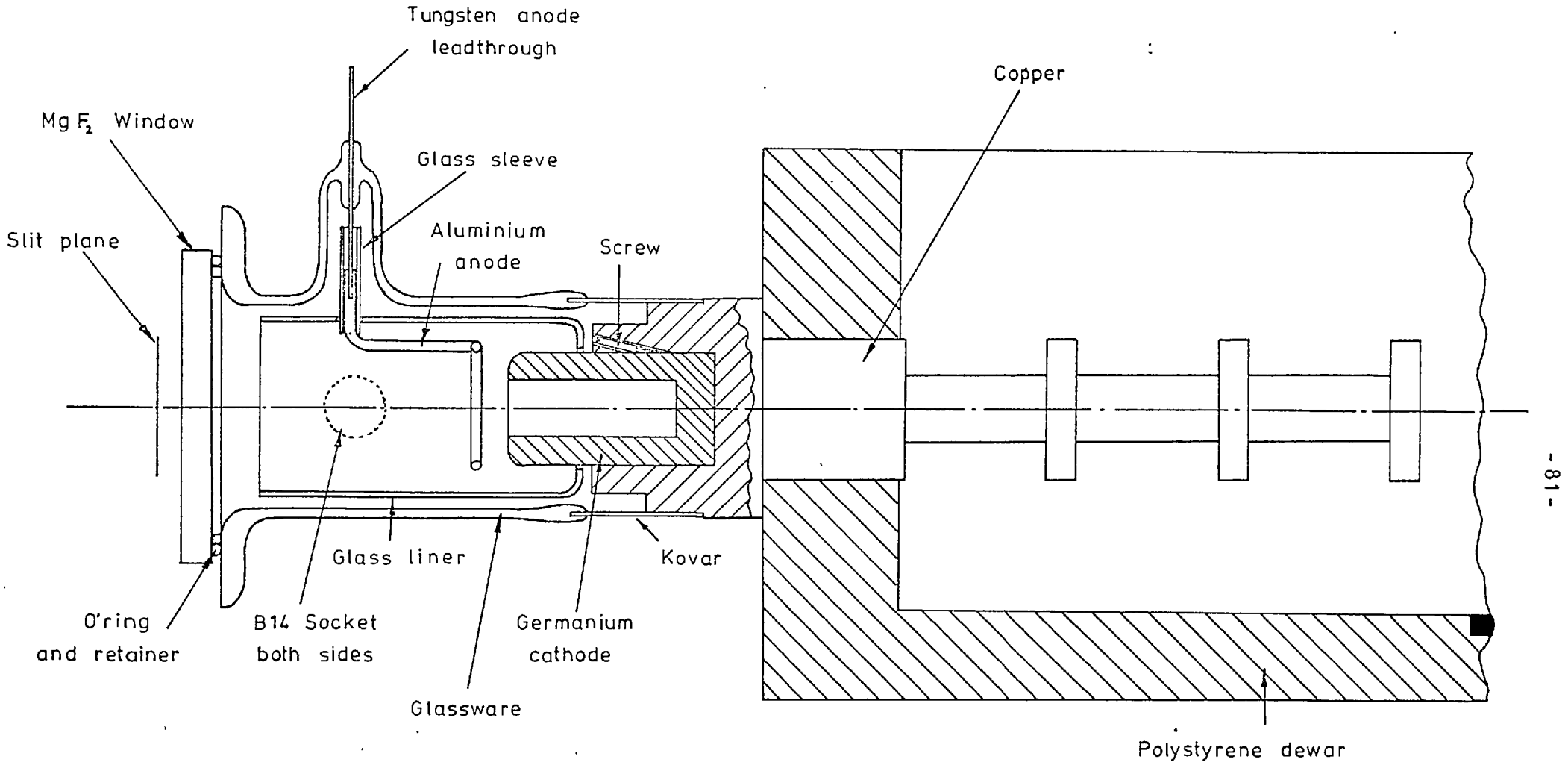

FIGURE 22. LIQUID NITROGEN COOLED GERMANIUM HOLLOW CATHODE LAMP

wire bent into a ring of internal diameter 20mm and placed 4-5mm from the cathode. A tungsten electrical lead-through held the anode in position. Cooling of the cathode is accomplished by inserting the copper fins, which are an extension of the block holding the germanium, through a hole in the side of a polystyrene dewar, which could be filled with liquid nitrogen. To prevent discharges occurring on the copper, a glass sleeve between the anode and cathode is used.

A magnesium fluoride window separated the lamp from the spectrometer and the whole system was mounted on an o'ring seal slide to allow the source to be translated horizontally and vertically. The distance between the cathode and slit was 60mm, which was sufficiently small to adequately fill the optics using the 10mm diameter cathode hole.

Continuous flow of carrier gas was maintained through the lamp in order to reduce the accumulation of impurities, and to enable the pressure to be changed quickly with the aid of an automatic pressure controlled needle valve in the gas supply line. A rotary vacuum pump was connected to the lamp, via glassware and a 1mm orifice tap. An Edwards model 9 pirani gauge was used to measure the carrier gas pressure and to supply the automatic pressure controlling needle valve with a voltage which was approximately proportional to the pressure. The pirani head was calibrated at N.P.L. although, after initial pressure versus wavelength shift measurements had been carried out, it was realised that the accuracy of absolute pressure measurement to ± 10% was more than adequate. However, calibration did show that the stability of the gauge as a transducer could be relied upon to ± 5% over a period of one year and the reproducibility of the gauge over a day was within ± 2%. Overnight evacuation of the lamp was accomplished using a small getter apendage pump. This pump was also used to pump impurities in the gas supply during the operation of the

hollow cathode lamp.

The impurity present in the carrier gases used was stated by the suppliers*, in volume parts per million (unless otherwise stated), as:-

Gas Impurity	neon	argon	helium
helium	2%	-	-
nitrogen	5	30	30
oxygen	5	6	20
hydrogen	2.5	1	1
carbon dioxide	2.5	1	2
neon	-	-	10
water	-	5	7
hydrocarbon	2.5	-	5

Using the lamp with the cathode run at close to liquid nitrogen temperatures, very few impurity lines were observed except in the case of helium being present in neon in small quantities. As will be discussed later, the helium appeared to be absorbed by the germanium during the times that it was used as a carrier gas. Desorption took place at a higher rate when the lamp was subsequently used with either argon or neon as carrier gas.

During operation at high gas pressures anode glows could appear. There was no evidence of any correlation between changes in the output intensity of the negative glow and the onset of such anode glows. They are probably caused by surface irregularities on the anode or possibly by impurities. It was usually found that the lamp would exhibit these effects if it had not been evacuated thoroughly since the

* B.O.C. LTD.

previous time it had been used, but they soon disappeared after some minutes of running.

Using the continuous carrier gas flow, the total gas throughput at a lamp pressure of about 1 torr was 10ml/sec. This was sufficiently small to prevent any serious turbulance in the lamp and there was never any evidence to the contrary during its use.

Prior to using a magnesium fluoride window, a differentially pumped system separated the lamp from the predisperser system. This was very successful but had to be abandoned because the cathode to slit distance could not be kept below 60mm, the value required in order to be able to observe none of the discharge within about 2mm of the inside wall of the germanium cathode. Another problem encountered was the difficulty in preventing a discharge occurring at the metal intermediate slits. Masking and altering the anode geometry was never successful in suppressing this discharge.

The lamp was excited by the use of a constant current power supply. Stability of the current was about 1 part in 10^4.

5.2 Wavelength shift of the λ160.2nm line of GeII

A large number of measurements of the wavelength shift of the $5s\ ^2S_{1/2} - 4p\ ^2P_{1/2}$ transition of GeII at λ160.2nm for different source condition changes were made. A description of the most relevant results will now be given. The inverse linear dispersion in the focal plane at λ160.2nm using the 35th order is $0.012.10^{-3}$nm/step, or in wavenumbers $4.7.10^{-3}$cm^{-1}/step. All shift and width results will be given in step units (1 step ≡ 0.5μm).

Initially, a set of shift measurements using the full entrance slit length were made. Using neon, argon and helium as carrier gases, a set of shift versus rare gas pressure curves were obtained for both 50 and 100mA discharge currents and are shown in figure 23. These

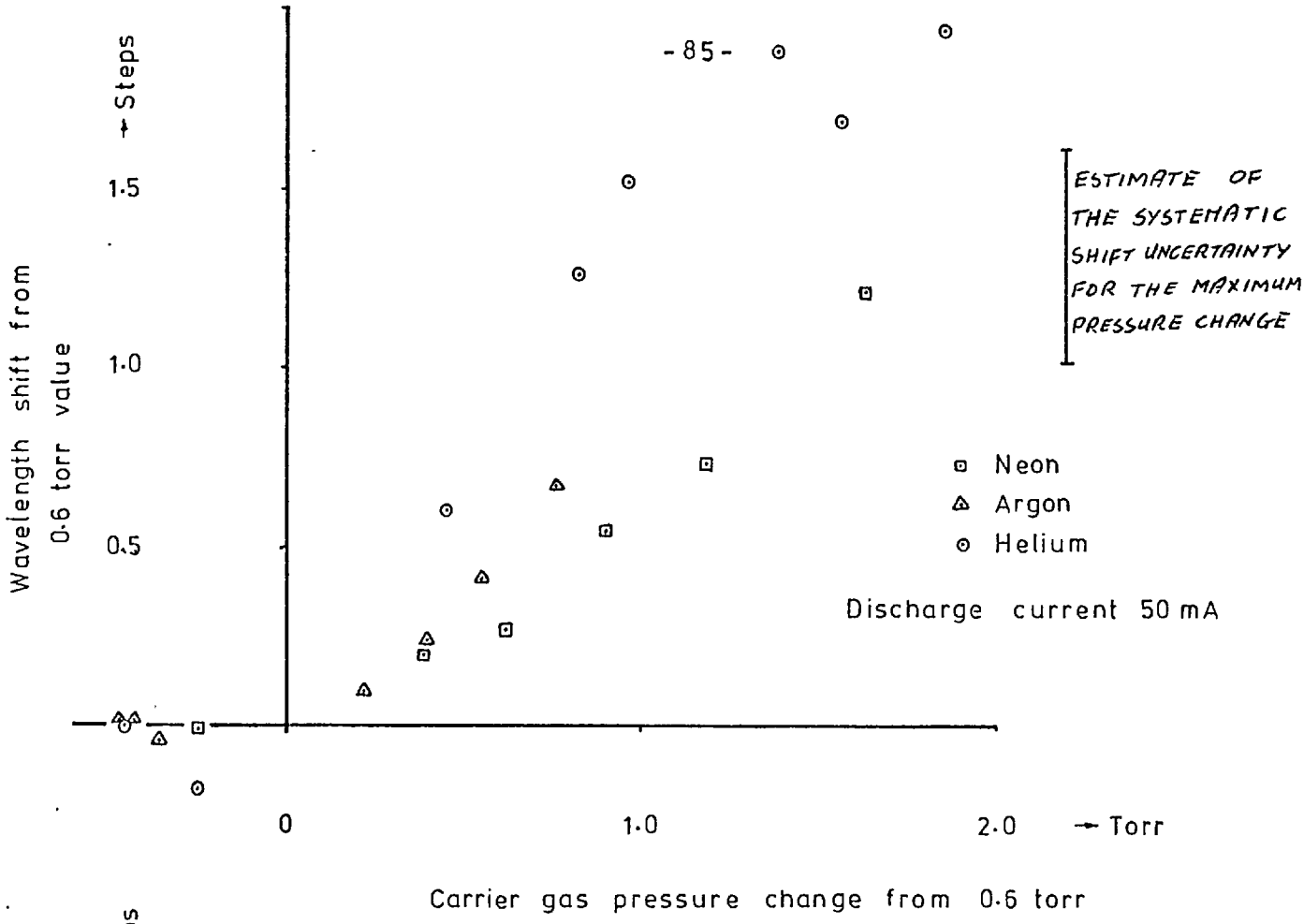

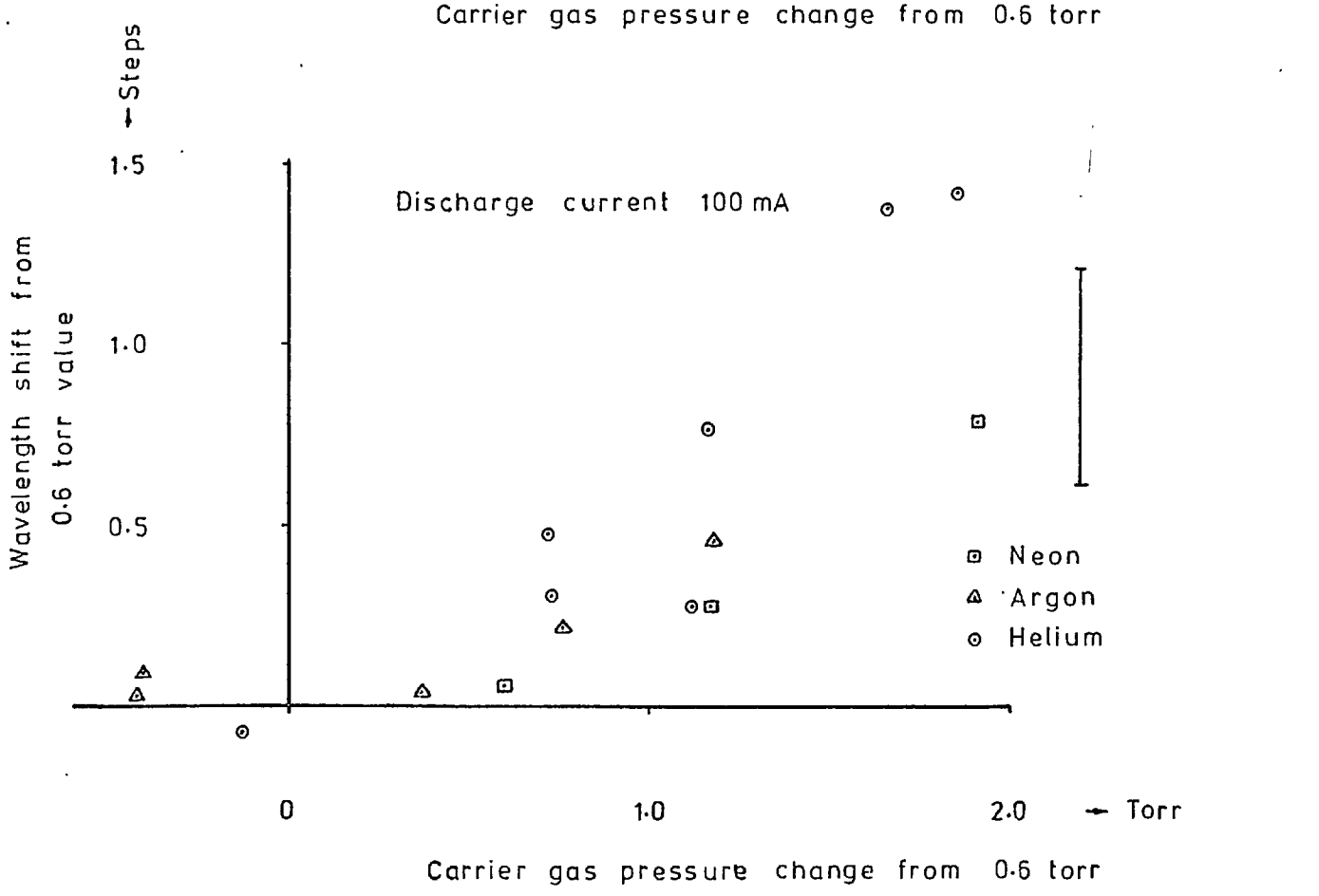

FIGURE 23. WAVELENGTH SHIFT VERSUS PRESSURE CURVES FOR λ160.2 nm Ge II LINE. INITIAL MEASUREMENTS.

indicate a red shift with increase in rare gas pressure. A wavelength shift versus discharge current determination for the three rare gases showed that at 0.6 torr the red shift was less than 0.2 ± 0.3 steps for a current change of 50 to 100mA. All the data corresponds to the use of 80% to 30% of the observed profile in the centre of gravity calculations. If 80-50 or 80-10 values are used there is little change in the results except that the general indication is that the shift increases as more of the line profile is used.

After these measurements, the predisperser entrance slit width was increased and its length limited to 2mm. The smaller signal increased the statistical uncertainty in a single shift determination. Up to 15 scans of the profile could be needed to obtain a combined random and systematic uncertainty corresponding to ± 0.4 steps for the shift corresponding to maximum pressure. Accumulation of data was a very slow process and a single point of a shift curve could take as long as 1-2 hours.

The results shown in figures 24, 25, 26 refer to the observed pressure shifts for neon, argon and helium respectively at both 50 and 100mA. Helium is still producing the largest shift. There is very little change in pressure shift with current. However, change in current from 50 to 100mA at a helium pressure of 0.6 torr produced a blue shift of 0.65 ± 0.3 steps whilst neon and argon produced a shift smaller than 0.2 ± 0.3 steps.

Prior to these measurements, but after the predisperser entrance slit length had been reduced, a neon carrier gas pressure versus wavelength shift curve had yielded a shift shown in figure 27. Comparison with the later curve shown in figure 24 shows a larger red shift. Before using neon as carrier gas, helium had been used in the lamp for about 1200 mins. running time. The following evidence supports the case that the larger shift is a result of helium present in the

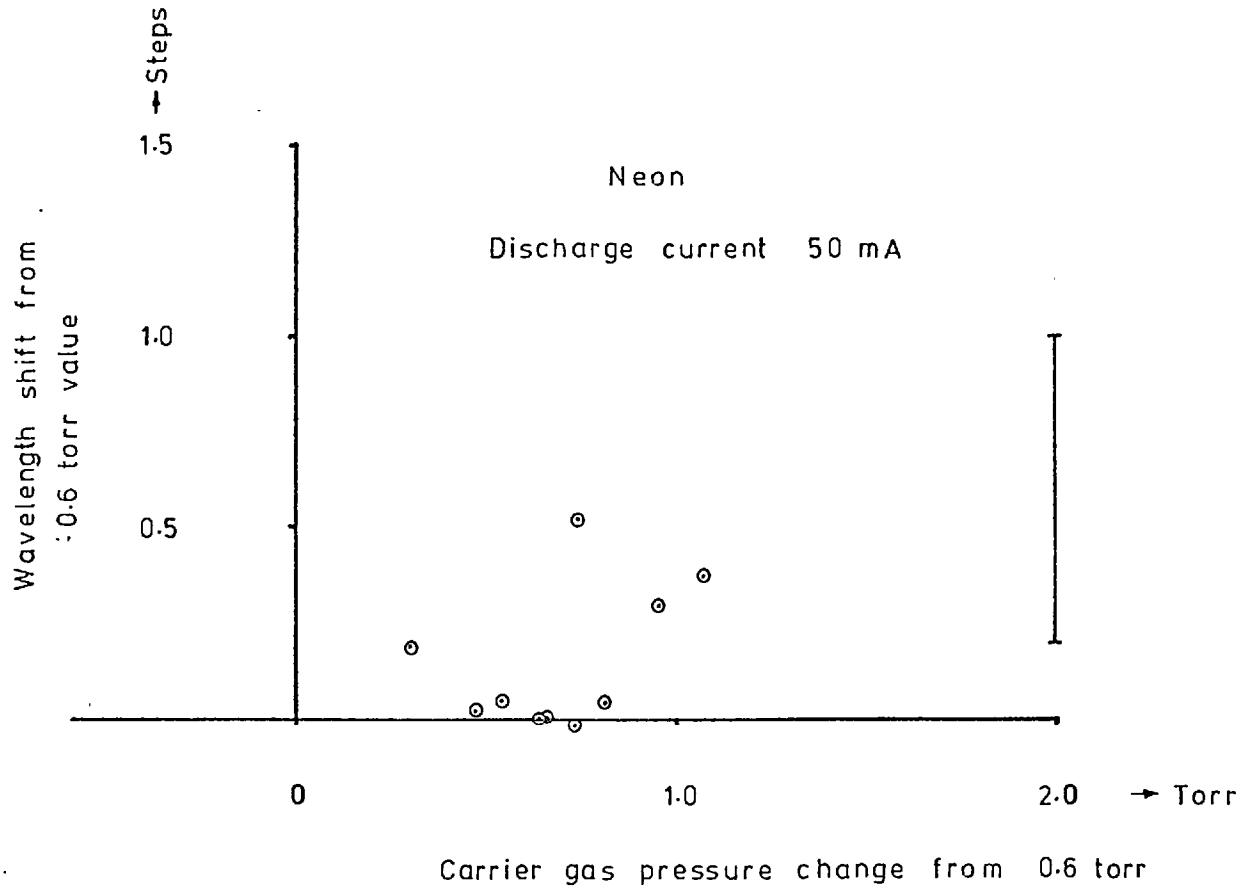

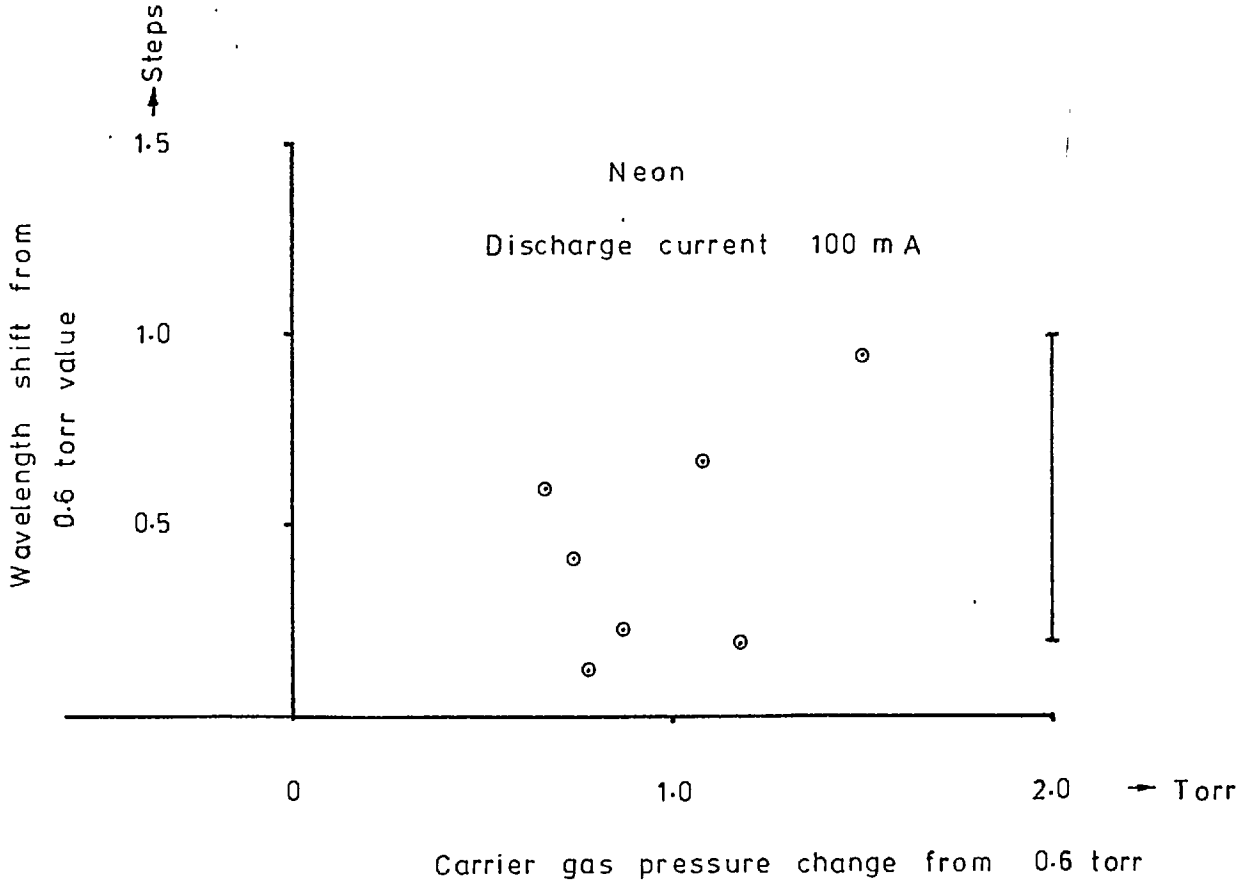

FIGURE 24. WAVELENGTH SHIFT VERSUS NEON PRESSURE FOR THE λ160·2 nm LINE

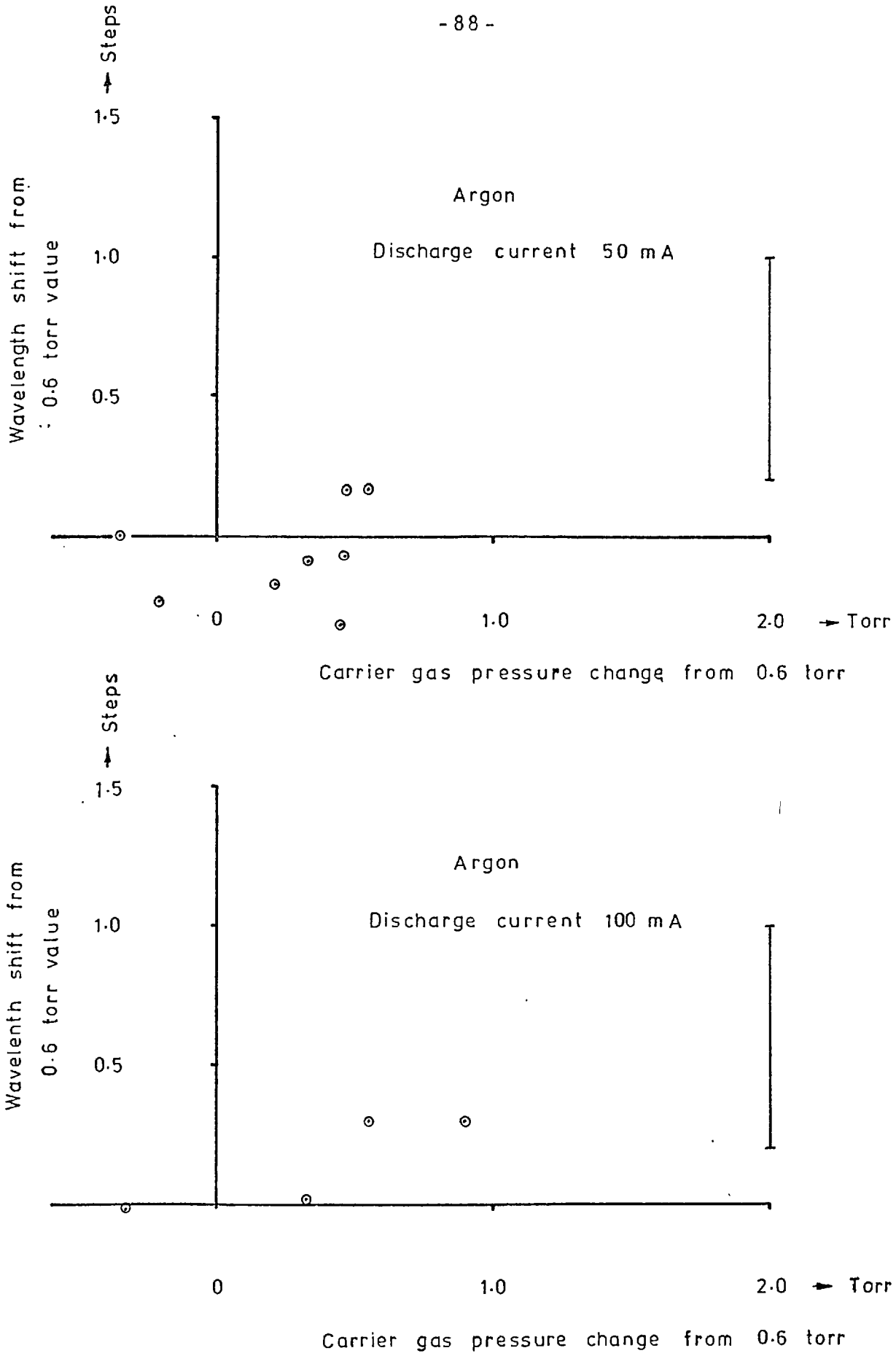

FIGURE 25. WAVELENGTH SHIFT VERSUS ARGON PRESSURE FOR THE λ160·2 nm LINE

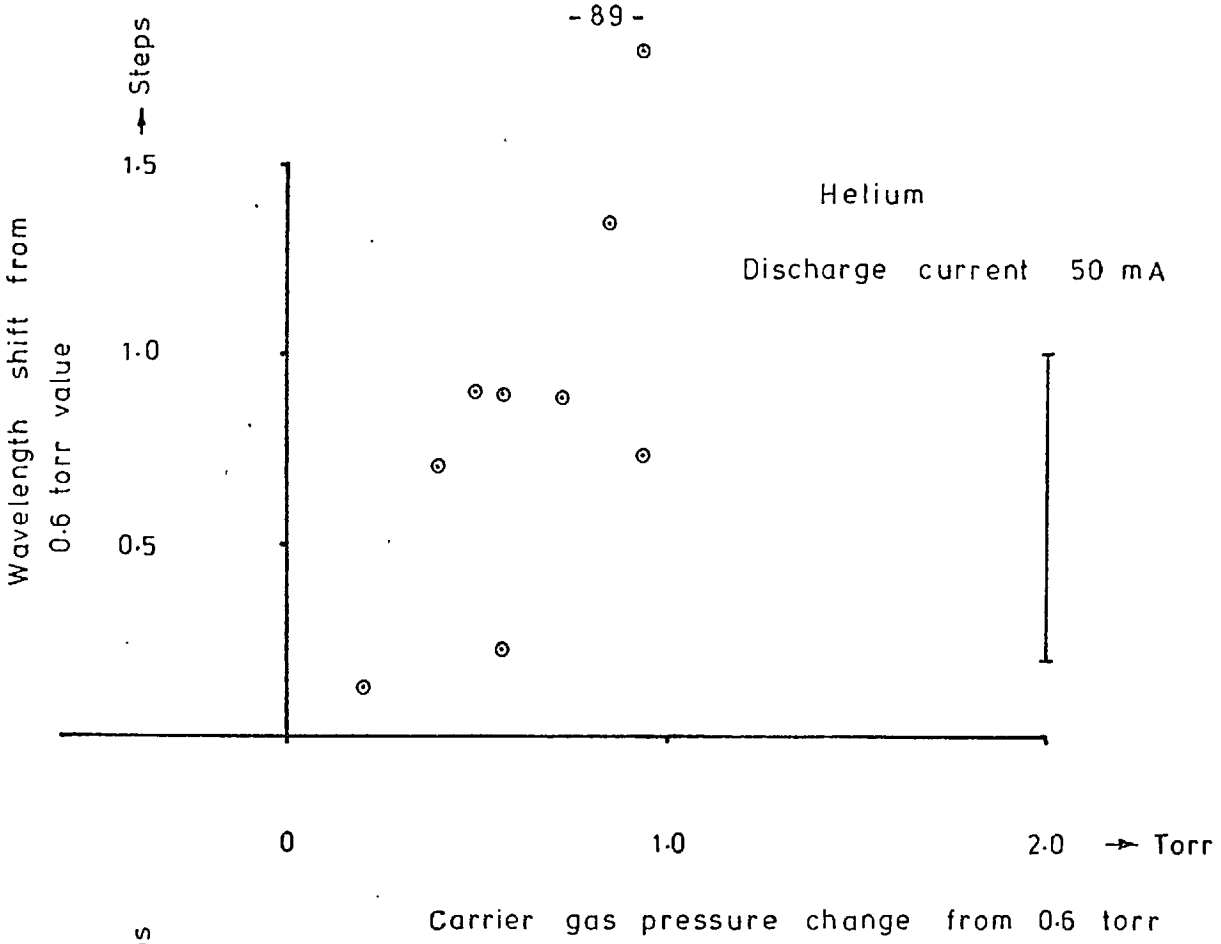

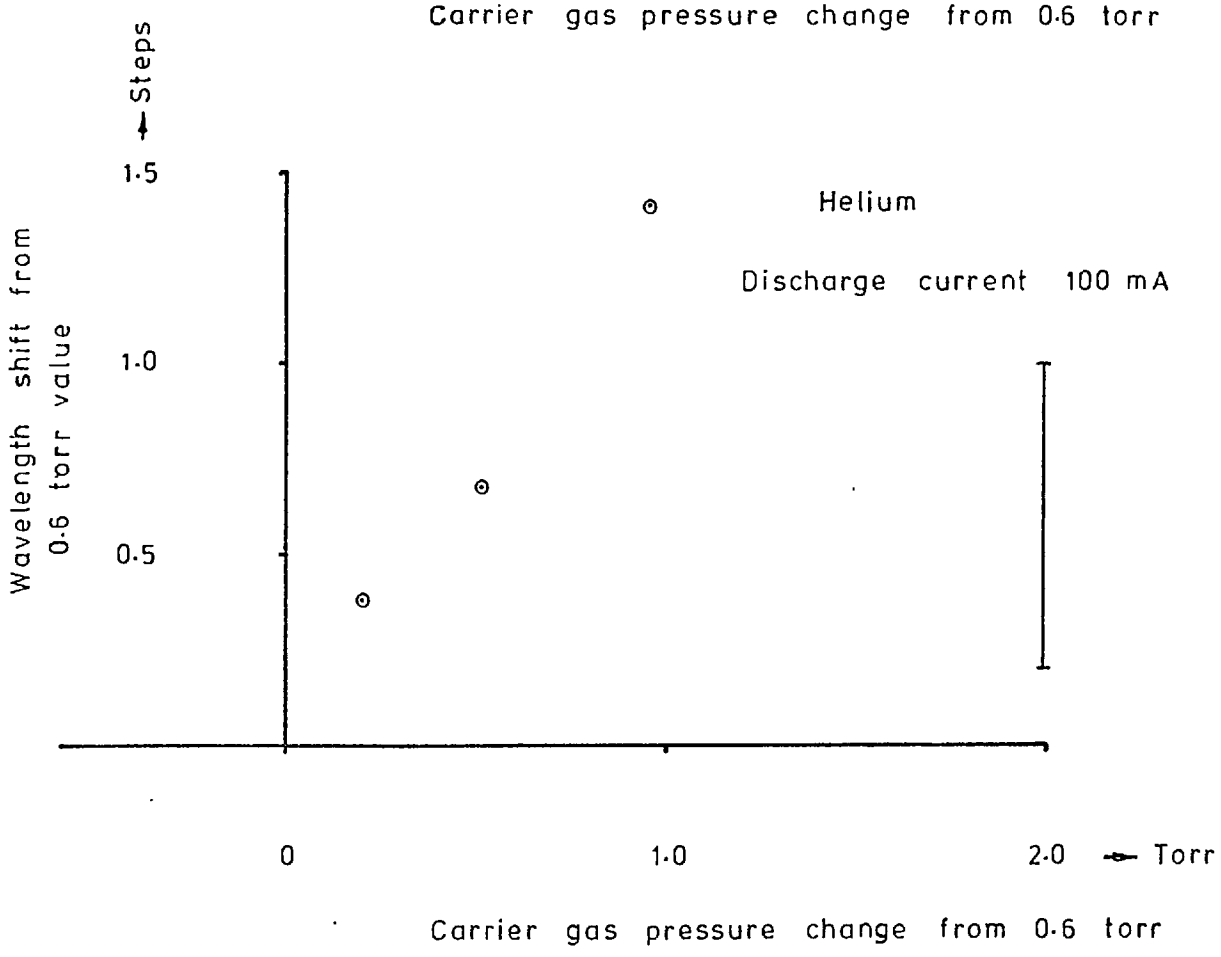

FIGURE 26. WAVELENGTH SHIFT VERSUS HELIUM PRESSURE FOR THE λ160·2 nm LINE

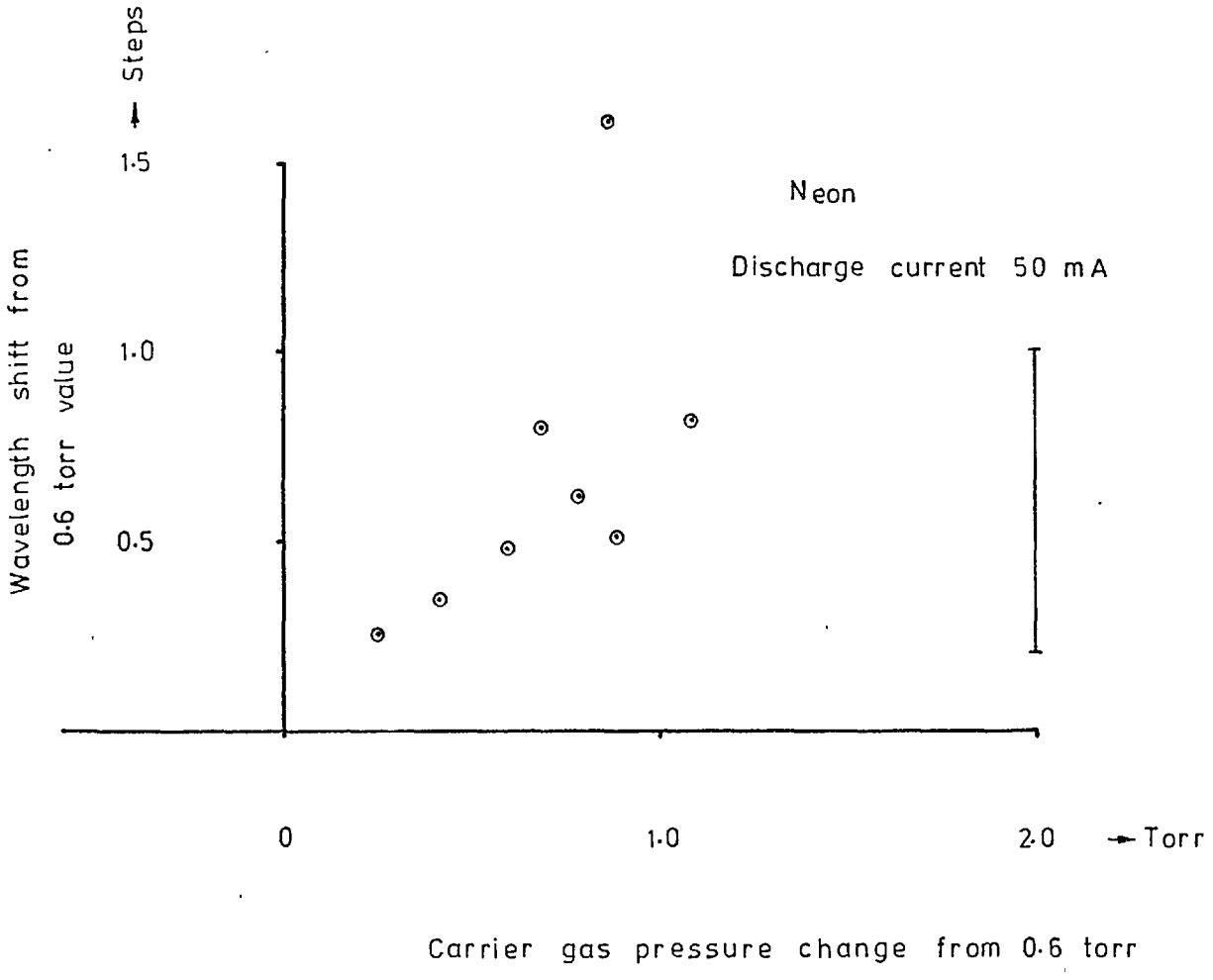

FIGURE 27. WAVELENGTH SHIFT VERSUS NEON PRESSURE FOR THE λ160·2 nm LINE. THIS EARLY MEASUREMENT INDICATES A LARGER SHIFT THAN THAT SHOWN IN FIGURE 24, PROBABLY A RESULT OF HELIUM PRESENT IN THE LAMP

discharge lamp:-

Helium always pumped away slowly from the lamp after a set of measurements had been made. This appeared to be a result of absorption of helium in the solid germanium cathode.

Observation of the HeII line at λ164nm, whilst the lamp was run with neon carrier gas, showed an intensity between 10 and 20% of its value when helium was used. The intensity increased with decrease in neon pressure.

A set of measurements were undertaken which involved obtaining shifts with pressure for the three rare gases in the following order:-

1. Neon,
2. Argon,
3. Neon,
4. Helium,
5. Neon.

Sets 1. to 4. produced results consistent with those shown in figures 24-26 but set 5. produced a shift whose initial value was 0.5 steps at 0.72 torr increase in pressure i.e. consistent with the results shown in figure 27. After pumping the lamp for a day, the next measurement showed a shift consistent with figure 24 and following runs also showed very small shifts.

One cause of the wavelength shifts of the form observed in figures 23-27 is that of electric fields causing Doppler shifts, as will be discussed later. Change of the anode to cathode separation could possibly change the field distribution. With this in mind, the anode to cathode separation was changed from the usual 4-5mm to 8mm.

Figure 28 shows the results of a neon pressure versus wavelength shift curve for the larger separation. There is no evidence for any change in the shift.

The solid germanium cathode was replaced by an aluminium one with germanium spread around the inside of the 10mm bore using a slurry of germanium powder and distilled water. Wavelength shifts with neon are shown in Figure 29, indicating a blue shift of considerable magnitude which appears to decrease on increase in discharge current from 50 to 100mA.

There was a considerable difference in the spatial characteristics of the discharge between the solid germanium cathode and the germanium lined aluminium cathode. In the former, the discharge extended outside the cathode towards the anode, i.e. appeared as a positive column, and contracted into the hollow cathode on increase in pressure. This was especially pronounced using helium as carrier gas. On increase in current this effect was still present. For the aluminium cathode, the discharge extended through the aluminium anode and at low pressures appeared to reach the window; as the pressure increased there was no evidence of contraction into the cathode although there was a reduction of discharge beyond the anode.

During the course of the wavelength shift measurements, the reproducibility of the measurements appeared to be best using helium and argon as carrier gases. This may be because the presence of helium causes spurious shifts. Argon, with its higher sputtering rate, may not be as dependent on surface absorption of helium because it is removed quickly. In the case of neon, removal of helium would take longer. Helium shift measurements would not of course be affected. The overall uncertainty of the shift measurements is about $\pm$ 0.4 steps at the highest pressure. This takes into account the possibility of systematic shifts as already described.

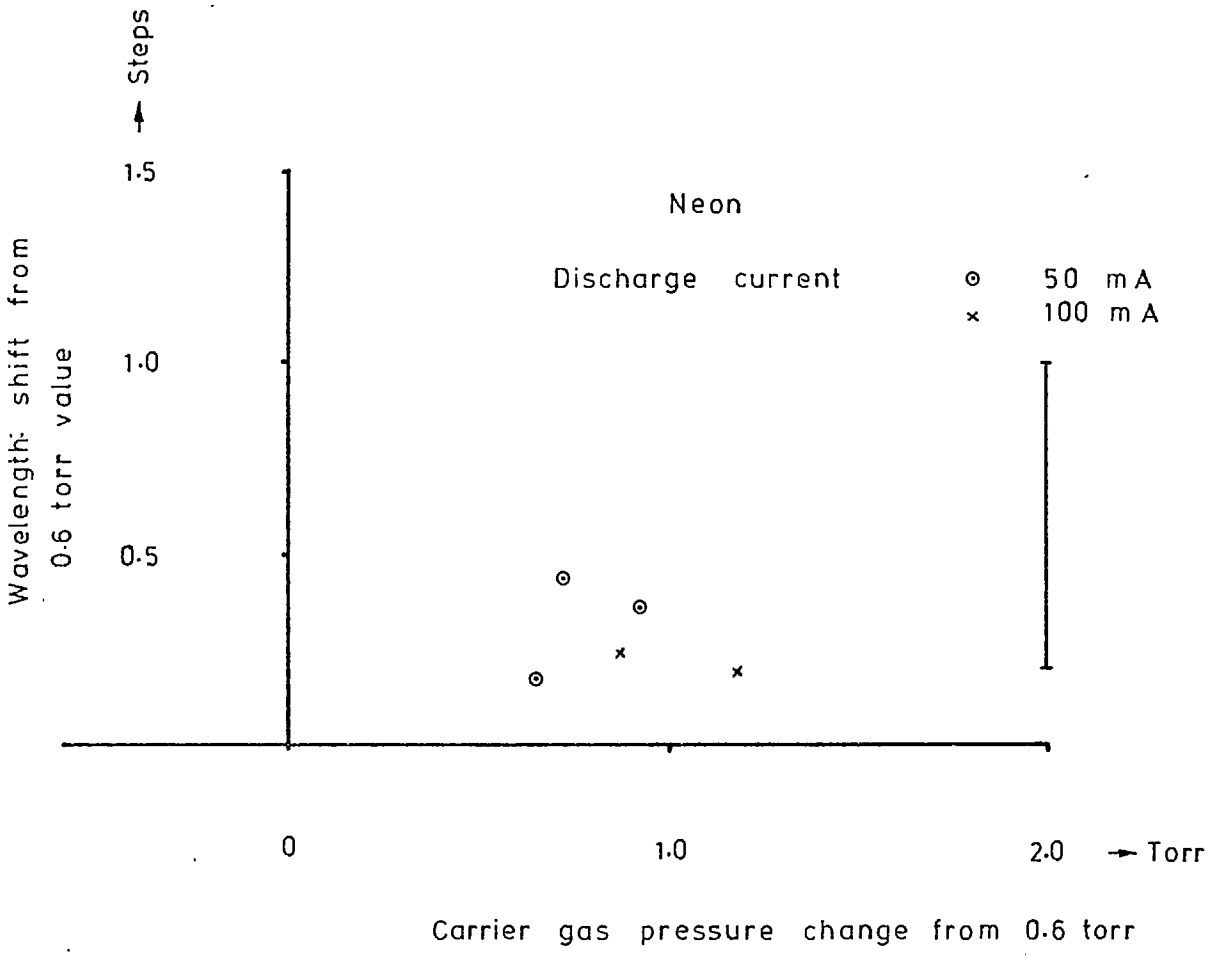

FIGURE 28. WAVELENGTH SHIFT VERSUS NEON PRESSURE FOR THE λ160·2 nm LINE, WITH AN ANODE-CATHODE SEPARATION INCREASED TO 8 mm

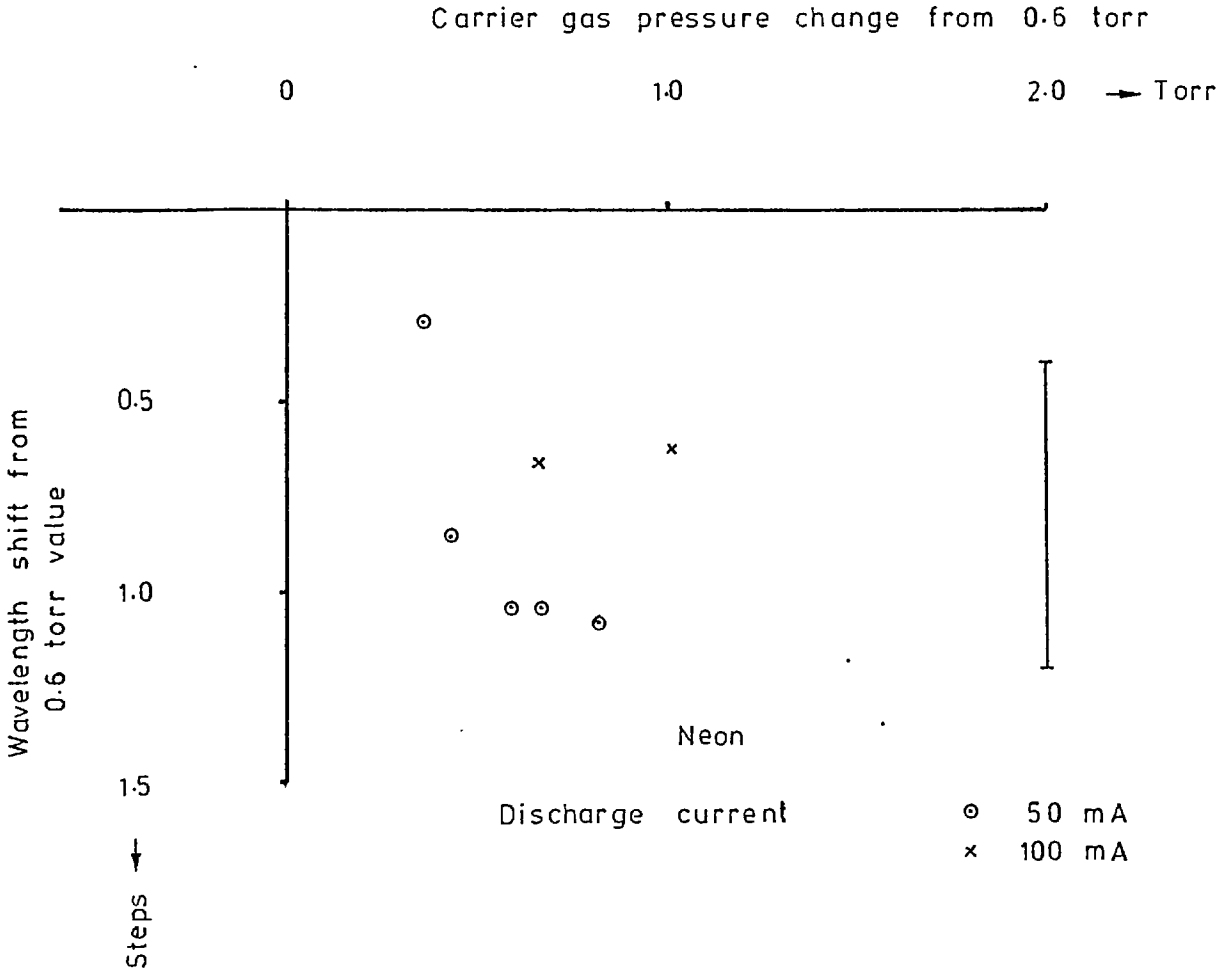

FIGURE 29. WAVELENGTH SHIFT VERSUS NEON PRESSURE FOR THE λ160·2 nm LINE, FOR AN ALUMINIUM CATHODE LINED WITH GERMANIUM

5.3 Overall width of the λ160.2nm line

The full width at half maximum intensity of the observed profiles was measured from the x-y recorder traces. Figure 30 shows the widths plotted against rare gas pressure for neon, argon and helium at 50 and 100mA discharge currents. Figure 31 shows the width versus discharge current for neon at 0.6 torr. These results indicate a significant change in width with discharge conditions and it is evident that under no condition is there no broadening of the observed profile. As will be discussed later self-absorption is an important broadening mechanism.

Width measurements were taken over a considerable period of time, nearly 6 months. Hence, the scatter of the results is an indication of the reproducibility of the instrumental profile of the spectrometer.

5.4 Intensity-pressure characteristics

The peak intensity of the observed profile was monitored and its change with rare gas pressure recorded for 25, 50, 75 and 100mA discharge currents. A broad maximum is observed as shown in figures 32, 33 and 34 for the three rare gases. Detailed explanation of these curves is not possible, but their general form can be explained as discussed in section 6.1. A family of log (Intensity) versus log (current) curves for different pressures shows a predominant slope of about 2 in the case of helium and neon except at low pressure where it decreases with increase in current, indicating the presence of self-absorption. Argon, however, shows a similar effect at low pressure but a slope as high as 5 occurs at high pressure. No satisfactory explanation is apparent, although collision-exchange processes could be responsible.

Using the aluminium hollow cathode, the pressure-intensity curve

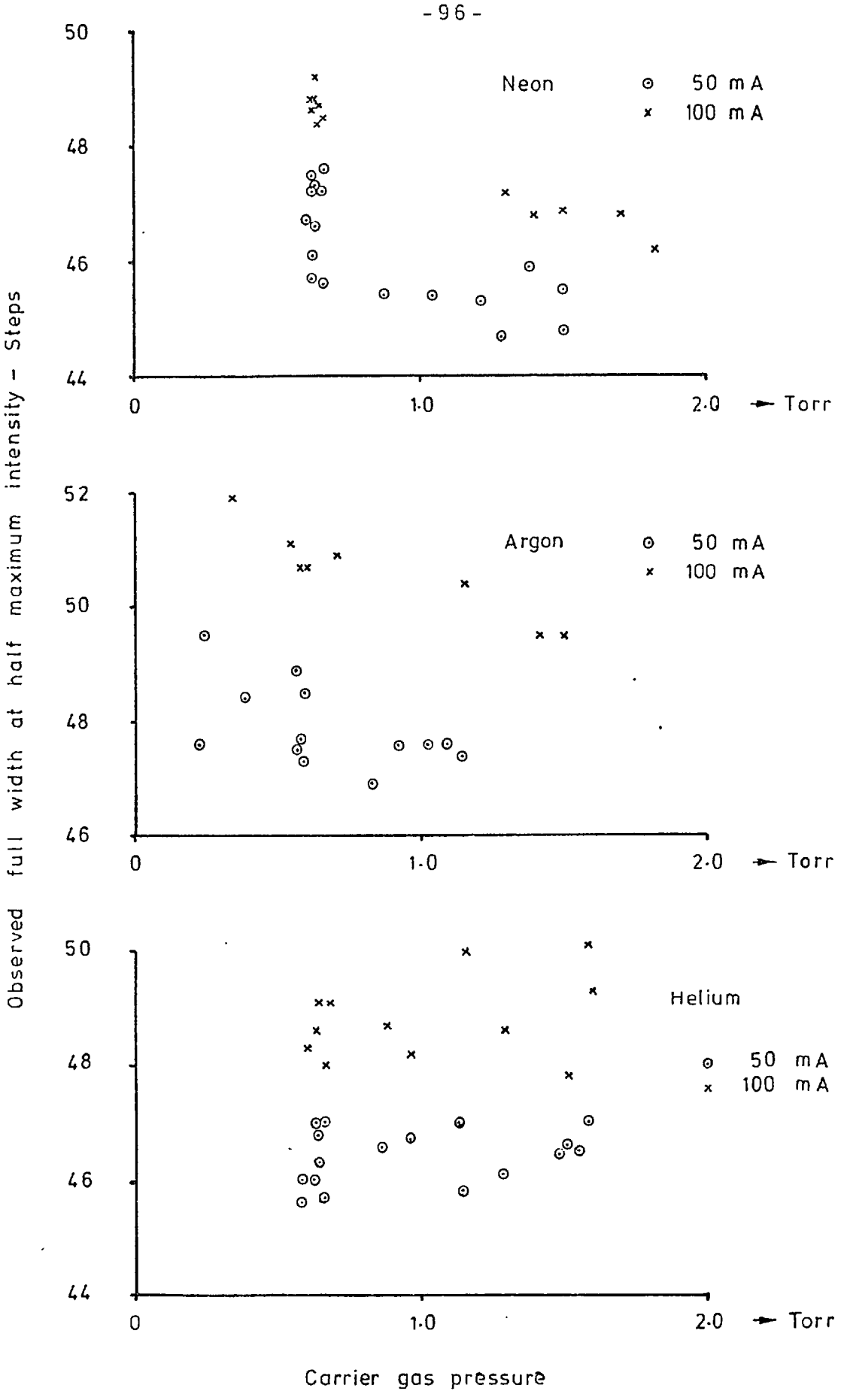

FIGURE 30. OVERALL WIDTH OF THE λ160·2 nm LINE AS A FUNCTION OF CARRIER GAS PRESSURE

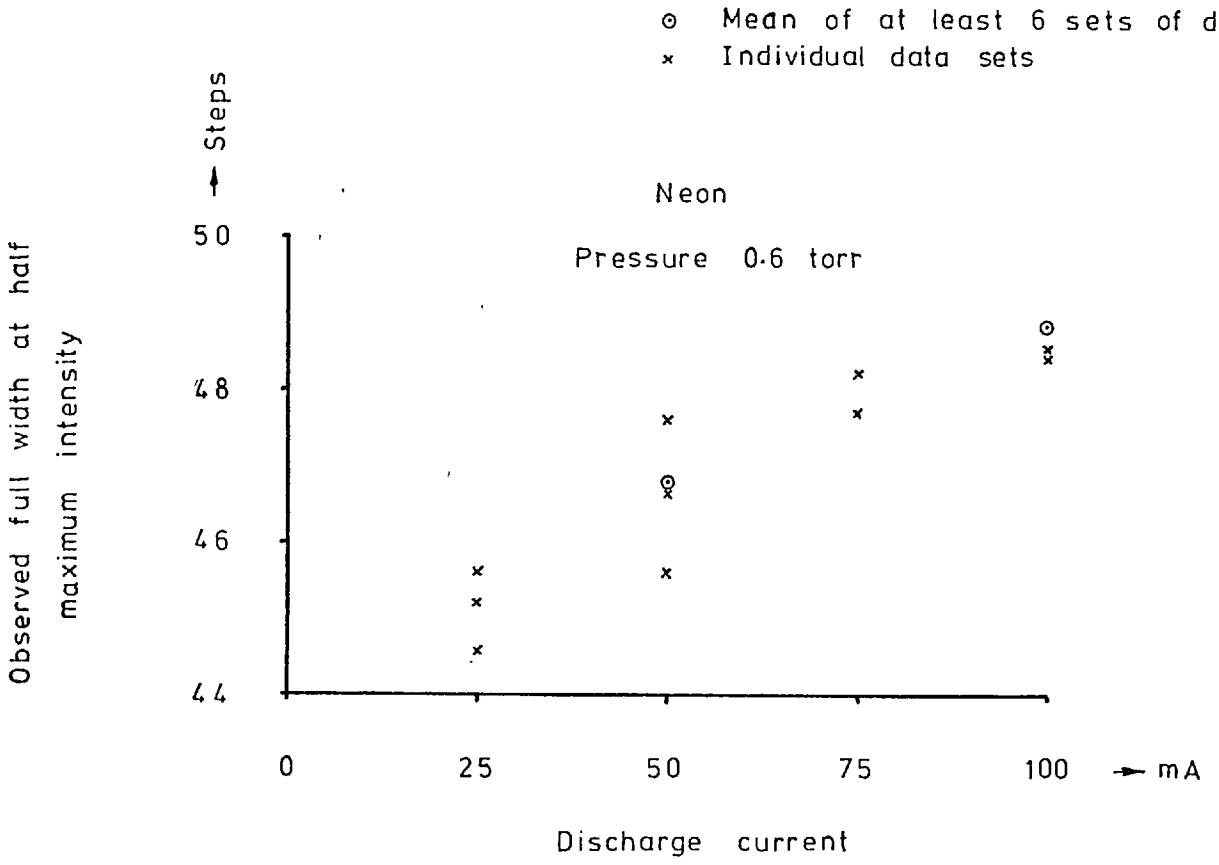

FIGURE 31. OVERALL WIDTH OF THE λ160·2 nm LINE AS A FUNCTION OF DISCHARGE CURRENT

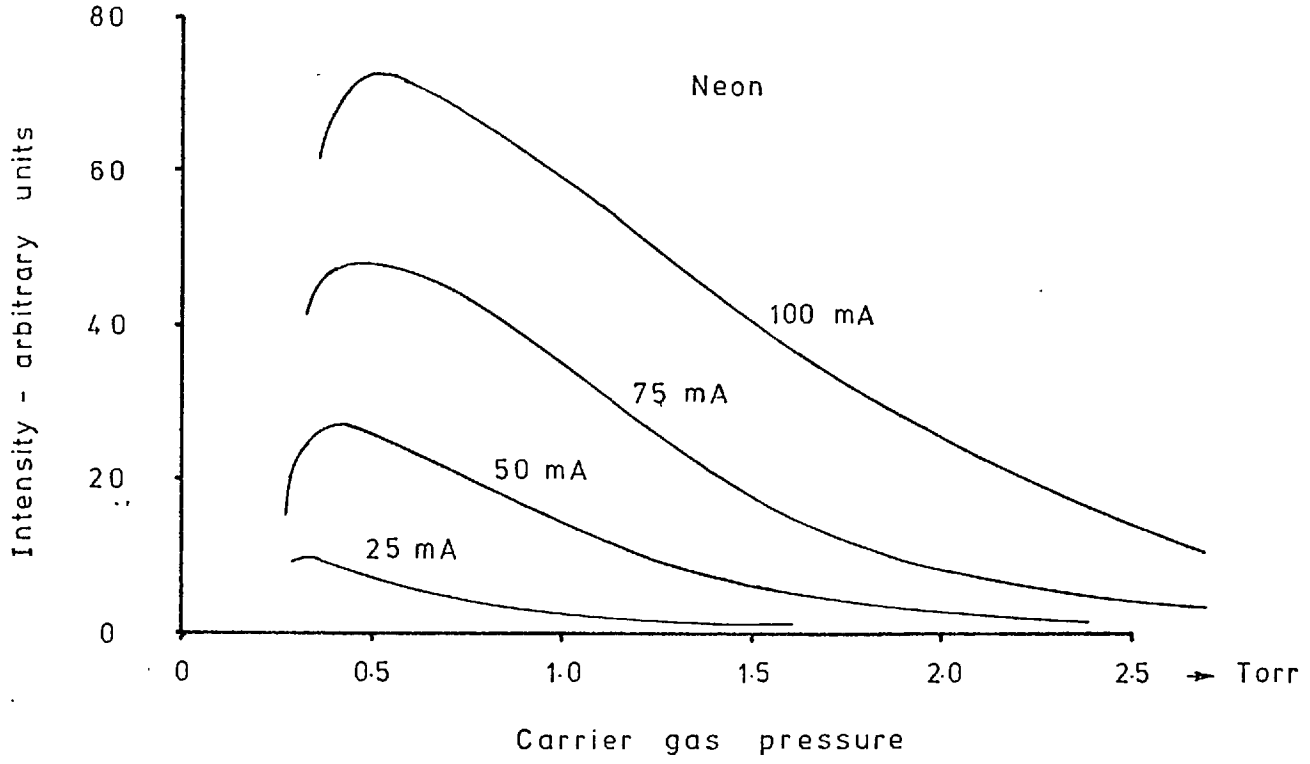

FIGURE 32. INTENSITY VERSUS NEON PRESSURE FOR THE λ160·2 nm LINE

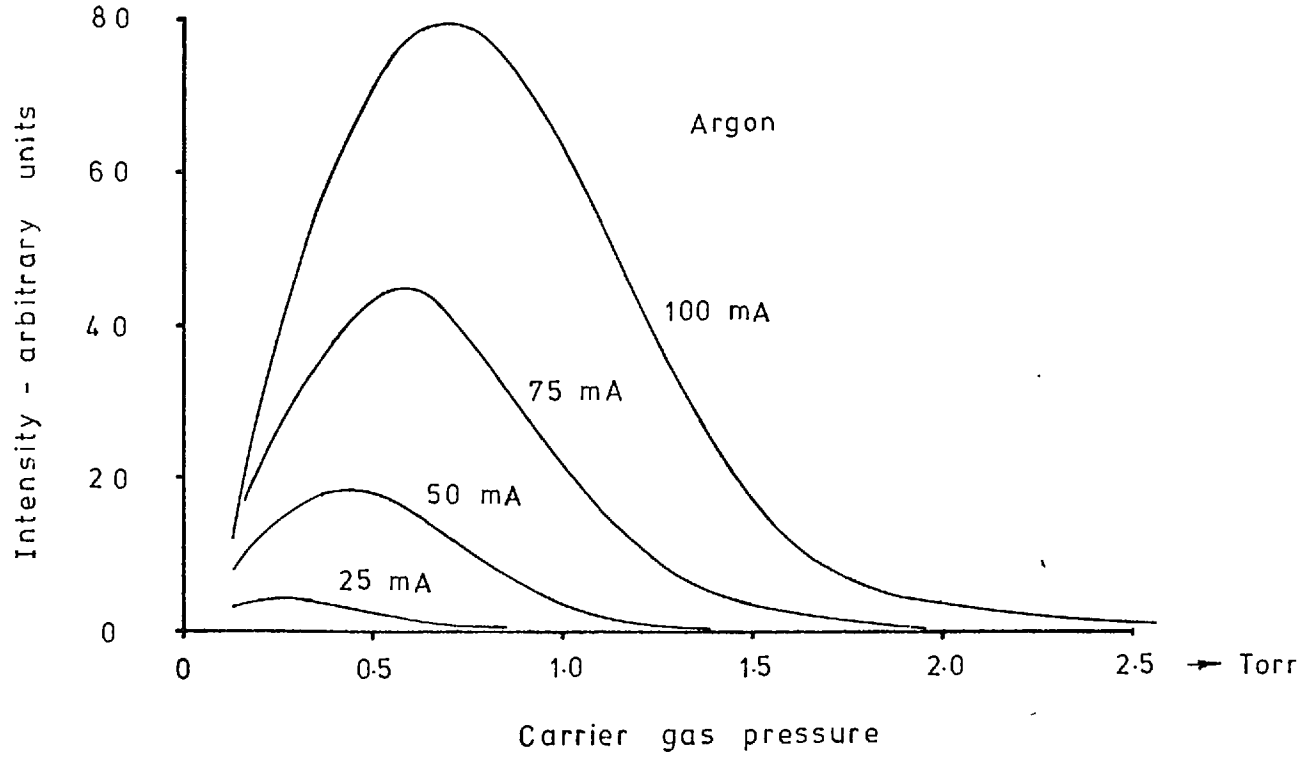

FIGURE 33. INTENSITY VERSUS ARGON PRESSURE FOR THE λ160·2 nm LINE

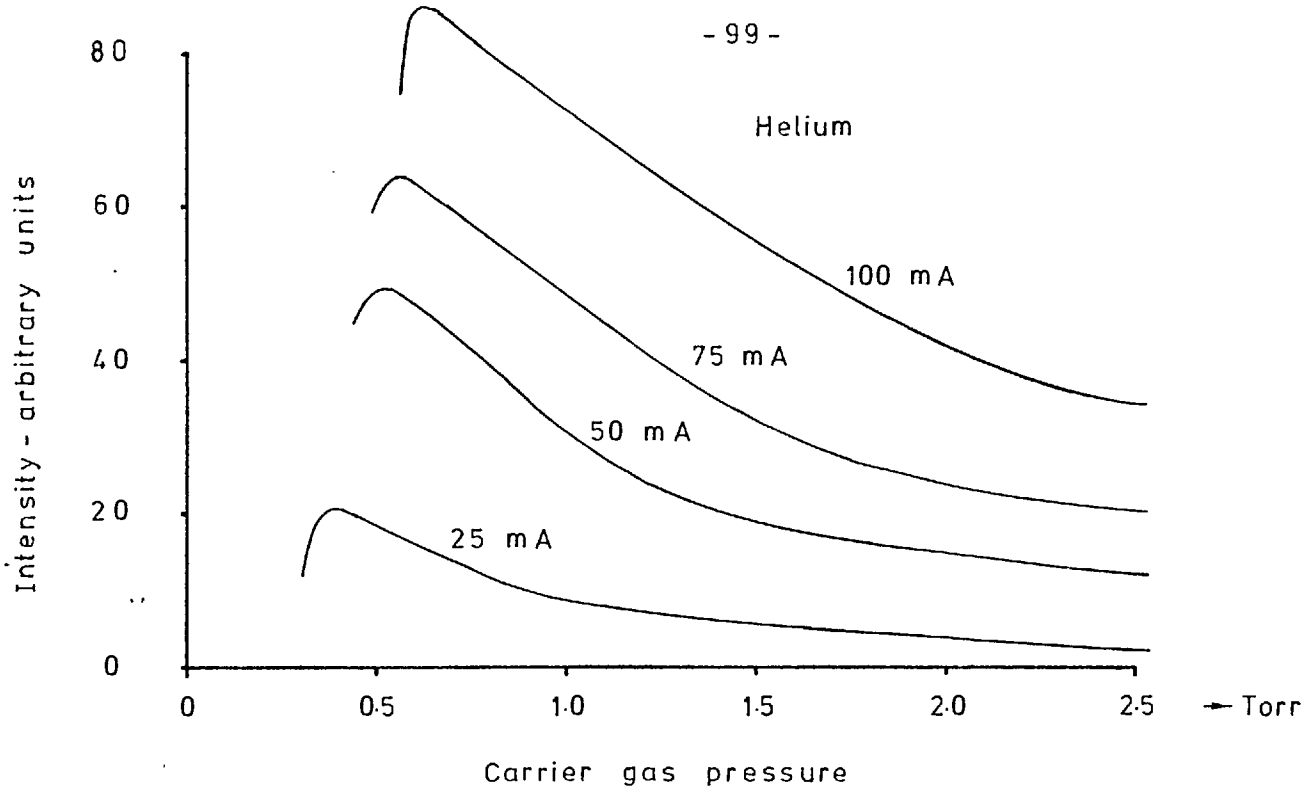

FIGURE 34. INTENSITY VERSUS HELIUM PRESSURE FOR THE λ160·2 nm LINE

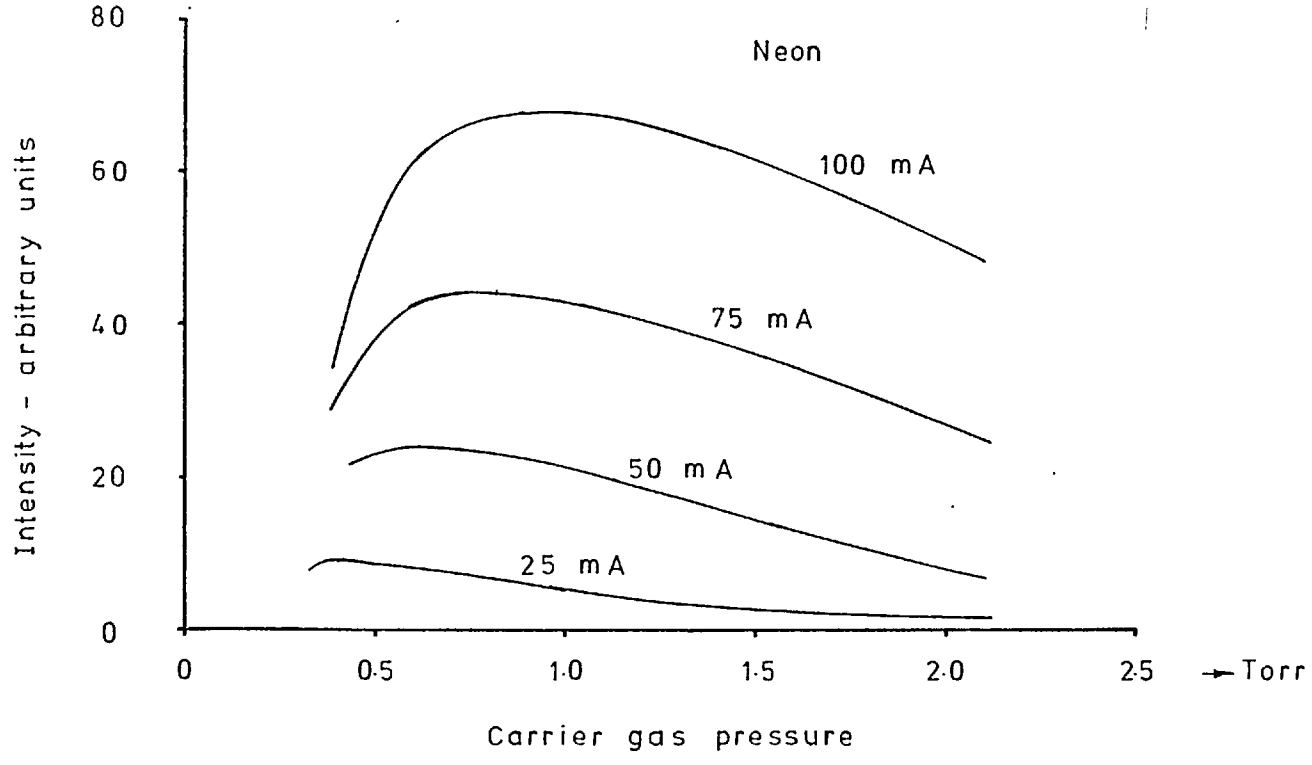

FIGURE 35. INTENSITY VERSUS NEON PRESSURE FOR THE λ160·2 nm LINE, FOR AN ALUMINIUM CATHODE LINED WITH GERMANIUM

with neon as a carrier gas is shown in figure 35 and appears to be broader than the solid germanium cathode curve shown in figure 32. The absolute peak intensity is about 50% of that shown in figure 32.

5.5 Overall lamp voltage-pressure characteristics

Figure 36 shows the overall lamp voltage versus pressure for the three rare gases at 50 and 100mA discharge current. Although these curves reflect the cathode fall, it is evident that the lamp voltage changes most rapidly in the case of helium over the working pressure range 0.6 to 2.0 torr.

Using neon and argon, the overall lamp voltage would decrease by about 10-20 volts during the first hour that the lamp was run and then settle down to a stable value. In the case of helium, the change could be as high as 40 volts during a similar period. Despite these changes there was no evidence of any correlation with change in wavelength shift and there was little evidence of intensity change. Again this is probably because the voltage change occurs at the cathode and the excitation mechanisms in the discharge occur in the negative glow region which is not strongly influenced by cathode changes. Impurity on the cathode is the probable cause of the voltage change, this would alter the surface potentials.

5.6 Observations on the λ164.9nm and λ157.7nm lines

(a) λ164.9nm line.

The ground state of GeII has the configuration $4p\ ^2P_{1/2,3/2}$. Transitions from the $5s\ ^2S_{1/2}$ produce a doublet of which the λ160.2nm, already investigated, is one member. The other member is the λ164.9nm, corresponding to the $5s\ ^2S_{1/2} - 4p\ ^2P_{3/2}$ transition, which is twice as intense as the λ160.2nm line. Some wavelength shift measurements were made

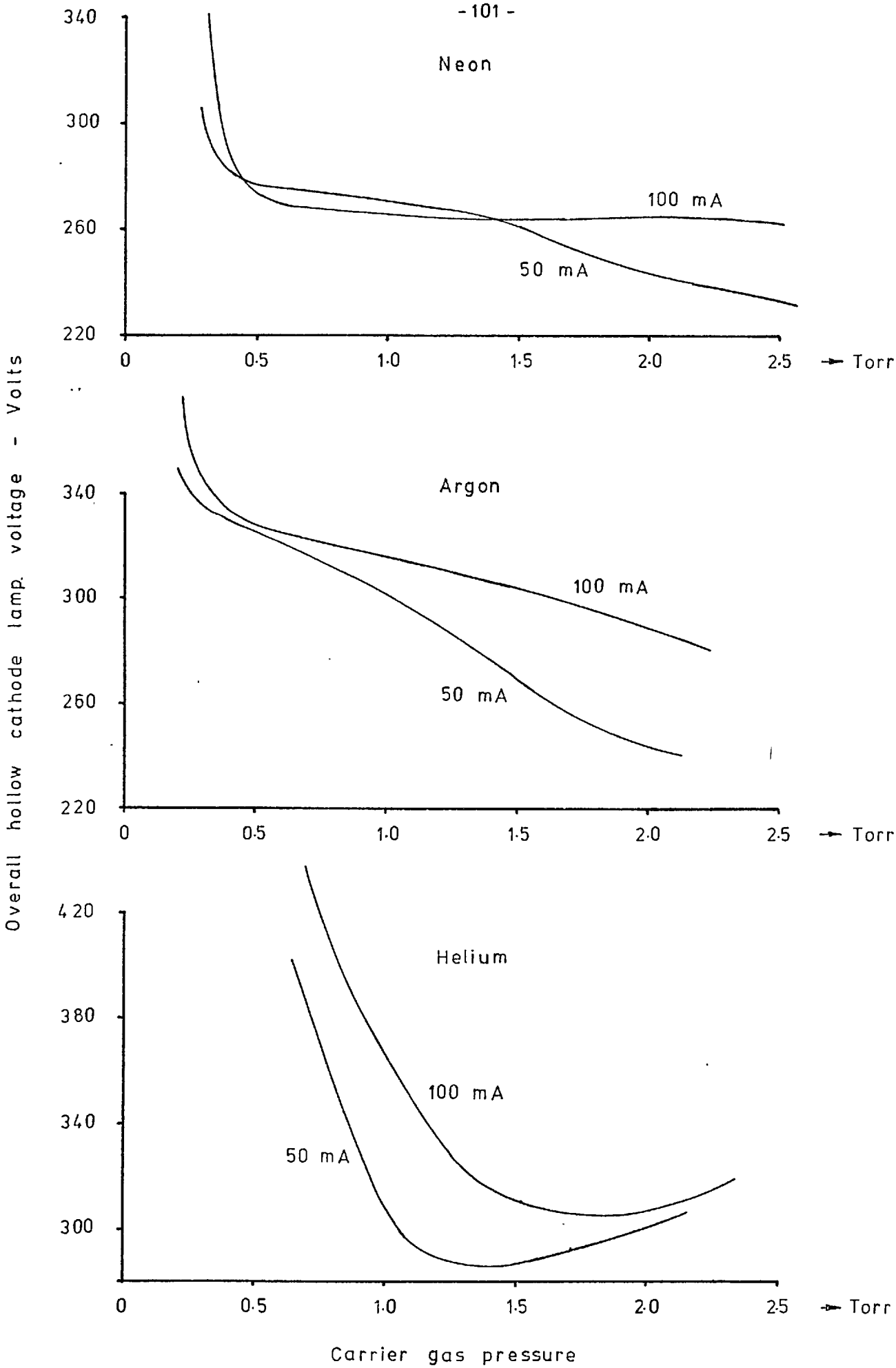

FIGURE 36. HOLLOW CATHODE LAMP ELECTRICAL CHARACTERISTICS

on the λ164.9nm component using neon as a carrier gas. Using the 34th order, the dispersion is $0.0125.10^{-3}$nm/step, or in wavenumbers $4.60.10^{-3}cm^{-1}$/step. Figure 37 shows the results and indicates that this component may be showing a rather smaller red shift than the λ160.2nm results given in figure 24 but there is little significant difference.

(b) λ157.7nm line.

Another strong multiplet arises from the transition $4s4p^2\ ^2D_{5/2,3/2} - 4s^2 4p\ ^2P_{3/2,1/2}$. The most intense component of the triplet occurs at λ157.7nm. Here, the dispersion using the 36th order is $0.0111.10^{-3}$nm/step, or $4.46.10^{-3}cm^{-1}$/step. Again, using neon as carrier gas, a wavelength shift versus pressure plot was obtained for 50 and 100mA discharge currents. Figure 38 shows the results of shift measurements and figure 39 the width variation with pressure. The latter is an indication that self-absorption is very strong in this line. There is an indication that the slope of the curve is falling on increase in pressure but no asymptotic value of $\frac{P}{\lambda}$ width (giving the instrumental width) can be inferred.

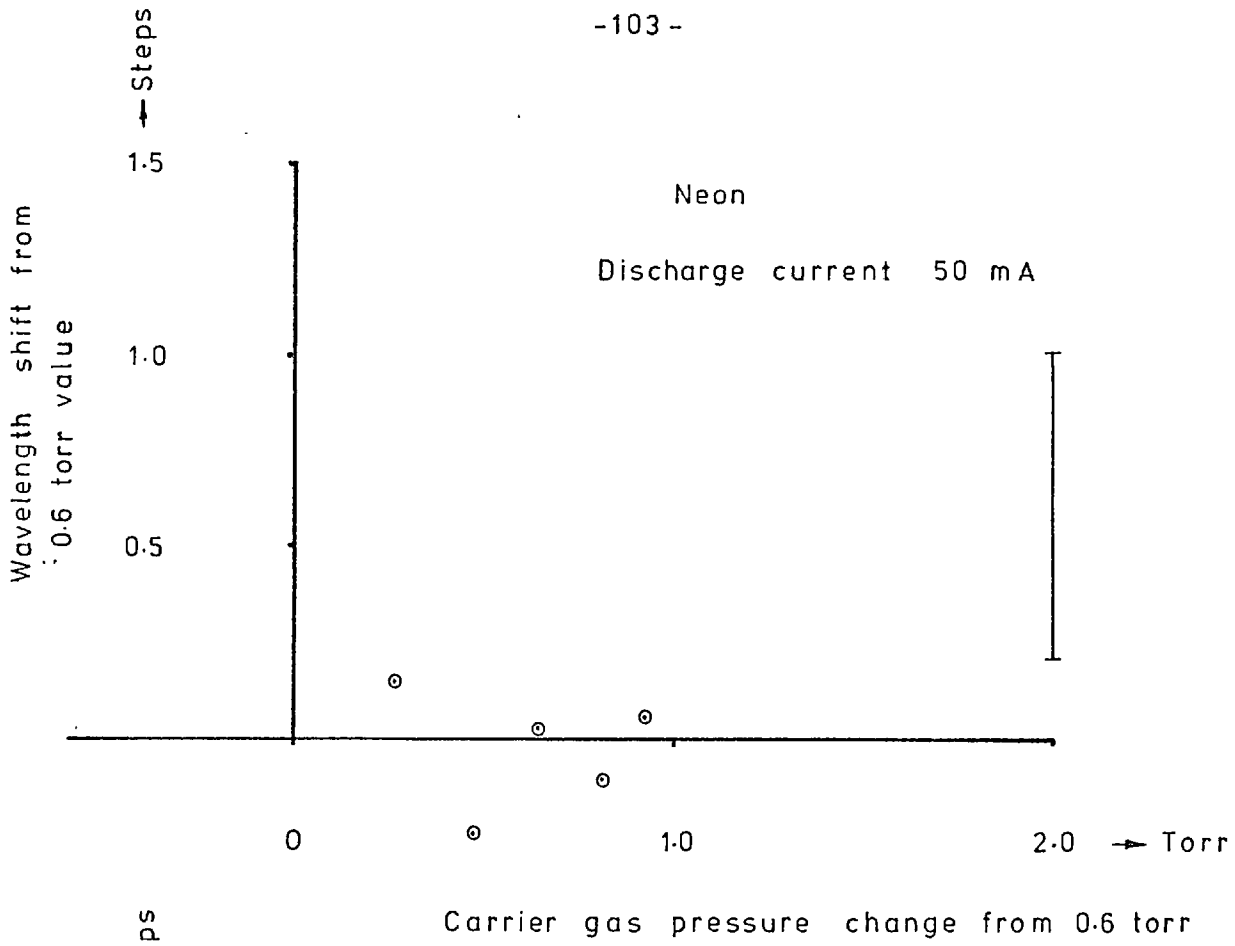

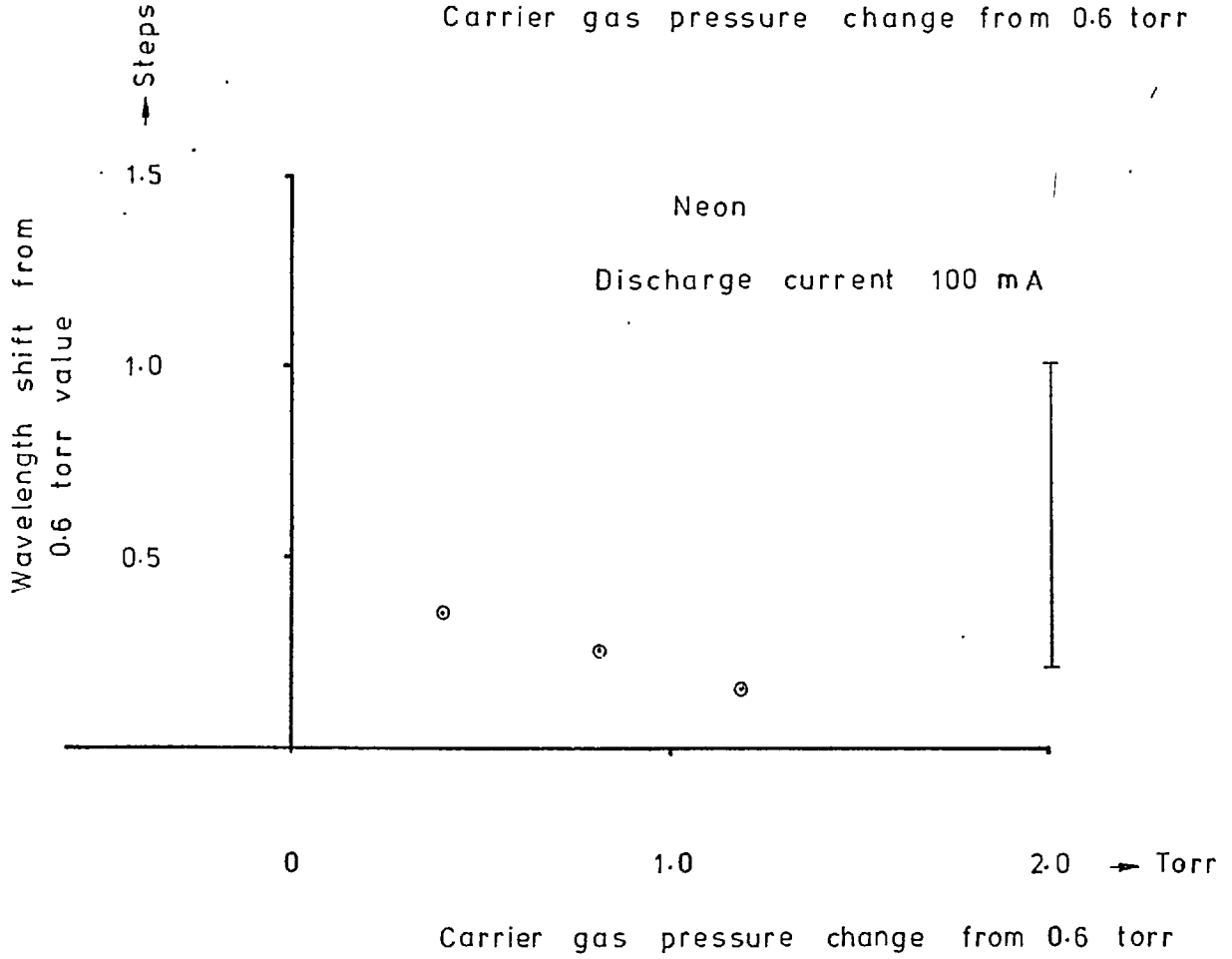

FIGURE 37. WAVELENGTH SHIFT VERSUS NEON PRESSURE FOR THE λ164.9 nm LINE

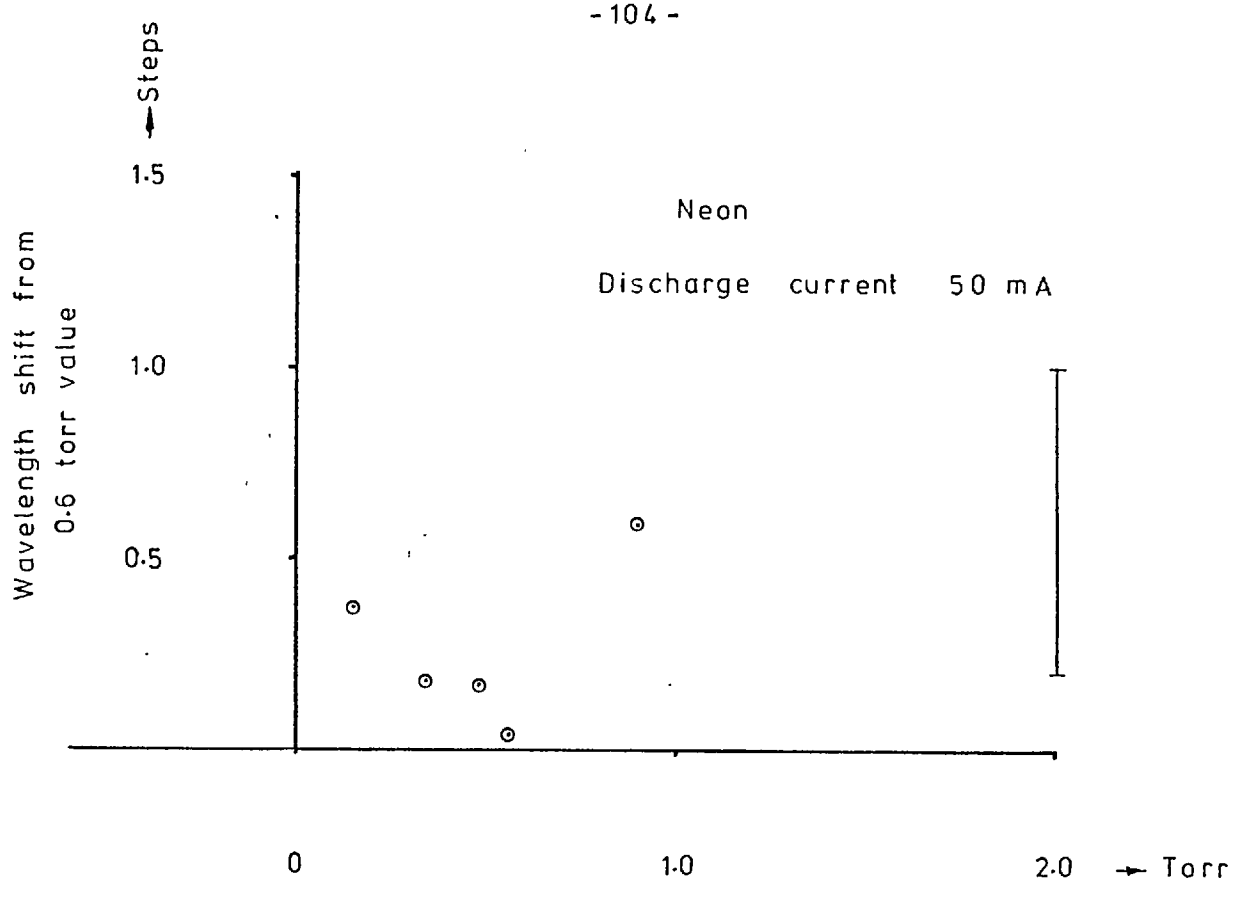

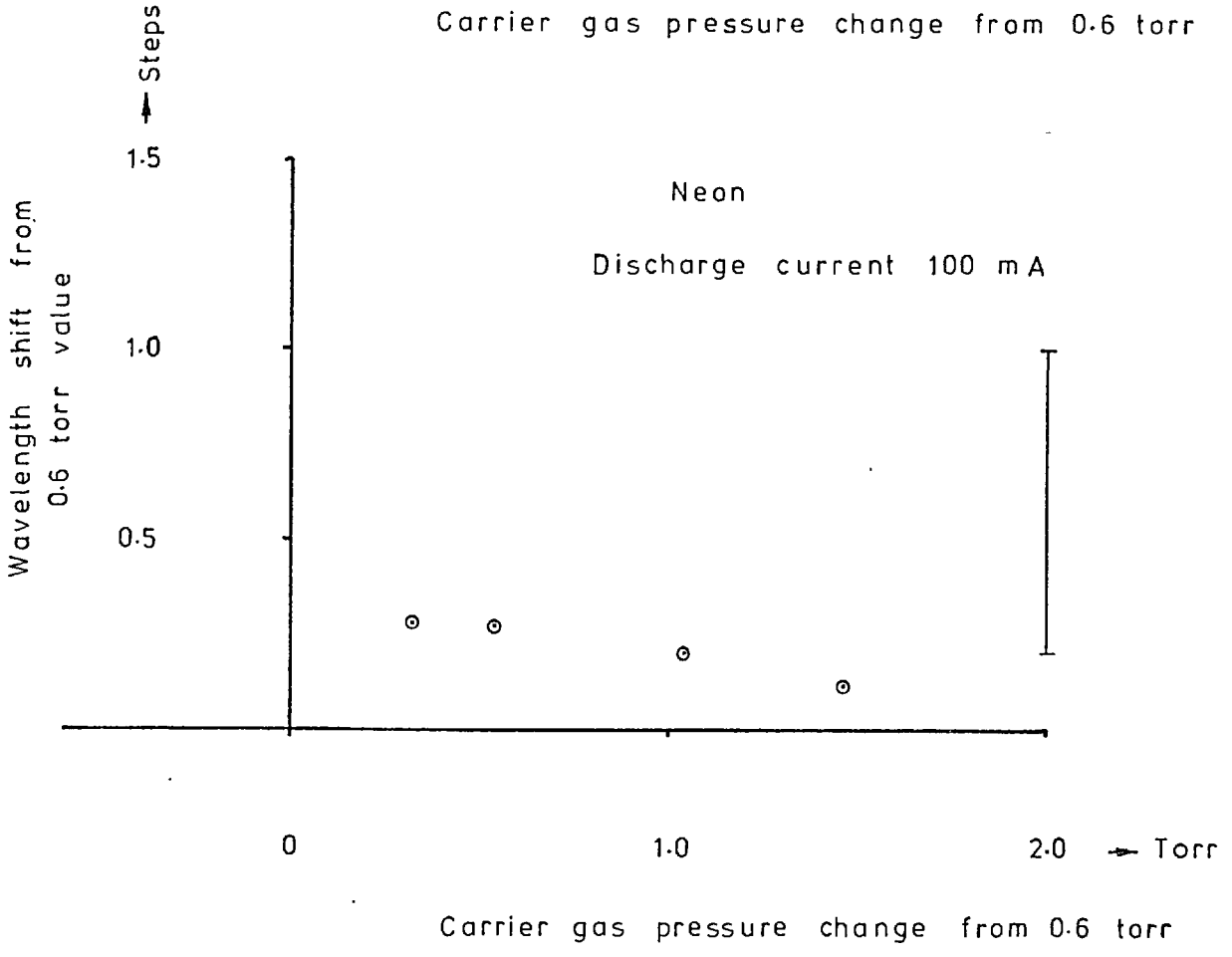

FIGURE 38. WAVELENGT SHIFT VERSUS NEON PRESSURE FOR THE λ157.7 nm LINE

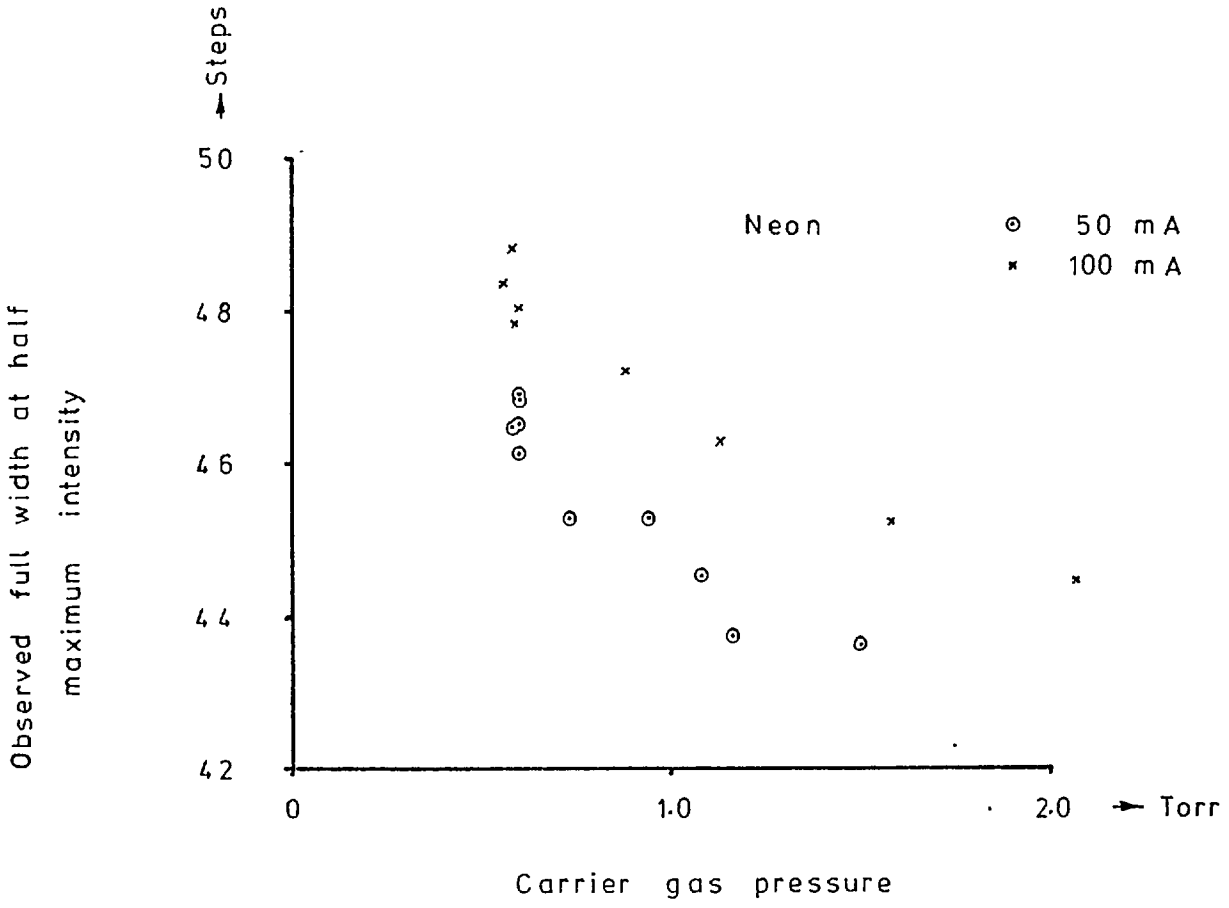

FIGURE 39. OVERALL WIDTH OF THE λ157·7 nm LINE AS A FUNCTION OF NEON PRESSURE

CHAPTER 6

DISCUSSION OF THE RESULTS

Detailed explanation of shift, width or intensity variations with source conditions is not possible. An attempt is made in this chapter to consider possible mechanisms which could explain the results. It will be shown that sputtering and self-absorption are responsible for the intensity variations with source conditions. The width of the profiles are dominated (apart ~~for~~ from the instrumental width) by Doppler broadening and self-absorption. Shift of the profiles with source conditions is not as easily explained. However, the most probable cause is that of a non-Maxwellian velocity distribution of the emitted species. Some recent work at C.S.I.R.O. Chemical Research Laboratories in Australia by Lowe (1972) also indicates that helium carrier gas gives rise to unusual widths in a hollow cathode lamp.

6.1 Variation of intensity with pressure and current

The curves shown in figures 32-35 for the spectral intensity versus pressure can be described by the following processes:-

(a) Sputtering.

Germanium gets into the discharge region by sputtering which results from the bombardment of the cathode surface by rare gas ions. The rate of sputtering would be proportional to the rare gas ion number density, N_i. Hence:-

$$\text{Rate of sputtering} \propto N_i .$$

Electronic direct excitation

$$Ge + e \rightarrow Ge^{+*} + e + e$$

would be the dominant process and hence the intensity of the observed radiation would be proportional to the rate of sputtering and also to the discharge current, I. Because N_i

is proportional to I, a square law dependence of intensity on current would be expected. N_i will also be proportional to rare gas pressure, p, for low pressure, where the electron mean free path allows acceleration to sufficiently high energy.

The rate of sputtering would also involve the energy and momentum of the rare gas ion. The heavier ion should be a better sputtering agent, if sputtering is a pure elastic collision process. This is reflected in the ratio of the absolute intensities of λ160.2nm line of GeII at 0.6 torr carrier gas pressure. From measurements, the ratio for different carrier gases is:-

$$\frac{Ne}{He} = 2.1, \quad \frac{Ne}{Ar} = 0.62.$$

The ratio of (atomic weight)$^{1/2}$ gives:-

$$\frac{Ne}{He} = 2.2, \quad \frac{Ne}{Ar} = 0.71.$$

The energy of the incident rare gas ion is dependent on the overall lamp voltage, and in particular on the cathode fall and the mean free path. Figure 36 shows the lamp voltage to be highest for helium and lowest for argon carrier gases. However, the ions would be accelerated over the cathode dark space, which for a hollow cathode would be about 0.5mm thick (see for example Hannaford (1972)) and dependent on the mean free path.

As the rare gas pressure increases, the ion attains a lower accelerated energy and hence the sputtering falls off. This effect would be most important in argon because the mean free paths are (Kaye and Laby (1966)):-

$$\frac{Ne}{He} = 0.71, \quad \frac{Ne}{Ar} = 1.98.$$

The overall lamp voltage, reflecting the cathode fall, would indicate that helium ions would be accelerated to a larger energy than neon or argon ions, assuming the same cathode fall thickness. However, this effect would probably not be important because the cathode fall thickness is unlikely to be constant.

Thus the fall off in sputtering rate with increase in pressure would be most important with argon and least with helium.

We conclude that at low pressure the intensity would rise linearly with pressure and then decrease as a result of mean free path limitations at higher pressure.

(b) Self-absorption.

As will be seen later, the GeII emission lines exhibit self-absorption. This will mean that, initially, at low rare gas pressure, the observed intensity results from the whole length of the cathode. As the pressure increases, giving rise to more sputtering and ionisation, the optical thickness increases and then, when the sputtering falls off, the optical thickness decreases and the whole cathode is observed.

From (a) we expect a square law relation between intensity and discharge current. But with self-absorption, this law would not hold at the peak intensity. Hence we would have:-

$$\text{Intensity} \propto (\text{Current})^{a},$$

where $a \simeq 2$ for low and high rare gas pressures,

$a < 2$ for rare gas pressures corresponding to the peak intensity.

A plot of log (Intensity) versus log (Current) for the three

rare gases has shown this to be the case for helium and neon. Argon exhibits a value of 'a' at high pressures as high as 5. There does not appear to be any satisfactory explanation for this observation.

(c) De-excitation of GeII excited states.

It is possible that a de-excitation process takes place before a germanium ion has had time to radiate.

Collisions between germanium ions and rare gas ions or electrons would be dominated by the coulomb interaction. Using the classical impact parameter calculation, for an electron and ion collision, we have the impact parameter, b, given by:-

$$b = \frac{ze^2}{mv_o^2} \cot \theta/2 \text{ cm},$$

where v_o is the electron velocity in cm/sec,

$z = 1$ is the ion charge,

θ is the scattering angle,

e and m are the electronic charge in esu and mass in grammes.

The time between collisions, for an electron density n_e, is:-

$$\frac{1}{\pi b\, n_e v_o} \simeq 2.5.10^{-6} \tan^2 \theta/2,$$

where we assume $n_e \simeq 10^{12} cm^{-3}$ and v_o corresponding to electron energies of 2eV; both taken from the work of Borodin et al. (1966) as typical electron parameters likely to be encountered. If collisions are to have any appreciable effect during the emission of radiation, the above time must be comparable with the excited state lifetime which is probably 10^{-8} sec (there is no experimental value for the lifetime of any GeII states).

For this to be true, θ must be small and hence no appreciable momentum could be transferred in such a collision. A similar conclusion can be drawn for germanium ion and rare gas ion collisions.

The most likely cause of de-excitation is the collision with rare gas neutrals during the germanium ion excited state lifetime. The collision rate for such a process is given by:-

$$\text{Collision rate} = \sigma n v_o, \qquad (13)$$

where σ is the cross-section for such a collision,

n is the rare gas neutral number density,

v_o is the relative velocity between neutral and ion.

The cross-section can be approximated, using the hard sphere type collision, to:-

$$\sigma = \pi (r_1 + r_2)^2,$$

where r_1 and r_2 are the radii of the germanium ion excited state and the neutral rare gas atom respectively.
Using the value of r_1 , from the equation given by Griem (1964), as $2.8.10^{-8}$cm and the value of r_2 from the work of Hindmarsh (1967) as:-

Neon	$2.12.10^{-8}$cm,
Argon	$2.82.10^{-8}$cm,
Helium	$1.77.10^{-8}$cm.

Typical value of v_o would be about 10^5cm/sec and with n given by:-

$$n = \frac{L.p}{760},$$

where L is Lochmidt's number and p the pressure in torr, we obtain, for say Helium at 1 torr, a collision time of:-

4.10^{-8} sec.

Hence, the order of magnitude of collision time would be similar to the excited state lifetime and could be an important de-excitation mechanism.

The value of v_o adopted is related to the particular rare gas used and the germanium atom and ion energy as a result of sputtering. The rare gas velocity can be assumed to correspond to the temperature of 150K; but according to the work of Bacis (1971) the temperature of argon atoms in a thorium-argon hollow cathode lamp, cooled in liquid nitrogen, peaked at about 270K at a pressure of 0.5 torr of argon.

Germanium ion velocity will be dominated by the energy of the sputtered atom. From the work such as Stuart and Wehner (1964), Stuart et al. (1969) and Bacis and Danière (1970) on the energy of sputtered atoms, we may conclude that it is possible that the germanium atoms could be sputtered with an energy as high as 5eV. The energy would be highest for argon ions and lowest for helium ions as one would expect from any simple collision theory. Hannaford (1972) has shown that, for a gold-argon hollow cathode, the effective temperature of the cathode atoms drops, through collisions with rare gas atoms, from a temperature as high as 3000K at low pressure to close to the argon gas temperature at high pressure. The work of Bacis (1971) has also shown this to be the case in a thorium-argon lamp, where the thorium temperature dropped from 400-500K at about 0.3 torr to a value which follows the argon atoms above 1.0 torr.

Without detailed knowledge of the sputtered energy it is not possible to adopt an accurate value of v_o. One may conclude that the contribution to v_o, from the rare gas atom, will be proportional to the (atomic weight)$^{-1/2}$ whereas the contribution from the sputtered atom will probably be proportional to (atomic weight)$^{1/2}$. The sputtered atom

velocity would be the larger contribution to v_o.

The difference between the collision rates given by equation (13) for different rare gases would be dominated by $(r_1 + r_2)^2$, possibly with a contribution from v_o, which would decrease with increase in pressure. Argon will have the smallest collision time and helium the largest. Hence because $n \propto \frac{p}{kT}$, where p is the carrier gas pressure, we would expect that de-excitation collisions would be most effective in argon and least in helium.

An overall picture of the intensity variation with pressure from crude theory would be as follows:-

At low pressure sputtering dominates and the intensity reflects the increase in germanium atoms in the discharge.

At large intensities the number density is such that self-absorption reduces the observed intensity which is reflected in the intensity versus current relation.

De-excitation of the GeII excited states as a result of collisions with rare gas atoms and reduction of sputtering both when the carrier gas pressure increases lead to a fall off in the intensity.

The results found by experiment shown in figures 32-35 appear to confirm, at least in general terms, the interpretation presented here.

6.2 Broadening and shift with pressure and current

There are a number of effects which could cause an emission line to be broadened and possibly shifted as a result of perturbations in the hollow cathode. The following possibilities will be discussed:-

1) Macroscopic electric fields causing Stark shifts. These would be a result of spurious stray fields within or just outside the cathode;

2) Microscopic electric fields again causing Stark shifts. These would be fields between different atomic species present in the plasma;

3) Neutral perturber pressure broadening and shift as a result of the carrier gas atoms interacting with the emitting atom, through Van der Waals forces, during the time taken to emit;

4) Plasma oscillations;

5) Resonance broadening;

6) Isotope effects;

7) Self-absorption and self-reversal;

8) Doppler broadening and Doppler shift as a result of a non-Maxwellian distribution of emitting species;

9) Momentum transfer between ions, neutrals or electrons and the emitting species.

An attempt will now be made to estimate and discuss the likelihood of each of the above effects producing the observed wavelength shifts. Estimates will be made for the λ160.2nm line of GeII.

1) Macroscopic electric fields - Stark shift.

At the sort of current densities and overall voltages encountered in the hollow cathode, it is unlikely that large enough field strengths could be set up to cause Stark shifts. However, it is useful to evaluate the order of magnitude of shifts using simple calculations.

The linear Stark effect occurs in hydrogen and hydrogen-like spectra where the levels are l degenerate and where fine structure is small compared with the level splitting caused by the fields. The linear effect produces symmetrical splitting and does not give rise to shifts.

Quadratic Stark effect would apply to germanium where l is non-degenerate. The splitting is given (Kuhn (1962)) by:-

$$\Delta T = \frac{a_o^3}{16hc} \frac{F^2}{Z^4} n^4 \left\{ 17n^2 - 3(n_2 - n_1)^2 - 9m^2 + 19 \right\} \ cm^{-1},$$

where a_o is the Bohr radius in cm,

F is the field strength in esu,

Z is the atomic number,

n is the Principal quantum number,

n_1 and n_2 are electric quantum numbers such that:-

$$n_1 = 0, 1, 2 \ldots\ldots n-1,$$

$$n_2 = 0, 1, 2 \ldots\ldots n-1,$$

$$m = n - n_2 - n_1 - 1.$$

If F is expressed in volts/cm, then the splitting becomes:-

$$\Delta T = 5{\cdot}22.10^{-16} \frac{F^2}{Z^4} n^4 \left\{ 17n^2 - 3(n_2 - n_1)^2 - 9m^2 + 19 \right\} \ cm^{-1}.$$

It is possible for this to give rise to wavelength shifts if the splitting is small compared with the Doppler width. For the λ160.2nm line of GeII, the largest splitting will be of the upper 5s term. For a field of 10^3 volts/cm we obtain:-

$$\Delta T \simeq 3.10^{-11} \ cm^{-1}.$$

This is negligible. Even at a field of 10^6 volts/cm this would hardly contribute to the broadening of the emission line. This agrees with the experimental findings of Van Veld (1951) who showed that no significant broadening in the arc spectrum was observed in the λ470 to λ220nm region with an electric field strength of up to 25kV/cm.

2) Microscopic electric fields - Stark broadening and shift.

Atomic wavefunctions are modified in the presence of an electric field and produce level splitting. In a plasma, an emitting atom or ion is in the field of electrons and ions. Because of the distribution of fields, the observed profile becomes a convolution of many individual emissions arising from emitters under the influence of different electric fields.

Electrons, with their high velocity, have to be treated by what is called an impact approximation. This assumes only one collision between emitter and electron takes place during a typical collision duration. This is a good approximation for low density plasmas encountered in a hollow cathode. The treatment of Lindholm (1941) will be used to estimate the impact width and shift.

Ions, with their lower velocity, are treated using a quasistatic approximation. This assumes the ions are effectively stationary and the effect on the emitter is a statistical average of many fields. The treatment is based on the work of Holtsmark (1919) and Margenau and Lewis (1959).

Later theory for electron and ion processes is given by Griem (1964) and reviewed by Cooper (1966).

Impact approximation - electrons.

This leads to the following expression for the half maximum intensity width, 2w, and shift, d, for the quadratic Stark effect:-

$$2w = 3{\cdot}79 \cdot 10^{-10} C_4^{2/3} \bar{v}^{1/3} n_e \ cm^{-1}$$

$$d = \sqrt{3}\, w,$$

where n_e is the electron number density in cm^{-3},

C_4 is the interaction constant,

$\bar{v}$ is the mean electron velocity in cm/sec.

A typical value of C_4 might be (Margenau and Lewis (1959)) 2.10^{-12} cgs units. Assuming $n_e \simeq 10^{12}cm^{-3}$, which is consistent with the probe measurements of Borodin et al. (1966), and the electron temperature T_e = 10 eV, giving $\bar{v} = 2.10^8$cm/sec, then we obtain:-

$$d \simeq 3.10^{-3}cm^{-1}.$$

Thus it is possible that, under the assumptions made, there could be a contribution towards the shift and broadening from electronic Stark effects. However, the estimate of T_e = 10 eV will only apply to about 10% of the electrons according to the work of Borodin et al. (1967) and n_e is probably overestimated. The dominant uncertainty is in the value of C_4.

Some semi-classical calculations have been performed on the λ160.2nm and λ164.9nm lines of GeII by Jones (1972) for electrons as perturbers. These indicate a shift and width which is about $2.10^{-5}cm^{-1}$ for the same values of n_e and T_e. Hence, it is unlikely that electron perturbers contribute to the observed width or shift.

Quasi-static approximation - ions.

The simple treatment of broadening by a static 'sea' of ions is treated by Holtsmark (1919) and considers a single ion and a single radiator. The observed profile $I(\Delta\nu)$ is given, for the quadratic Stark effect, by:-

$$I(\Delta\nu) = \frac{3}{4\Delta\nu}\left(\frac{\Delta\nu_o}{\Delta\nu}\right)^{3/4} exp\left\{-\left(\frac{\Delta\nu_o}{\Delta\nu}\right)^{3/4}\right\}$$

where $$\Delta\nu_o = \frac{C_4}{2\pi}\left\{\frac{4\pi n_i}{3}\right\}^{4/3}$$

and C_4 is the interaction coefficient similar to that used in the impact approximation,

n_i is the number density of ions in cm^{-3},

ν is the frequency in sec^{-1}.

Examination of the intensity distribution I $(\Delta\nu)$, given above, shows that any overall shift of the profile will be of the same order of magnitude as $\Delta\nu_0$. Hence, evaluation of $\Delta\nu_0$ should indicate the contribution to the shift and width from ionic Stark effect.

Using the value of $C_4 = 2.10^{-12}$ cgs units and $n_i = 10^{12} cm^{-3}$, we obtain:-

$$\Delta\nu_0 \simeq 2.10^{-4} sec^{-1}$$

$$\therefore \Delta\bar{\nu}_0 \simeq 7.10^{-7} cm^{-1}.$$

Thus the contribution from ion perturbers, other than germanium ions, will be negligible.

3) Neutral perturbers.

Interatomic attractive forces whose potential varies as $1/r^6$ where r is the atomic separation, dominate the interaction of two dissimilar atoms. These are called Van der Waals forces and are associated with the polarisation of the perturbing atom by an effective dipole which results from the perturbed atom being in an excited state. Thus a perturber will produce an effect which is proportional to its polarisibility, α, which for the three rare gases used is (Allen (1955)):-

He	$2.07.10^{-25} cm^3$,
Ne	$3.96.10^{-25} cm^3$,
A	$16.54.10^{-25} cm^3$.

The width, 2γ, and shift, β, of an observed line profile can be estimated using the Lindholm (1945) and Foley (1946) theory as:-

$$2\gamma = \frac{17.0}{2\pi} C_6^{2/5} \bar{v}^{3/5} N \cdot sec^{-1}$$

$$\frac{2\gamma}{\beta} = -2.8$$

where $C_6 = C_{6i}(n, \ell) - C_{6f}(n', \ell')$

and $$C_6(n, \ell) = \frac{e^2 \alpha a_o^2 n^{*2}}{2hZ^2} \left[5n^{*2} + 1 - 3\ell(\ell+1) \right],$$

where $\bar{v}$ is the average perturber velocity in cm/sec,

N is the perturber number density in cm^{-3},

l, n, n^* are the orbital, principal and effective quantum numbers of the emitting atom level,

Z is the emitter atom charge when the radiating electron is removed (= 2 for GeII).

For the λ160.2nm line of GeII corresponding to the transition $5s\ ^2S_{1/2} - 4p\ ^2P_{1/2}$ we have:-

$$n_i^* = 2.57,\ l_i = 0$$

$$n_f^* = 1.85,\ l_f = 1.$$

Using values of $\bar{v}$ corresponding to a rare gas temperature of 150K and putting N in terms of the pressure of the rare gas in torr, we obtain the values of β shown in table 5 for the shift in units of $10^{-3} cm^{-1}$ per torr of rare gas.

Griem (1964) gives a similar equation for Van der Waals broadening and shift which does not directly involve the classical polarisibility. Table 5 also gives the results using this equation and agreement is very good. Higher order interaction terms, as in the work of Hindmarsh (1967), are unlikely to alter the results by more than an order of magnitude which is the amount required to explain the observed shifts. The calculations also indicate that all three perturbers would give similar shifts, which is contrary to the results observed. However, they do indicate a red shift and one that increases proportionally with rare gas pressure.

Perturber	Shift in $10^{-3}cm^{-1}$	
	Lindholm - Foley	Griem
He	-0.20	-0.29
Ne	-0.16	-0.16
A	-0.23	-0.27

TABLE 5. Calculated neutral perturber shift for the three rare gases used in the hollow cathode. The negative sign indicates a red shift and the values correspond to a rare gas pressure of 1 torr.

Hence, as with Stark broadening and shift, this effect cannot be eliminated as a cause of the observed shifts but it does appear that the results are rather too small to be significant.

4) Plasma oscillations.

Satellite spectral lines, symmetrically disposed about the parent emission line, can arise when longitudinal plasma oscillations are present. The satellites are separated from the parent by the plasma

frequency.

The plasma frequency is given by Baranger and Mozer (1961) as:-

$$\Delta\nu = \left(\frac{4\pi n e^2}{m}\right)^{1/2} \text{ sec}^{-1},$$

where n is the electron density in cm^{-3}.

For $n \simeq 10^{12} cm^{-3}$ we have:-

$$\Delta\nu = 5{\cdot}6 \cdot 10^{10} \text{ sec}^{-1}.$$

Thus satellites would occur at $\nu \pm \Delta\nu$ where ν is the emission line frequency. In wavenumbers we have:-

$$\Delta\bar{\nu} = 2 \text{ cm}^{-1}.$$

Hence we expect that if plasma oscillations are present then the satellites would occur at $2cm^{-1}$ from the main line which is 10 times too far to distort the observed profile of the λ160.2nm line. Because $\Delta\bar{\nu} \propto n^{1/2}$ we would not expect plasma oscillations, if present, to be significant unless n was about $10^{10} cm^{-3}$ which is smaller than the value expected in the hollow cathode.

5) Resonance broadening.

When an atom or ion with an electron in its ground state comes into close proximity with a similar species, but with an electron in its excited state, a type of resonance is set up between the two systems. Interatomic forces whose potential energy is proportional to $1/r^3$ are set up, giving rise to symmetrical broadening of the emission profile. An estimate of the broadening, called resonance broadening, is obtained using the expression given by Kuhn and Vaughan (1964) as:-

$$\delta = \frac{k\lambda e^2}{8mc^2} f_{jj'} N \text{ cm}^{-1}.$$

where $f_{jj'}$ is the oscillator strength of the resonance transition,

N is the number density of the atoms or ions in cm^{-3},

k is a numerical constant which depends on the particular theory used to derive the expression; it varies between 1.25 and 2, the larger value will be used.

Although the value of f_{jj}, is not known, it is reasonable that it will be quite large, say 0.3 for the λ160.2nm of GeII. Using the value for N of $10^{12}cm^{-3}$, we calculate the resonance broadening to be:-

$$\delta \simeq 4.10^{-7}cm^{-1}.$$

Hence resonance broadening at these number densities is negligible.

6) Isotope effects.

Germanium, with atomic number Z = 32, occurs naturally with the following atomic weight, A, abundances ^{70}Ge - 20.5%; ^{72}Ge - 27.4%; ^{73}Ge - 7.8%; ^{74}Ge - 36.5%; ^{76}Ge - 7.8%.

Hyperfine structure results from the interaction of nuclear and electronic angular momenta. When Z and A are both even, nuclear spin is also zero and no splitting occurs. The odd germanium isotope ^{73}Ge with 7.8% abundance has a nuclear spin $I = 9/2$. The configuration of GeII giving rise to the λ160.2nm and λ164.9nm lines has a single outer p electron. If we treat the configuration as alkali-like we can estimate the splitting of the upper and lower states.

For the $5s\ ^2S_{1/2}$ upper level, the total splitting, a_s', is given by Kuhn (1962) as:-

$$a_s' = 0.00849\ \frac{Z Z_a^2}{n^{*3}}\ \frac{\mu'}{I}\left(1 - \frac{d\Delta}{dn}\right) cm^{-1},$$

where $Z_a = 2$ for GeII,

μ' is the nuclear magnetic moment in nuclear magnetons;

$\mu' = -0.88$ for ^{73}Ge (Kuhn (1962)),

n and n^* are the principal and effective quantum numbers respectively,

Δ is the quantum defect, $\Delta = n - n^*$,

$\frac{d\Delta}{dn}$ is the change in the quantum defect with n in the particular term, we will assume $\frac{d\Delta}{dn} = 0$.

This gives a value:-

$$a_s' \simeq 12.5.10^{-3} cm^{-1}.$$

The lower state $4p\ ^2P_{1/2,3/2}$ has a splitting, a_J', given by:-

$$a_J' = \frac{\Delta T\ \mu'\ L(L+1)}{I.1836.1(Z-4)(L+1/2)J(J+1)} \quad cm^{-1},$$

where ΔT is the term splitting = 1767 cm^{-1},

L and J are the orbital and total angular momentum quantum numbers.

For the $J = 1/2$ we obtain:-

$$a_{1/2}' \simeq 12.10^{-3} cm^{-1},$$

and for $J = 3/2$:-

$$a_{3/2}' \simeq 2.4.10^{-3} cm^{-1}.$$

Hence, with an abundance of 7.8%, it is unlikely that hyperfine splitting of the ^{73}Ge isotope would significantly contribute to the broadening of the overall line profile. There is no evidence in the literature to contradict this conclusion.

Isotope shifts in the arc spectrum of germanium have been observed for a few transitions by Heilig et al. (1966). Their results show the largest to be $(3.0 \pm 0.5).10^{-3} cm^{-1}$. Deverall et al. (1954) utilised an atomic beam of natural germanium and found there was no

detectable splitting of the lines, greater than $5.10^{-3}cm^{-1}$, for eight different transitions between the lowest even level and differing odd levels.

These results are consistent with the expected small isotope shifts from an atom near the centre of the periodic table. Mass shifts decrease with increase in atomic weight provided no d-electrons are involved in the transition; volume or field shifts are important for large values of A, usually above 100 and where transitions involve s electrons.

Hyperfine splitting and isotope shift combined with self-absorption can very often explain unusually wide emission lines from hollow cathode sources. Hannaford (1972) claims this explains the anomalously high apparent Doppler width obtained by Kreye and Roesler (1970) for gold and argon lines emitted in a hollow cathode source.

In the present work, it is unlikely that isotope effects or hyperfine structure contribute to the width or shift of the profiles.

7) Self-absorption and self-reversal.

When light is emitted by an atom or ion in a plasma, it can only be observed by viewing from outside the discharge region. Between the emitter and observer, it is possible for intermediate atoms to absorb the radiation. As a result of this process, the emission spectral profile can be modified according to the degree of absorption and the temperature distribution of the absorbers. If the temperature is constant self-absorption flattens the observed spectral profile. Observation through cooler absorbers produces self-reversal, where the centre of the line is preferentially reduced.

The absorption is given, from Griem (1964), as:-

$$k(\tilde{\nu}, x) = \frac{\pi e^2}{m c^2} \int N L(\tilde{\nu}, x),$$

where f is the absorption oscillator strength,

N is the absorber number density in cm^{-3},

$L(\bar{\nu}, x)$ is the normalised line shape function for a wave-number $\bar{\nu}$ at a position x in the plasma.

For a Doppler dominated emission profile with no dependence on x we have:-

$$L(\bar{\nu}, x) = \left(\frac{4 \log_e 2}{\pi}\right)^{1/2} \frac{1}{d_{\bar{\nu}}} \exp\left(-\frac{4 \log_e 2 (\bar{\nu} - \bar{\nu}_o)^2}{d_{\bar{\nu}}^2}\right),$$

where $$d_{\bar{\nu}} = \bar{\nu} \cdot 7.16 \cdot 10^{-7} \sqrt{\frac{T}{A}},$$

for a temperature, T, and atomic weight, A.

The peak absorption coefficient corresponding to $\bar{\nu} = \bar{\nu}_o$ is k_o where:-

$$k_o = \frac{\pi e^2}{m c^2} f N \left(\frac{4 \log_e 2}{\pi}\right)^{1/2} \cdot \frac{1}{d_{\bar{\nu}}} \quad cm^{-1}.$$

For the λ160.2nm line of GeII assuming f = 0.3, an ion density of $10^{12} cm^{-3}$, temperature 150K and absorbing length of x = 2cm, then the optical thickness $k_o x$ is:-

$$k_o x \simeq 7.$$

Hence, under these conditions, virtually no radiation emitted at the far end of the cathode would be observed outside the discharge region.

If $I_e(\bar{\nu})$ is the emission per unit length in the discharge, then the observed intensity at the centre of the emission is:-

$$\int_{x=0}^{x=2} I_e(\bar{\nu}_o) \exp(-k_o x)\, dx$$

$$= \frac{I_e(\bar{\nu}_o)}{\approx 3.5}$$

The assumptions for N, T and f are probably overestimated, but nevertheless we see that self-absorption will be a very important broadening mechanism for these ground state transitions.

In practice T will not be constant over the observing path and a certain amount of self-reversal will be present.

Self-absorption has been shown to be very important in the GeII λ160.2nm line profile. The variation of intensity with current in figures 32-35 has been shown in section 6.1 to illustrate the onset of self-absorption when the carrier gas pressure corresponds to the peak sputtering rate and hence peak output intensity. The above calculations are clearly overestimating the absorption but, because of the uncertainty of N, T and f, this is not surprising.

The observed total width of the profile, shown in figures 30 and 31, also reflect self-absorption in the cases of argon and neon, where the self-absorption and width decrease when the carrier gas pressure increases and sputtering rate decreases as seen in section 6.1. For helium the sputtering is smaller and the indication of an increase in width with pressure probably results from the same mechanism as the red shift.

Self-absorption appears, at first sight, to change only the observed width of an emission profile. However, during the course of the work on the echelle spectrometer, a number of lines (NI at λ120nm, HgI at λ184.9nm and GeI at λ209.4nm) have been observed which show

self-reversal where the absorption and emission profile were centred at different wavelengths. The red side of the effective doublet was increased in intensity with respect to the blue side. This effect has been observed in the visible spectral region by Rowley (1962) and Tako et al. (1962). An attempt to evaluate the change in overall shift of the profile when the pressure of carrier gas was increased, in the case of the GeI λ209.4nm, did not produce any satisfactory conclusion. This may be because the top 20% of the observed profile was not used in the calculation of centre of gravity and it is this region which shows the asymmetry of the profile as observed on the x-y recorder. It is not surprising that this is a negative result because the self-reversal was very small and probably shows itself as an asymmetry in the effective doublet peaks before it is possible to determine the centre of gravity change especially as the uncertainty of shift measurement is about 1% of the full width at half maximum intensity.

8) Doppler width and shift as a result of a non-Maxwellian velocity distribution of the emitting species.

The Doppler width of an emission line is given by:-

$$\Delta \bar{\nu} = \bar{\nu} . 7.16.10^{-7} \sqrt{\frac{T}{A}} .$$

For a temperature of 150K at λ160nm this becomes, for germanium:-

$$\Delta \bar{\nu} = 65.10^{-3} cm^{-1} .$$

Evidence from the work of Bacis (1971) indicates that the Doppler width, in a liquid nitrogen cooled hollow cathode, of the cathode atoms reduces from as high as 450K at low carrier gas pressures to the cathode temperature at high pressure. Hence, the estimate of $\Delta\bar{\nu} = 65.10^{-3} cm^{-1}$ may well be only half the true Doppler width. Decrease in Doppler width as the carrier gas pressure increases, as a result of the mean free path decreasing and more collisions with the

cathode walls, could also explain the decrease in overall emission profile width. For the same rare gas pressure, helium, with the longest mean free path, might be expected to exhibit the largest Doppler width and argon the smallest. In fact this is not verified by the results shown in figures 30 and 31. However, it is possible that Doppler width change with rare gas pressure is contributing to these curves.

Although Doppler broadening is symmetrical this assumes the velocity distribution of the emitting atoms is Maxwellian. We will now look at a few reasons why this may not be true for all the hollow cathode negative glow emission.

It is useful to calculate the velocity, v, of an emitting atom required to produce a wavenumber shift of say $5.10^{-3}cm^{-1}$. Now:-

$$\Delta\bar{\nu} = \bar{\nu}\,\frac{v}{c}$$

which for the λ160.2nm line and $\Delta\bar{\nu} = 5.10^{-3}cm^{-1}$ gives:-

$$v \simeq 25 \text{ m/sec},$$

which is not a particularly large velocity.

The lamp is used in a continuous flow mode with a gas throughput of 0.005l/sec at about 1 torr pressure. With typical lamp dimensions of 1 cm this only corresponds to velocities much smaller than the 25 m/sec. Hence, gas streaming or turbulence cannot cause such a shift.

If the sputtered germanium atoms are ejected in a preferred direction, this could give rise to Doppler shifts. Stuart and Wehner (1964) indicate that the energy of sputtered copper atoms, by rare gas ions, depends strongly on the direction of ejection.

Patterson and Tombin (1962) showed that departures from a cosine distribution law arises from the contribution of atoms from different

depths. Lower energy ions penetrate least and hence restrict the sputtering to the upper layers in which case the cosine law is approached. Comparison with the present hollow cathode would indicate that argon ions would produce maximum deviation from cosine distribution whilst helium would produce least deviation. Hence, one might expect argon to produce the largest deviation from Maxwellian distributions.

Change in cathode structure, single crystal, polycrystalline (as in the present cathode of cast germanium) or amorphous, could be responsible for changes in the sputtering angular distributions if these are related to lattice directions. Stuart et al. (1969) showed that this does not seem to play an important role in the ejection energy distributions.

Thus although sputtering could result in non-Maxwellian velocity distributions it is unlikely that this is important. Observations are made in the centre of the negative glow region where, owing to the small mean free paths (about 0.1mm), we would expect collisions to have elliminated any such effects.

A more likely cause of Doppler shifts could be stray electric fields within or just outside the hollow cathode. If ions are being accelerated in a field of E volts/cm whilst radiating, then, assuming a direct excitation process:-

$$e + Ge \rightarrow Ge^{+*} + e + e,$$

the shift $\Delta\bar{\nu}$ is given by:-

$$\Delta\bar{\nu} = \bar{\nu}\,\frac{E e \tau}{300\, M c},$$

where τ is the excited state lifetime in sec, and M the atomic weight in g and e, the electronic charge, in esu.

For $\tau \simeq 10^{-8}$ secs and $\Delta\bar{\nu} = 5.10^{-3}\,cm^{-1}$, as before, the electric field strength capable of producing the necessary Doppler shift is:-

$$E \simeq 15 \text{ volts/cm.}$$

This is a relatively small electric field strength and it is possible that such fields could easily exist within the discharge region. A red shift would be obtained if observations are made through the anode and acceleration being towards the cathode. Change in the red shift with lamp conditions would depend on the way in which the electric field changes, which is not known. If de-population of the ionic excited state by collisions with neutral rare gas atoms is important, then increase in pressure would produce a blue shift (strictly a reducing red shift). Such a shift has been observed by Berry and Roesler (1970) with an aluminium hollow cathode used to excite the λ468.6nm line of HeII. Different excited state lifetimes and change in plasma size were used to explain the observed shifts.

This sort of effect cannot explain the observed shifts in GeII because of the different direction of the shifts.

An alternative explanation is that there is a complex electric field distribution within the cathode space. Reversal of the field could be possible, especially as the germanium is a semiconductor with a large electrical resistivity. However, as observations are made in the central 50% of the cathode area it is unlikely that this is an important factor.

Another explanation is that there exists, just outside the hollow cathode, a strong electric field. Acceleration of germanium ions towards the cathode could then take place. It is then possible for the germanium ions to exhibit a Doppler shift which could change as a result of the spatial configuration of the electric field changing with source conditions. This will now be examined in more detail.

External electric fields causing Doppler shifts.

Electrical probe measurements just outside a hot hollow cathode made by Medicus (1965) show that electric fields, as high as 45V/cm, can occur over very small distances which appear as a single visible

striation, termed a 'double layer'. Boyd and Twiddy (1960) show that striations in a positive column can be associated with field strengths as high as 100 or 1000V/cm.

Having established the possibility of large electric fields, just outside the open end of the hollow cathode, it is useful to examine the frequency distribution of the radiation emitted by ions when observation is made parallel to the accelerating electric field. Frish and Kagan (1948) have calculated such a distribution and find it can be described by a half Doppler profile whose width a half maximum intensity is $\Delta\bar{\nu}$ where:-

$$\Delta\bar{\nu} = \frac{\bar{\nu}}{c}\left(\frac{\log_e 2}{b}\right)^{1/2} \qquad (14)$$

and $$b = \frac{M}{2eEd},$$

where $\bar{\nu}$ is the wavenumber,

M is the ionic mass in g,

E is the electric field strength in esu/cm,

d is the mean free path in cm.

The mean free path for an ion moving in a neutral rare gas can be described by the effective hard-sphere cross-section $\pi(r_1 + r_2)^2$, where r_1 and r_2 are the atomic radii of the rare gas atoms and the germanium ions respectively as given in section 6.1. Hence, we can evaluate equation (14), for say neon rare gas at 1 torr pressure, for the λ160.2nm line of GeII and E of 100 volts/cm. This gives

$$\Delta\bar{\nu} \simeq 300.10^{-3}\text{cm}^{-1}.$$

Combination of this asymmetrical profile with the Doppler profile from the rest of the cathode would lead to an overall gaussian profile with asymmetrical red wing (observing through the anode). From

equation (14) the shift should decrease with increase in pressure of the rare gas, which is opposite to the observed shifts. This may be because:-

(a) The boundary between the negative glow and positive column, i.e. the double layer where the strong fields occur, may move into the cathode on increase in carrier gas pressure and hence be capable of accelerating a greater proportion of the germanium ions whose distribution of number density would fall off rapidly with distance from the cathode. Observation of the discharge by eye shows that this does happen, especially with helium. As the rare gas pressure increases the glow contracts into the hollow cathode.

(b) Change of electric field with carrier gas pressure could also lead to a change in the acceleration. The overall lamp voltage has been shown in figure 36, but gives no indication of the double layer field strength, except that it is inevitably a function of lamp conditions.

(c) Self-absorption has been shown to be important for the ground-state transition λ160.2nm of GeII. At low rare gas pressure corresponding to maximum intensity, where self-absorption is important because of the large Ge ion number density, the observed radiation will be from the anode end of the cathode and contain a greater proportion of emitting ions capable of exhibiting red shifts. This proportion will decrease as the pressure increases, hence producing a blue shift. Increase in lamp current with its associated number density increase would produce a larger red shift.

(d) Boyd and Twiddy (1960) report positive column striations, which loose definition on increase in discharge current and

increase in impurity. There is no positive evidence of the impurity being important other than the presence of helium. There appears to be little change in shift with discharge current.

From the calculations, although only rough assessments of the possibility of external fields causing shifts can be made, it is clear that the small magnitude of the observed shifts could easily be a result of such a process and equation (14) shows that this would be most important in the case of helium and least for argon (based on the dependance on mean free path). This is basically because germanium ions can attain a higher velocity when the mean free path is longer. The variation with pressure is probably the result of spatial changes in electric field distribution.

9) Momentum transfer.

Contributions to non-Maxwellian velocity distributions as a result of electron, rare gas ion, rare gas neutral collisions can be ruled out as follows.

Collisions between electrons and ions would be dominated by the coulomb interaction. Evaluation of the classical scattering for electrons and rare gas ions shows that these cannot transfer significant momentum during the lifetime of the excited state.

Collisions with rare gas neutrals are unlikely to produce anything other than Maxwellian velocity distributions and can be ignored as sources of shifts.

6.3 Conclusion

It is clear that the Doppler effect and self-absorption are the dominant spectral line broadening mechanisms. The experimental results shown in figures 30 and 31 indicate that self-absorption is certainly

present. The observed width is of course dominated by instrumental limitations and as already mentioned there is no way of obtaining the true emission line profile. An interesting excercise was undertaken to determine how much of the observed profile was gaussian and how much lorentzian. The results showed that the profile was almost completely gaussian and on increase in carrier gas pressure beyond the maximum intensity value it became even more gaussian-like. This probably reflects the decrease in self-absorption on increase in pressure as a result of the Ge ion number density decrease.

The shifts probably result from electric fields causing differential Doppler effects. Changing the cathode from solid germanium to aluminium caused a complete change in shift as seen in figures 24 and 29 for neon as a carrier gas. Although there is a possibility of sputtered aluminium acting as a third body in any collision processes, it is unlikely that it has a significant effect on the excitation of GeII spectra. Added complication is that the intensity pressure relation for the aluminium cathode, shown in figure 35, is noticeably different from the solid germanium curve in figure 32. An important observation in the case of the aluminium cathode was that when the neon pressure was increased the discharge did not contract longitudinally into the hollow cathode. In other words there did not appear to be any evidence of a double layer effect.

It is not surprising to conclude that the observed shifts cannot be accounted for in a satisfactory manner, although it is hoped that some of the important mechanisms have been considered and an attempt at evaluation made.

RECOMMENDATIONS

The results that have been presented are limited by the resolving power of the spectrometer. Use of an interferometer, as proposed at N.P.L., will enable absolute wavelength measurements to be undertaken together with detailed fine wavelength shift measurements. It would also enable the line profile, of say the λ160.2nm line, to be determined and hence used to obtain the spectrometer instrumental function by de-convolution. The future advent of vacuum altraviolet lasers or frequency doubling techniques could open up further possibilities for wavelength standards, but these are unlikely to be of general use to the spectroscopist for some years.

As far as the present work is concerned there are a few points worth mentioning for possible development. These are divided into two categories, first the spectrometer and second the source.

Higher instrumental resolving power could be obtained in the spectrometer by reducing the geometrical aberrations. With the present high blaze echelle this could be done by increasing the focal length of the optics to say 3m. However, a more practical short term method could be to employ a holographic grating used at a smaller angle of incidence, the latter reducing the residual coma.

Systematic errors in the measurements, due to the possibility of change in optical illumination with source conditions, could be overcome using a focussing mirror to image the source onto the predisperser entrance slit, despite the inevitable loss in overall efficiency. This could also enable different sources to be compared with each other and spatial emission characteristics investigated.

Lack of signal could be offset by the use of a photomultiplier with lithium fluoride window.

An image converter instead of an exit slit could enable the

information collection rate to be increased, but the spatial resolution of such devices is not at present small enough; it would require a resolution of about 1μm.

One of the major uncertainties about the spectral shifts observed is the influence of impurity on the observations. Employing a better pumping system for evacuating the lamp and removing impurities in the gas supply could lead to a better understanding of the shifts.

Further investigations of the hollow cathode lamp could be undertaken if observations of the emitted light were made looking in the opposite direction (not through the anode). Although this cannot be done with the present lamp design, it may be possible to construct such a lamp and still satisfy the experimental constraints. Such observations would enable the electric field hypotheses to be examined in greater detail.

Geometry of the hollow cathode lamp can be investigated in greater detail when the uncertainty of the shift measurements is reduced to about 1 or 2 parts in 10^8. Change in hollow cathode diameter and length would be two important parameters to be varied.

C O N C L U S I O N

It has been shown, in this thesis, that the GeII lines examined are easily excited in a simple liquid nitrogen cooled hollow cathode discharge lamp. Neon, with its intermediate sputtering rate, is the best carrier gas to give minimum shifts and moderate intensity. The disadvantage of the use of argon is the rapid fall off in window transmission as a result of the large sputtering rate. Helium appears unsuitable as the carrier gas because of the large wavelength shifts that it produces and the low sputtering rate and hence low intensity of GeII emission.

Typically, for the λ160.2nm line, shifts are less than 0.6 steps/torr of neon at 50mA discharge current. With 1 step $\equiv$ 0.012pm $\equiv$ $4.7.10^{-3}cm^{-1}$ $\equiv$ 7.5 parts in 10^8; we see that provided the neon pressure is maintained, such that the observed intensity does not drop below 50% of its maximum value, the wavelength shift will be less than 5 parts in 10^8. Although discharge current does not change the wavelength by more than 0.2 $\pm$ 0.3 steps for a change of 50 to 100mA, it is advantageous to reduce self-absorption and Doppler broadening by keeping the current as low as possible.

Clearly, as far as discharge conditions are concerned, it should be possible to measure the λ160.2nm and λ164.9nm lines absolutely to a precision of $\pm$ 5 parts in 10^8 by using neon as carrier gas at 0.6 $\pm$ 0.4 torr and operating at a current of between 25 and 50mA. Similar conclusions apply to the λ157.7nm line and other members of the triplet.

The absolute wavelength measurement of these lines will be undertaken in the near future at the National Physical Laboratory.

A C K N O W L E D G E M E N T

The work described in this thesis has been carried out as part of the Research Programme of the National Physical Laboratory.

I am much indepted to Dr. A.H. Cook for early encouragement and guidance and to Dr. P. Dean for continued support in the programme. I would like to thank Lady Anne Thorne of Imperial College, Dr. W.R.C. Rowley, Dr. G.H.C. Freeman and Mr. E.J. Gillham for many useful discussions and advice.

For the detailed design of the spectrometer, I am indebted to the efficient work of P.E. Routledge. For the excellent performance of the instrument I owe much to the skills of J. Etherington and his colleagues.

I would also like to thank the various other people with whom I have discussed problems over the five years spent on the project.

Lastly, I would like to thank my wife, Christine, for typing the thesis.

I am grateful to the Director for permission to use the results for submission as a thesis.

A P P E N D I X

The following pages contain reprints of the references:-

Preston, R.C., Asymmetry in the diffraction pattern of a grating due to periodic errors, 1970, Optica Acta, 17, 857.

Preston, R.C., Reduction of residual coma and astigmatism in a 1.5m Czerny-Turner spectrometer, 1970, J. Phys. E., 3, 737.

Preston, R.C., Ray-tracing for a two-mirror spectrometer and optimisation of a 1.5m Czerny-Turner instrument, 1970, N.P.L. Quantum Metrology Report No. 13.

OPTICA ACTA, 1970, VOL. 17, NO. 11, 857–867

Asymmetry in the diffraction pattern of a grating due to periodic errors

R. C. PRESTON

Division of Quantum Metrology, National Physical Laboratory, Teddington, Middlesex

(*Received* 19 *February* 1970)

Abstract. The effect of diffraction grating errors of low spatial frequency is investigated numerically and analytically.

It is shown that such errors can produce diffraction patterns in which the intensities of subsidiary maxima do not obey a simple wavelength variation law because of the interaction of Rowland ghosts which are close to the central maximum. However, shift of the line profile does obey a simple variation law under certain assumptions. Typically, the shift for a single cycle error of amplitude $\lambda/80$ in the wavefront would be about $3\frac{1}{2}$ per cent of the half-intensity width. General results for any phase distribution in the wavefront lead to the conclusion that a symmetrical diffraction pattern can only be derived from a symmetrical wavefront and not, in general, from an anti-symmetrical one.

1. Introduction

When high quality diffraction gratings are used for accurate comparisons of wavelength, or for examining spectral line profiles, it is desirable to know how closely the diffraction pattern produced by the grating approximates to that of an ideal grating and, in particular, the degree of asymmetry in the pattern and its variation with wavelength. One common and sensitive way of investigating this is by obtaining an interferogram of the diffracted wavefront against a reference wavefront and then calculating the diffraction pattern from the observed phase distribution.

This calculation can be done by computing numerically the Fourier transform of the complex amplitude distribution in the wavefront. However, to obtain a more general insight into the relation between phase distribution and the diffraction pattern, it is necessary to obtain an analytical relation between the two. This of course can only be done for a few special types of distribution [1]. The type treated here is a one-dimensional periodic variation across the width of the diffracted wavefront. This case has been treated by Rowland [2] for variations of high periodicity, such as commonly occur in practice because of ruling engine defects, and which give rise to the well-known Rowland ghosts. The purpose of this paper is to extend this analysis to the case where the periodicity is small, and the Rowland ghosts approach the central diffraction peak and affect its shape.

2. Periodic errors

Different forms of errors in the wavefront observed from a plane diffraction grating can be examined by using the expression for the amplitude in the diffraction pattern given by

$$A(\beta) = \int_{\eta=-1}^{+1} \exp(i\beta\eta) \cdot \exp[i\Delta(\eta)] \cdot d\eta, \qquad (1)$$

where the various parameters involved are defined, with the aid of figure 1, as follows:

β represents the angular coordinate in the diffraction pattern;

η represents the normalized diffracted wavefront coordinate, and is related to the coordinate y of the projected grating width D of the grating by

$$\eta = 2y/D,$$

where $D = W\cos\theta$ for an angle of diffraction θ and grating width W; the coordinate y lies in the region $-D/2$, $+D/2$;

$\Delta(\eta)$ represents the normalized deviation of the diffracted wavefront from a reference wavefront.

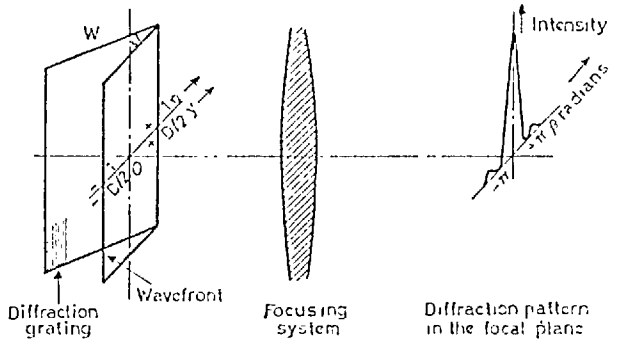

Figure 1. Illustration of some of the parameters used in the text.

Experimental observation of the diffracted wavefront can be made by using a Fizeau or Twyman–Green interferometer [3] adjusted so that the fringes produced by interference between the diffracted wavefront and a plane reference wavefront run perpendicular to the grating rulings. Any deviation $\Delta(\eta)$ will then produce a displacement of the fringe $\Delta(y)$ in a direction parallel to the rulings, and may be determined from the measured displacement according to the relation

$$\Delta(\eta) = \Delta(y) \times 2\pi/I,$$

where I is the fringe spacing as measured on the interferogram.

Computations of the diffraction pattern by measuring the deviation $\Delta(y)$ at a large number of points on the interferogram of the wavefront and using a Fourier transform computer programme lead to the diffraction pattern $A(\beta)$ as expressed in equation (1). Figure 2 show the result of the calculation of equation (1) for the particular case of the wavefront, shown in figure 3, from an Echelle grating. The abscissa relates to the particular properties of the instrument and grating considered Note that the ordinate is the square root of the intensity for clarity, i.e.

$$[A(\beta) . A^*(\beta)/4]^{1/2}.$$

If we let $\Delta(\eta)$ in equation (1) be a cosine function error of a single period across the wavefront we obtain the complete imperfect diffraction pattern by using the Fourier transform programme. Figures 4 to 7 give the result of the computations for the two wavelengths λ632·8 nm and λ316·4 nm when the amplitude of the periodic error is $\lambda/10$ at λ632·8 nm with the phase of the error, with respect to the

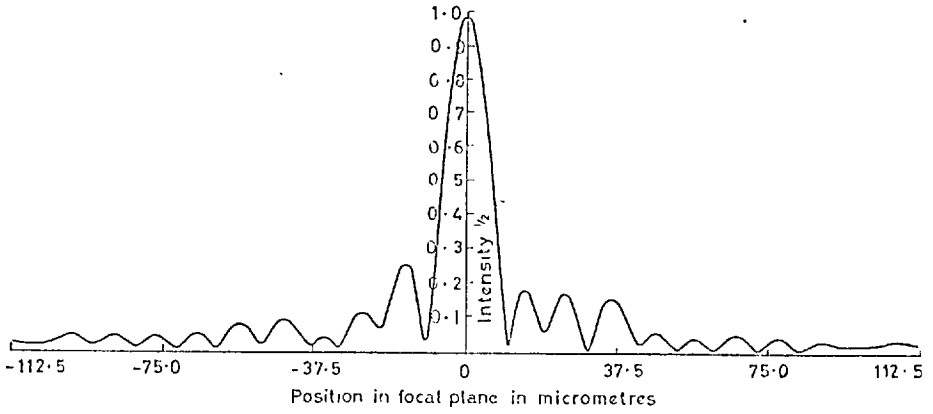

Figure 2. Diffraction pattern calculated by Fourier transform programme.

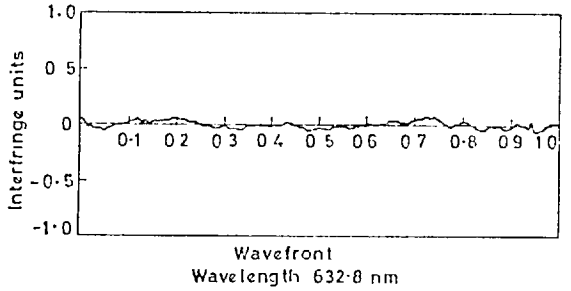

Figure 3. Wavefront from which figure 2 was obtained.

centre of the grating, either 0 or $\pi/2$. The figures show that symmetry is observed for $\phi=0$, asymmetry for $\phi=\pi/2$, and that decreases as well as increases in intensity can be obtained at shorter wavelengths. The abscissae in the figures refer to the same instrument and grating type as that of figure 2 and an ordinate value of 1·0 corresponds to the central peak intensity of a perfect grating.

We can now investigate this particular form of error by an extension of Stroke's analysis [4] of Rowland ghosts. Consider a wavefront with a single periodic error present. Let the amplitude of the error be Φ and its period be p, both in the η domain. We can express the deviation from a flat wavefront as a random component, R, and a periodic component by

$$\Delta(\eta)=R+\Phi\cos\left(\frac{2\pi}{p}\,.\,\eta+\phi\right), \tag{2}$$

where ϕ represents the phase of the periodic deviation of the wavefront. Stroke [4] has analysed equation (2) when $\phi=0$ and produces an analytical expression for the amplitude distribution in Rowland ghosts. We will follow a similar analysis for the above form of deviation.

Insertion of equation (2) into equation (1) leads to the term $\exp[i\Delta(\eta)]$ as follows:

$$\exp[i\Delta(\eta)]=\exp(iR)\,.\,\exp\left[i\Phi\,.\,\cos\left(\frac{2\pi}{p}\,.\,\eta+\phi\right)\right],$$

which reduces to [5]:

$$\exp(iR).\sum_{n=-\infty}^{+\infty} i^n.J_n(\Phi).\exp\left[i.n.\left(\frac{2\pi}{p}.\eta+\phi\right)\right],$$

where n is an integer and $J_n(\Phi)$ is the Bessel function of order n. The distribution of amplitude in the diffraction pattern is then given by equation (1):

$$A'(\beta)=\int_{\eta=-1}^{+1}\exp(i\beta\eta).\exp(iR).\sum_{n=-\infty}^{+\infty} i^nJ_n(\Phi).\exp\left[i.n.\left(\frac{2\pi}{p}.\eta+\phi\right)\right].d\eta.$$

The Bessel functions are given, if we neglect higher than cubic orders of Φ, by [6]:

$$J_0(\Phi)\simeq 1,\quad J_{+1}(\Phi)\simeq\Phi/2,\quad J_{-1}(\Phi)\simeq-\Phi/2,$$
$$J_{+2}(\Phi)\simeq\Phi^2/8,\quad J_{-2}(\Phi)\simeq\Phi^2/8.$$

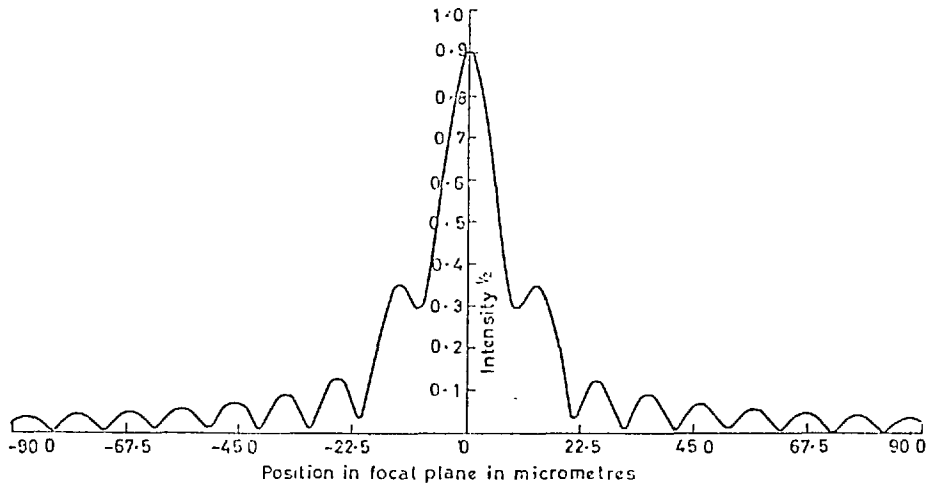

Figure 4. Diffraction pattern from a single cycle cosine wavefront of amplitude $\lambda/10$ at λ632·8 nm, observed at λ632·8 nm.

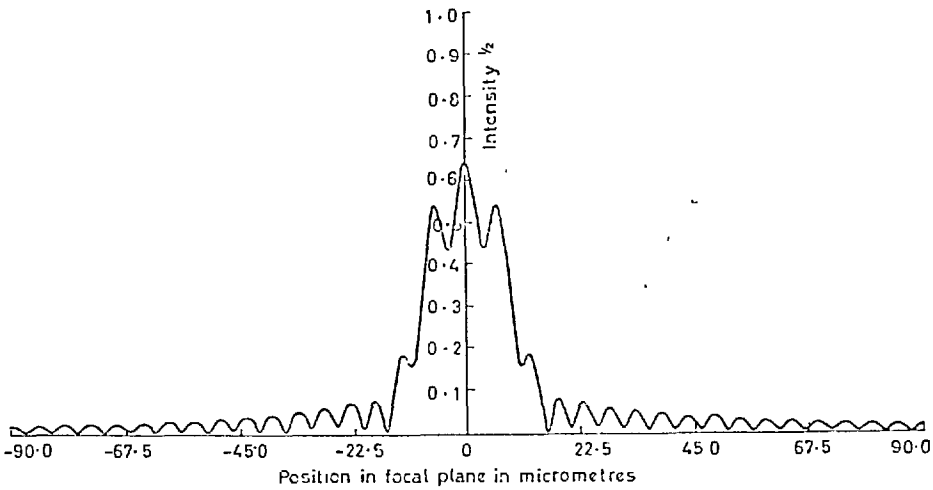

Figure 5. Diffraction pattern from a single cycle cosine wavefront of amplitude $\lambda/10$ at λ632·8 nm, observed at λ316·4 nm.

It is easily seen that this then gives rise to the amplitude:

$$A'(\beta) = A(\beta) + \frac{\Phi}{2} . i . \exp(i\phi) . A\left(\beta + \frac{2\pi}{p}\right) + \frac{\Phi}{2} . i . \exp(-i\phi) . A\left(\beta - \frac{2\pi}{p}\right) - \frac{\Phi^2}{8} . \exp(2 . i\phi) . A\left(\beta + 2 . \frac{2\pi}{p}\right) - \frac{\Phi^2}{8} . \exp(-2 . i\phi) . A\left(\beta - 2 . \frac{2\pi}{p}\right) + \ldots . \quad (3)$$

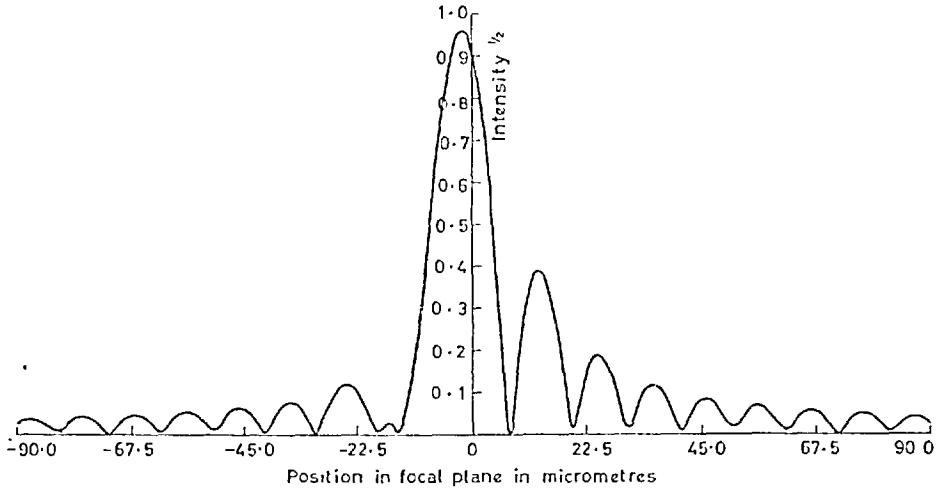

Figure 6. Diffraction pattern from a single cycle sine wavefront of amplitude $\lambda/10$ at $\lambda 632{\cdot}8$ nm, observed at $\lambda 632{\cdot}8$ nm.

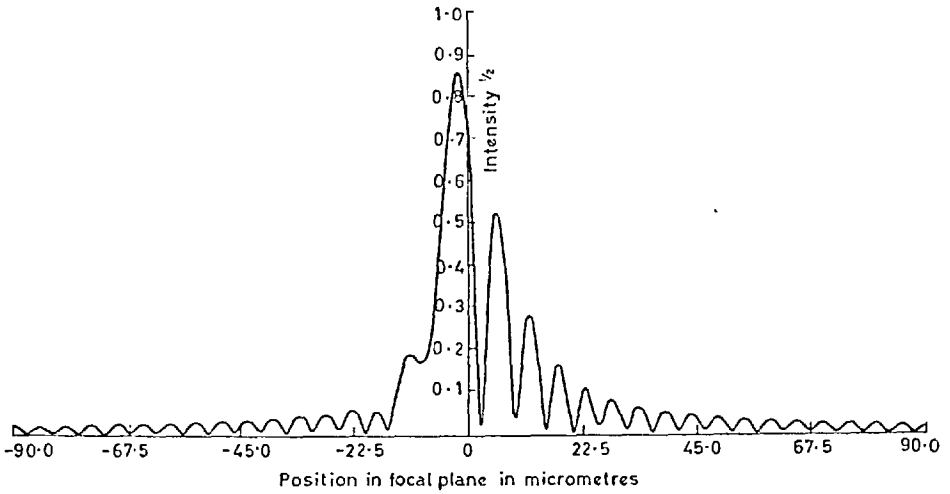

Figure 7. Diffraction pattern from a single cycle sine wavefront of amplitude $\lambda/10$ at $\lambda 632{\cdot}8$ nm, observed at $\lambda 316{\cdot}4$ nm.

The period p is usually extremely small for the case of Rowland ghosts and the terms of equation (3) can be considered separately, in which case their intensity is independent of ϕ, the phase. The usual Rowland ghost distribution of intensity consists of a central pattern given by the imperfections R and symmetrically placed either side of this is an exactly similar distribution at $\beta = \pm 2\pi/p$ but modified in intensity. A complete set of Rowland ghosts is obtained by considering higher orders of Φ, leading to replicas of the central diffraction pattern at multiples of $2\pi/p$.

However, when p is close to unity, that is when the period is comparable to the width of the grating, we must consider the interaction of the various terms in equation (3). It is for this reason that unless $\phi = 0$ we will have a certain asymmetry in the resulting intensity distribution about $\beta = 0$.

The agreement between Fourier transform calculations given earlier, for a single periodic error, and equation (3) has been shown to depend on the number of terms considered in equation (3).

3. Variation of amplitude of secondary maxima with wavelength

Stroke [4] shows that we can divide the amplitude $A(\beta_0)$ in the diffraction pattern, obtained by using the grating with random errors at a wavelength λ_0 and at an angle of diffraction i_0 (in autocollimation), into two components. These are the perfect diffraction grating and the imperfect grating terms, the latter dominating beyond the second minimum. If T represents the Fourier transform of the wavefront error $\Delta(\eta)$, then

$$A(\beta_0) \simeq 2 \cdot \frac{\sin \beta_0}{\beta_0} + i \cdot T[\Delta(\eta)_0].$$

Stroke goes on to show that observation at a different wavelength and angle of diffraction, λ and i respectively, gives rise to an amplitude distribution:

$$A(\beta) \simeq 2 \cdot \frac{\sin \beta}{\beta} + i \cdot \alpha \cdot T[\Delta(\eta)_0],$$

where α is given by:

$$\alpha^2 = \left(\frac{\lambda_0}{\lambda}\right)^2 \left(\frac{\sin i}{\sin i_0}\right)^2 \quad \text{for ruling errors,}$$

$$\alpha^2 = \left(\frac{\lambda_0}{\lambda}\right)^2 \left(\frac{\cos i}{\cos i_0}\right)^2 \quad \text{for blank errors.}$$

This means that in the regions where $T[\Delta(\eta)_0]$ dominates we can predict the variation of amplitude with wavelength. Hence we have the usual satellite intensity versus wavelength dependence law for random wavefront errors.

Variation of Rowland ghost intensities with wavelength is well known and seen from equation (3), when the period p is small, as being the result of the variation of Φ with wavelength. If Φ_0 represents the periodic amplitude for the case of λ_0 and i_0, than at λ and i we have:

$$\Phi = \Phi_0 \cdot \alpha.$$

Long period errors cannot be treated in the same way as Rowland ghosts because of the interaction of the amplitudes between subsidiary maxima, i.e. we cannot take the terms of equation (3) singly.

4. The case of a general phase and amplitude distribution in the wavefront

So far we have restricted ourselves to a single periodic error. We will now go on to consider the more general case of a wavefront which consists of any phase and amplitude distribution. But first we must establish the relation between symmetry in amplitude and intensity.

Let the amplitude A be expressed as:

$$A = A_S + A_A,$$

where A_S and A_A are the symmetrical and anti-symmetrical components of A. The intensity I is given by:

$$\begin{aligned} I &= AA^* \\ &= A_S A_S^* + A_S A_A^* + A_A A_S^* + A_A A_A^* \\ &= (A_S A_S^* + A_A A_A^*) \text{ which is always symmetrical} \\ &\quad + (A_S A_A^* + A_A A_S^*) \text{ which is always anti-symmetrical.} \end{aligned}$$

The special case of a symmetrical intensity distribution is obtained if A_S or $A_A = 0$, A_S is real and A_A imaginary, or A_S is imaginary and A_A is real.

Now let us look at the amplitude in the diffraction pattern obtained from the wavefront with a general phase and amplitude error:

$$\begin{aligned} A(\beta) &= \int_{\eta=-1}^{+1} \exp(i\beta\eta) \cdot \exp[i\Delta(\eta)] \cdot d\eta \\ &= \int_{\eta=-1}^{0} \exp(i\beta\eta) \cdot \exp[i\Delta(\eta)] \cdot d\eta + \int_{\eta=0}^{+1} \exp(i\beta\eta) \cdot \exp[i\Delta(\eta)] \cdot d\eta \\ &= \int_{\eta=0}^{+1} \exp(-i\beta\eta) \cdot \exp[i\Delta(-)] \cdot d\eta + \int_{\eta=0}^{+1} \exp(i\beta\eta) \cdot \exp[i\Delta(+)] \cdot d\eta, \end{aligned}$$

where $\Delta(-)$ is the value of $\Delta(\eta)$ at $-\eta$, $\Delta(+)$ is the value of $\Delta(\eta)$ at $+\eta$.

Assuming we have a smooth wavefront without random errors then $R = 0$ and we can write Δ as Δ_s and Δ_a where Δ_s is symmetrical about $\eta = 0$ and Δ_a is anti-symmetrical. Thus:

$$\begin{aligned} \Delta(+) &= \Delta_s + \Delta_a, \\ \Delta(-) &= \Delta_s - \Delta_a. \end{aligned}$$

The amplitude becomes:

$$\begin{aligned} A(\beta) &= \int_{\eta=0}^{+1} \exp(i\beta\eta) \cdot \exp(i\Delta_s) \cdot \exp(i\Delta_a) \cdot d\eta \\ &\quad + \int_{\eta=0}^{+1} \exp(-i\beta\eta) \cdot \exp(i\Delta_s) \cdot \exp(-i\Delta_a) \cdot d\eta \\ &= 2\int_{\eta=0}^{+1} \cos\beta\eta \cdot \exp(i\Delta_s) \cdot \cos\Delta_a \cdot d\eta \\ &\quad + 2\int_{\eta=0}^{+1} \sin\beta\eta \cdot \exp(i\Delta_s) \cdot \sin\Delta_a \cdot d\eta. \end{aligned} \tag{4}$$

Examination of equation (4) shows that the first term is symmetrical about $\beta = 0$ since $\cos\beta\eta$ is symmetrical and the second term is anti-symmetrical.

There are three forms of wavefront error possible:

(1) symmetrical where $\Delta_a = 0$;

(2) anti-symmetrical where $\Delta_s = 0$;

(3) asymmetrical where $\Delta_s \neq 0$, $\Delta_a \neq 0$.

Using the previous relation between symmetry in amplitude and intensity we may conclude from equation (4) that the above three cases give

(1) symmetrical diffraction pattern occurs when $\Delta_a = 0$;

(2) an anti-symmetrical grating error gives rise to an amplitude distribution consisting of the sum of symmetrical and anti-symmetrical terms which is an asymmetrical intensity distribution. An exception to this would be that of $\Delta_a = \pi/2$ where we would obtain a symmetrical intensity distribution;

(3) an asymmetrical grating error gives rise to an asymmetrical diffraction pattern.

5. Influence of periodic errors on the width and shift of line profiles

In order to obtain a quantitative idea of the width and shift of line profiles, as a result of long period errors, a number of computations, using the Fourier transform programme, were performed for the case of odd periodic errors of various amplitudes and periods, the results of which are shown in the table. There is apparent a definite relation between shift and period which we shall examine in more detail.

Width and shift (in radians) of the line profile measured in the angular coordinate, β, of the diffraction pattern for odd periodic errors of various amplitudes and numbers of cycles in the periodic error across the grating. All results relate to $\lambda 632{\cdot}8$ nm

Number of cycles in periodic error	Amplitude of periodic error							
	$\lambda/10$		$\lambda/20$		$\lambda/40$		$\lambda/80$	
	Width	Shift	Width	Shift	Width	Shift	Width	Shift
1	2·85	−0·63	2·79	−0·32	2·79	−0·16	2·79	−0·08
2	2·73	−0·28	2·78	−0·13	2·78	−0·07	2·78	−0·03
3	2·76	−0·14	2·78	−0·06	2·78	−0·04	2·78	−0·02

Half-height width for a perfect grating is 2·78

Considering the expression for the amplitude resulting from a single periodic error, given by equation (3), we see that the majority of any asymmetry of the central maximum in the diffraction pattern will result from the first subsidiary maxima at $\beta = \pm 2\pi/p$. Let us examine equation (3) by replacing $2\pi/p$ by χ and putting $R = 0$:

$$A(\beta) = \frac{\sin\beta}{\beta}\,; \quad A(\beta \pm \chi) = \frac{\sin(\beta \pm \chi)}{\beta \pm \chi}.$$

The resulting amplitude is expressed as:

$$A'(\beta)=\frac{\sin\beta}{\beta}+i\,.\,\frac{\Phi}{\beta^2-\chi^2}\,.\,(\beta\sin\beta\cos\chi-\chi\cos\beta\sin\chi)\,.\,\cos\phi$$
$$-\frac{\Phi}{\beta^2-\chi^2}\,.\,(\beta\cos\beta\sin\chi-\chi\sin\beta\cos\chi)\,.\,\sin\phi.$$

The first two terms are symmetrical and the last anti-symmetrical about $\beta=0$. Hence using the previous relation between intensity and amplitude we see the symmetrical part of the intensity is given by:

$$I_S=\frac{\sin^2\beta}{\beta^2}+\frac{\Phi^2}{(\beta^2-\chi^2)^2}(\beta\sin\beta\cos\chi-\chi\cos\beta\sin\chi)^2\cos^2\phi$$
$$+\frac{\Phi^2}{(\beta^2-\chi^2)^2}(\beta\cos\beta\sin\chi-\chi\sin\beta\cos\chi)^2\sin^2\phi,$$

and the anti-symmetrical part is:

$$I_A=-2\,.\,\frac{\sin\beta}{\beta}\,.\,\frac{\Phi}{\beta^2-\chi^2}\,.\,(\beta\cos\beta\sin\chi-\chi\sin\beta\cos\chi)\,.\,\sin\phi. \qquad (5)$$

Equation (5) leads to the following results:

(1) The anti-symmetrical term is proportional to the amplitude of the periodic error, and therefore inversely proportional to wavelength.

(2) If χ is large, i.e. p small, and β is small we have $\chi^2\gg\beta^2$ and $\sin\chi/\chi$ is small which means:

$$I_A\simeq-2\,.\,\frac{\sin^2\beta}{\beta^2}\,.\,\Phi\,.\,\beta\,.\,\frac{\cos\chi}{\chi}\,.\,\sin\phi\propto\frac{\cos\chi}{\chi}\,.$$

There is an inverse dependence on χ which shows the asymmetry will fall off as the number of periods in the wavefront increases. This confirms the small amount of line profile asymmetry expected from Rowland ghosts.

(3) If χ is small, i.e. $\ll\pi$, corresponding to p large, then

$$I_A\simeq-2\,.\,\frac{\sin\beta\,.\,\cos\beta}{\beta^2}\,.\,\Phi\,.\,\chi\,.\,\sin\phi\propto\chi.$$

Again the asymmetry would fall off as the wavefront becomes flat.

(4) Maximum anti-symmetry is in the region $\beta=\pi$.

The table confirms the above predictions for the special case of an odd wavefront. The shift of the point midway between the half maximum intensity points on the line profile from that of a perfect profile is used as an approximate measure of the asymmetry. Variation of this shift with wavelength is predicted mainly by the variation of Φ, as shown in (1), when we neglect higher order terms in equation (3), and variation with period is given by (2).

6. Reducing the asymmetry in the line profile

When observing line profiles with a grating instrument where the resolution is grating limited, the type of errors described become extremely important. By masking a grating in the correct manner it should be possible to produce a symmetrical profile from a previously asymmetrical one. The required amount of

masking would be such as to make $\phi = 0$ in equation (5). This would lower the resolving power but may be worthwhile in terms of the resulting profile. However, we are assuming that any asymmetry is a result of a single periodic component. The importance of the masking lies in the fact that an asymmetrical profile alters its asymmetry on changing the wavelength at which we observe, whereas a symmetrical profile stays symmetrical on change of wavelength.

7. Conclusion

Periodic errors whose periods are similar in magnitude to the width of the grating are shown to be particularly harmful near the centre of the diffraction pattern.

The overall diffraction pattern is found to be symmetrical for an even wavefront error and consists of a combination of symmetrical and anti-symmetrical distributions for an odd wavefront error. Because of the interaction of subsidiary maxima, it is not possible to predict overall wavelength versus intensity relations for the subsidiary maxima. This sort of error means that the intensity of satellites obtained close to the central diffraction maxima may not always vary according to the usual square of the wavelength ratio law.

The symmetry of the central maxima has been shown to be susceptible to these periodic errors and the dependence of the asymmetry found, for the case of a single periodic error, for variation of wavelength and number of cycles in the wavefront.

Masking of the grating can be used in an attempt to reduce the degree of asymmetry resulting from these sorts of error. The importance of a symmetrical line profile, especially in the vacuum ultra-violet wavelength region, often outweighs the attainment of the extra resolving power gained by the use of the full grating width.

Acknowledgments

The author wishes to thank Dr. A. H. Cook for the considerable interest he has taken during the course of this work and for the suggestion of a simplified approach for dealing with general phase and amplitude distribution errors and shifts of the line profile. I am also grateful for comments and suggestions made by Mr. E. J. Gillham, Dr. G. H. C. Freeman and Dr. W. R. C. Rowley.

The work described above has been carried out at the National Physical Laboratory.

On examine numériquement et analytiquement l'effet des défauts de faible fréquence spatiale des réseaux de diffraction.

On montre que de tels défauts peuvent produire des figures de diffraction dans lesquelles les intensités des maxima secondaires n'obéissent pas à une loi simple de variation avec la longueur d'onde à cause de l'interaction des ghosts de Rowland qui sont près du maximum central. Toutefois, le déplacement du profil de raie suit une loi de variation simple sous certaines hypothèses. Typiquement, le déplacement, pour un défaut d'un cycle d'amplitude $\lambda/80$ dans la surface d'onde, serait d'environ $3\frac{1}{2}$ pour cent de la longueur à mi-intensité. Les résultats généraux obtenus pour une distribution quelconque de la phase dans la surface d'onde conduisent à la conclusion qu'une figure de diffraction symétrique peut être obtenue uniquement à partir d'une surface d'onde symétrique et non, en général, à partir d'une surface d'onde antisymétrique.

In der Arbeit wird der Einfluss von Fehlern bei Beugungsgittern niedriger Ortsfrequenz numerisch und analytisch untersucht.

Solche Fehler können Beugungsmuster erzeugen, bei denen die Intensitäten der zusätzlichen Maxima kein einfaches Gesetz der Wellenlängenänderung befolgen, weil die nahe dem zentralen Maximum liegenden Rowlandschen Geister mitwirken. Indessen gehorcht die Verschiebung des Linienprofils unter bestimmten Annahmen einem einfachen Änderungsgesetz. So beträgt für einen einzelnen Periodenfehler mit der Amplitude $\lambda/80$ in der Wellenfläche die Verschiebung ungefähr $3\frac{1}{2}$ Prozent der Halbwertsbreite. Die allgemeinen Ergebnisse für eine beliebige Phasenverteilung in der Wellenfläche führen zu dem Schluss, dass ein symmetrisches Beugungsbild nur aus einer symmetrischen Wellenfläche herstammen kann und nicht, wenigstens im allgemeinen, von einer antisymmetrischen.

References

[1] Lyman, T., 1901, *Phys. Rev.*, **12**, 1; 1903, *Ibid.*, **16**, 257. Ingelstam, E., and Djurle, E., 1953, *J. opt. Soc. Am.*, **43**, 572. Finkelstein, N. A., Brumley, C. H., and Meltzer, R. J., 1952, *J. opt. Soc. Am.*, **42**, 121. Sparrow, C. M., 1919, *Astrophys. J.*, **49**, 65. Peirce, C. S., 1879, *Am. J. Math.*, **2**, 330.

[2] Rowland, H. A., 1893, *Phil. Mag.*, **35**, 397. Michelson, A. A., 1927, *Studies in Optics* (Chicago: University Press); 1903, *Astrophys. J.*, **18**, 278.

[3] Stroke, G. W., 1960, *Rev. d'Optique*, **39**, 291. Mallia, E. A., 1967, *Solar Phys.*, **2**, 360.

[4] Stroke, G. W., 1967, *Handbuch der Physik*, **29**, edited by S. Flügge (Berlin: Springer-Verlag), p. 426.

[5] Whittaker, E. T., and Watson, G. N., 1965, *Modern Analysis* (Cambridge: University Press), p. 357.

[6] Whittaker, E. T., and Watson, G. N., 1965, *Modern Analysis* (Cambridge: University Press), p. 355.

Reduction of residual coma and astigmatism in a 1·5 m Czerny–Turner spectrometer

R C Preston
Division of Quantum Metrology, National Physical Laboratory, Teddington, Middlesex
MS *received 20 March 1970, in revised form 14 May 1970*

Abstract Ray tracing calculations have been performed in order to evaluate the geometrical aberrations of a high resolution 1·5 m in-plane Czerny–Turner spectrometer using spherical mirrors and a high blaze angle Echelle grating. Results show that for minimum instrumental broadening the focusing mirror off-axis angle must satisfy the Rosendahl $\cos^3$ relation, that the astigmatism can be reduced by using divergent grating illumination, and that circular slits can still be used to eliminate the inherent spectral line curvature.

1 Introduction

Recently (Eggers and Peterson 1969, Hill 1969), the use of off-axis paraboloidal mirrors has been considered as a means of producing parallel illumination for plane diffraction gratings

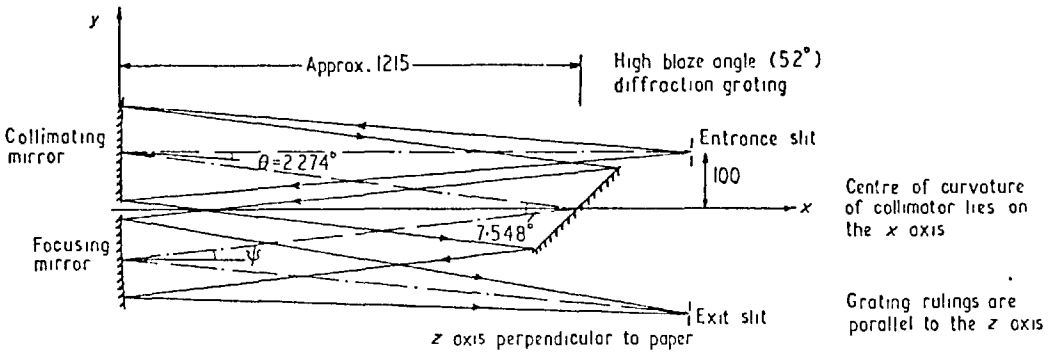

Figure 1 Schematic arrangement of the 1·5 m spectrometer showing the main design parameters. Collimating mirror aperture 110 wide × 102 high, defined by the grating. Both mirrors are spherical and 3·0 m radius of curvature. Dimensions in millimetres

and the results show that very good image quality can be obtained with certain configurations. However, the increased cost, manufacturing time and alignment problems as compared with spherical mirrors are a severe limitation to their use. The instrument which is at present being constructed at NPL is a 1·5 m in-plane Czerny–Turner spectrometer to be used in the vacuum ultraviolet, where the theoretical resolution of the grating is unlikely to be realized. This leads us to consider whether, with a system using spherical mirrors, geometrical aberrations can be reduced to a tolerable level, compatible with the resolution and dispersion of the Echelle grating to be used. Ray tracing calculations outlined here were carried out to minimize the geometrical aberrations, whilst retaining spectral purity for finite slit lengths.

2 Ray tracing results

The various parameters of the spectrometer to be considered are shown in figure 1. In order to obtain an approximately flat focal plane (Mielenz 1964), the grating is placed at the non-critical distance of 1215 mm from the two spherical mirrors. To minimize the off-axis angle θ the entrance slit is placed as close as possible to the grating in the y direction, giving a value for θ of 2·274°. The collimator aperture of 110 mm wide × 102 mm high is defined by the size of the 52° blaze, 309 lines per millimetre, Echelle to be used. The angle between incident and diffracted beams of 7·548° is the minimum allowed by a reasonable separation of the mirrors. For a wavelength of λ 150 0 nm the blaze properties of the grating are most nearly satisfied for the 34th order, corresponding to angles of incidence and diffraction of 48·285° and 55·833° respectively. The factors left to be optimized are the off-axis angle (ψ) of the focusing mirror in order to reduce the residual coma arising from the high blaze angle grating, the entrance slit-to-collimator distance in order to reduce astigmatism, and the form of curved slits necessary to produce maximum spectral purity. All calculations refer to λ 150 0 nm but are obviously applicable to other wavelengths since very similar angles of incidence and diffraction can be obtained by choice of the correct order.

With the entrance slit at the tangential astigmatic focus of the collimator various ray tracings were performed in order to reduce the residual coma in the image, due to the incident and diffracted beams from the grating being of unequal width, by optimizing the off-axis angle ψ of the focusing mirror. A summary of the results for an object point at the centre of the entrance slit is shown in figure 2, which shows the variation with ψ of the three image width evaluation parameters defined in the figure. The three curves show a minimum which approximately corresponds to the value calculated using the Rosendahl $\cos^3$ relation (Rosendahl 1962, Shafer *et al.* 1964) which substantiates the results given in recent papers by Rouse *et al.* (1969) and Reader (1969). Analysis for object points other than at the slit centre has been performed in order to investigate the inherent spectral line curvature in such a system (Fastie 1952, Kudo 1965, Minkowski 1942, Rupert 1952, Stroke 1967). It was expected that this would be the same as that of an Ebert spectrometer (where $\theta=\psi=2{\cdot}274°$ and the two mirrors are concentric), since the basic collimator, grating and entrance slit arrangement is the same. This has been confirmed, and it is concluded that circular slits of 100 mm radius of curvature provide best compensation for spectral line curvature due to the grating, but do not wholly compensate for the long astigmatic image.

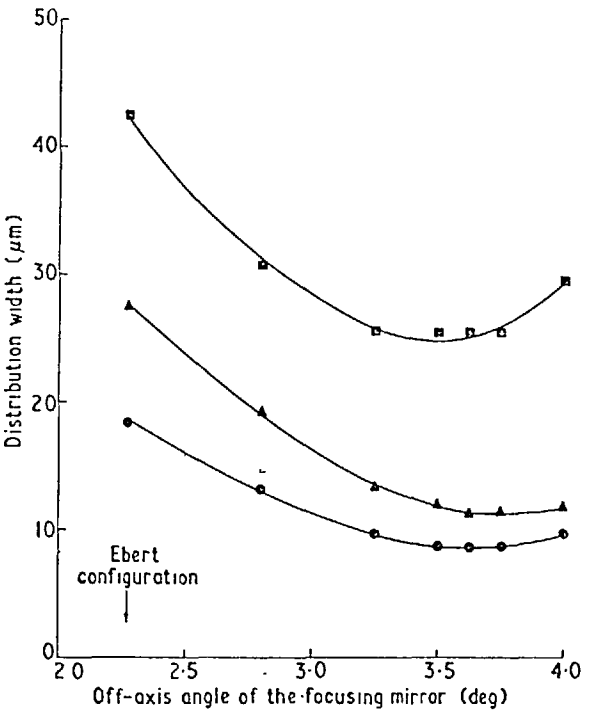

Figure 2 Plot of the image distribution width against the off-axis angle of the focusing mirror for an object point at the centre of the entrance slit. ⊡ extreme width of the image distribution; ▲ width of image distribution at $z=0$; ⊙ width corresponding to twice the rms deviation from the centre of gravity of the distribution

For $\psi = 3{\cdot}5°$, the extreme width of the image distribution for object points at the ends of a 10 mm long circular entrance slit is 33 μm as compared with 26 μm which, as can be seen from figure 2, is the extreme width for an object point at the centre of the entrance slit.

Bates *et al.* (1970) show that a slight defocusing of the entrance slit and refocusing at the exit slit leads to a balancing of the mirror astigmatism by that introduced by the grating when illuminated in divergent light, and calculations have been made to try to minimize astigmatism by this means. The best results have been obtained by putting the entrance slit 19 mm closer to the collimating mirror and moving the exit slit 24 mm away from the focusing mirror. This reduced the astigmatic image length from 550 μm to a negligible 50μm with only about 6% loss in spectral resolution for the object point at the centre of the entrance slit. The image distribution for object points at the ends of a 10 mm long circular entrance slit also became more symmetrical. Bates *et al.* (1970) also show that, provided the grating width is not too large, the additional coma introduced by the grating is small when illuminated by a slightly divergent beam. This has been shown to be the case for this particular instrument, and the results of the optimization process described earlier, for reducing residual coma, are not significantly altered by using divergent grating illumination. Although astigmatism has been considerably reduced it is still necessary to use 100 mm radius of curvature slits (or a straight entrance slit with a specially curved exit slit) to compensate for the inherent spectral line curvature due to the grating in order to obtain spectral purity.

3 Conclusion

The performance of a 1·5 m asymmetrical Czerny–Turner spectrometer using spherical mirrors and a high blaze angle grating has been investigated by the use of geometrical optics ray tracing, and steps have been taken to minimize the major aberrations. Residual coma has been shown to be reduced by optimizing the focusing mirror off-axis angle, astigmatism is reduced by illuminating the grating in a slightly divergent beam, and circular slits have been shown to satisfy the inherent spectral line curvature.

Finally, it is useful to consider the expected performance of the spectrometer optimized in this way. An indication of its instrumental resolution is given by twice the root mean square deviation of the optimized distribution. With a linear dispersion of 0·036 nm mm^{-1} this parameter corresponds to a spectral width of 0·0004 nm, at the central slit point, for a wavelength of λ 150·0 nm.

Acknowledgments

This work forms part of the research programme of the National Physical Laboratory.

References

Bates B McDowell M and Newton A C 1970 *J. Phys.* E: *Sci. Instrum.* 3 206–10

Eggers D F and Peterson M A 1969 *Appl. Optics* 8 589–92

Fastie W G 1952 *J. Opt. Soc. Am.* 42 641–7, 647–51

Hill R A 1969 *Appl. Optics* 8 575–81

Kudo K 1965 *J. Opt. Soc. Am.* 55 150–61

Mielenz K D 1964 *J. Res. Nat. Bur. Stand. C* 68 205–13

Minkowski R 1942 *Astrophys. J.* 96 306–8

Reader J 1969 *J. Opt. Soc. Am.* 59 1189–96

Rosendahl G R 1962 *J. Opt. Soc. Am.* 52 412–5

Rouse P E Brixner B and Kline J V 1969 *J. Opt. Soc. Am.* 59 955–60

Rupert C S 1952 *J. Opt. Soc. Am.* 42 779–81

Shafer A B Megill L R and Droppleman L 1964 *J. Opt. Soc. Am.* 54 879–87

Stroke G W 1967 *Handb. Phys.* 29 469 (Berlin: Springer)

Journal of Physics E: Scientific Instruments 1970 Volume 3
Printed in Great Britain

Qu.13

September 1970

N A T I O N A L P H Y S I C A L L A B O R A T O R Y

RAY-TRACING FOR A TWO-MIRROR SPECTROMETER AND OPTIMISATION OF A 1.5 m CZERNY-TURNER INSTRUMENT

by

R.C. Preston

DIVISION OF QUANTUM METROLOGY

Abstract

A system of ray tracing equations is given which enables the distribution of intensity in the focal plane of a two spherical mirror spectrometer to be calculated. Using these equations in a computer program the particular properties of a 1.5 m Czerny-Turner spectrometer, using a high blaze angle Echelle grating, have been evaluated. The results show that the focussing mirror off-axis angle must satisfy the Rosendahl $\cos^3$ relation in order to minimise residual coma and that a stigmatic system is obtained, at a marginal loss in spectral resolution, when a slightly divergent beam is incident upon the grating. Curved slits are also investigated in order to retain as much spectral purity as possible.

Introduction

Evaluation of the image quality of a Czerny-Turner spectrometer, assuming a perfect diffraction grating, can most easily be accomplished using geometrical optics ray tracing and letting each ray satisfy the grating equation when it hits the grating.

The instrument being constructed at NPL is for use in the vacuum ultra-violet wavelength region where wavefront aberrations from the grating are expected to be relatively large in comparison with the wavelength. Under these conditions an indication of the aberrations presented by the mirrors when using a perfect grating is of considerable interest.

Results of ray tracing calculations for general or specific instruments have been given by Brahde (ref. 1), Yoshinaga et al. (ref. 2), Shafer et al. (ref. 3), Chandler (ref. 4), Eggers and Peterson (ref. 5), Hill (ref. 6), Rouse et al. (ref. 7) and Reader (ref. 8). This report will give general equations for the evaluation of aberrations and apply them to a specific 1.5 m instrument using a high blaze angle Echelle grating with the view to optimising the spectral quality attainable.

Ray tracing equations

The ray trace is a simple geometrical approach which uses equations similar to those given by Brahde (ref. 1) for the treatment of the spherical mirrors and where possible similar terminology has been used. Diffraction by a high blaze angle grating is considered and a rectangular grid of rays incident on the collimator used.

Figure 1 shows the general layout of the two mirror system of the Czerny-Turner form where the centres of all the optical components including the centres of curvature of the mirrors lie in the x-y plane. The slits and grating rulings are parallel to the z axis so that dispersion takes place in the x-y plane. Figure 2 shows more detail of the entrance slit-collimator arrangement. Ray I is shown originating at the slit point (f, p, q) defined with respect to a co-ordinate system, denoted by the subscript 1, centred on the vertex of the collimator, of radius of curvature r1, with the x axis pointing towards the centre of curvature. The angle, θ, between the ray from the entrance slit point (f, p0, 0) to the vertex of the collimator and the x_1 axis defines the off-axis angle of the collimator. Thus p0 is defined as the y_1 co-ordinate of the entrance slit such that a ray from the centre of the slit hitting the collimator vertex will also hit the centre of the grating as shown in Figure 1. There is the following relation between p0, f and θ:-

$$\frac{p0}{f} = \tan\theta. \qquad \ldots (1)$$

Now f defines the distance in the x_1 direction of the entrance slit from the collimator which for parallel illumination of the grating would correspond to the tangential astigmatic focus and:-

$$f = \frac{r1.\cos^2\theta}{2}. \qquad \ldots (2)$$

For parallel illumination of the grating equations (1) and (2) serve to eliminate θ whereas if we wish to consider other types of illumination equation (1) is used with $p0$ and f as independent variables. In the present program equation (2) is not used.

Let ray I hit the collimator at $(x0, y0, z0)$ from which it is reflected as ray II towards the grating. A complete set of rays representing a realistic collimator illumination is obtained by dividing up the collimator surface into rectangular areas each representing one ray. A rectangular grid totalling 256 rays in a 16 × 16 array is used here. If the overall width and height of the aperture are w and h respectively then the y-z co-ordinates of the point of impact for ray I on the collimator become:-

$$\begin{aligned} y0 &= w.(2m - 17)/32, \\ z0 &= h.(2n - 17)/32, \end{aligned} \qquad \ldots (3)$$

where m and n are integers taking the values from 1 to 16.

Thus the $(y0, z0)$ co-ordinates of the point of impact represent the centres of small rectangular areas all the same size and therefore each ray represents equal intensity weight in the focal plane. The x_1 co-ordinate is defined by the surface of the mirror and is given by:-

$$x0 = r1 - (r1^2 - y0^2 - z0^2)^{\frac{1}{2}}. \qquad \ldots (4)$$

In fact we see that each ray does not quite represent equal intensity weight due to the curvature of the mirror surface, but this is negligible in practice. The reason for using a rectangular grid is that a rectangular diffraction grating is used and it is the latter which is the effective aperture stop in the system and defines the values of h and w.

Different object points on the entrance slit are considered by scanning the variable q in suitable intervals.

The direction cosines of ray II are easily calculated as:-

$$\lambda = 2k.(1 - f/r1 + b - b.x0/r1),$$

$$\mu = -2k.(p/r1 + b.y0/r1),$$

$$\nu = -2k.(q/r1 + b.z0/r1), \qquad \ldots (5)$$

where $$b = -1 + 2.x0/r1 + 2.f/r1 - 2.f.x0/r1^2 - 2.p.y0/r1^2 - 2.q.z0/r1^2,$$

$$k = 1/2.\left(b + \frac{(r1 - f)^2 + p^2 + q^2}{r1^2}\right)^{\frac{1}{2}}.$$

Rotation of the co-ordinate system about the z_1 axis by $-\theta$ is now performed such that the new x axis points to the centre of the grating as shown in Figures 1 and 2. The new co-ordinate system is denoted by a subscript 2 and has the grating at $(d1, 0, 0)$. At this point it should be noted that these calculations refer to a beam limited only by the aperture of the grating. In practice the mirrors may be masked in which case it is possible for a small amount of vignetting to occur for extreme rays. This is neglected here and we note that if this occurs it will be of advantage because the vignetting will be of the most aberrated rays.

The direction cosines of ray II now become $(f1, g1, h1)$ where:-

$$f1 = (f.\lambda - p0.\mu)/(f^2 + p0^2)^{\frac{1}{2}},$$

$$g1 = (f.\mu + p0.\lambda)/(f^2 + p0^2)^{\frac{1}{2}},$$

$$h1 = \nu. \qquad \ldots (6)$$

By a similar transformation the position that ray II leaves the collimator $(x1, y1, z1)$ becomes:-

$$x1 = (x0 - y0.p0/f)/pf,$$

$$y1 = (y0 - x0.p0/f)/pf,$$

$$z1 = z0, \qquad \ldots (7)$$

where $pf = (1 + p0^2/f^2)^{\frac{1}{2}}$.

Let ray II hit the grating at $(xg1, yg1, zg1)$ in the present co-ordinate system and let the grating normal make an angle γ with the x_2 axis (this being the angle of incidence for a non-aberrated ray) and the diffracted ray be observed at an angle β as shown in Figure 3. Now β is fixed by design considerations, γ is such that the grating blaze properties are most nearly satisfied as discussed later. The co-ordinates of intersection of ray II and the grating become:-

$$\begin{aligned} xg1 &= (g1.\tan\gamma.x1 - f1.\tan\gamma.y1 - f1.d1)/(g1.\tan\gamma - f1), \\ yg1 &= (xg1 - d1)/\tan\gamma, \\ zg1 &= (xg1 - x1).h1/f1 + z1. \end{aligned} \qquad \ldots (8)$$

Using the grating equation and two extra transformations we can find the direction cosines of the diffracted ray III.

In the subscript 2 co-ordinate system the direction cosines of ray II when it hits the grating are - (f1, g1, h1). Rotation of the subscript 2 co-ordinate system about the z axis by $180^\circ - \gamma$, after first translating the system by d1 in the x_2 direction, leads to the transformed direction cosines (f2, g2, h2) of ray II, in the co-ordinate system denoted by subscript 3, of:-

$$\begin{aligned} f2 &= f1.\cos\gamma - g1.\sin\gamma, \\ g2 &= f1.\sin\gamma + g1.\cos\gamma, \\ h2 &= - h1. \end{aligned} \qquad \ldots (9)$$

For a particular wavelength λ, and order n with a grating whose spacing constant is d, the direction cosines (f3, g3, h3) of ray III become, by application of the grating equation:-

$$\begin{aligned} h3 &= - h2, \\ g3 &= n.\lambda/d - g2, \\ f3 &= (1 - g3^2 - h3^2)^{\frac{1}{2}}. \end{aligned} \qquad \ldots (10)$$

Rotation of the co-ordinate system about the z_3 axis by $\gamma+\beta$ leads to the x_4 axis pointing towards the vertex of the focussing mirror and the direction cosines $(f4, g4, h4)$ of ray III become, in the co-ordinate system denoted by a subscript 4:-

$$\begin{aligned} f4 &= f3.\cos(\gamma+\beta) + g3.\sin(\gamma+\beta), \\ g4 &= -f3.\sin(\gamma+\beta) + g3.\cos(\gamma+\beta), \\ h4 &= h3. \end{aligned} \qquad \ldots (11)$$

The position at which ray III left the grating is seen by a direct single transformation of $(xg1, yg1, zg1)$, in the subscript 2 system, about the z axis by β to give, in the subscript 4 system, the co-ordinates $(xg4, yg4, zg4)$ as:-

$$\begin{aligned} xg4 &= (d1 - xg1).\cos\beta - yg1.\sin\beta, \\ yg4 &= -(d1 - xg1).\sin\beta - yg1.\cos\beta, \\ zg4 &= zg1. \end{aligned} \qquad \ldots (12)$$

If the focussing mirror has a radius of curvature $r2$ and off-axis angle ψ then we can show that the position on the focussing mirror surface at which ray III hits is $(x2, y2, z2)$ where:-

$$\begin{aligned} y2 &= yg4 - g4.gt + g4.(gt^2 - ht - xg4^2 - yg4^2 - zg4^2)^{\frac{1}{2}}, \\ z2 &= zg4 - h4.gt + h4.(gt^2 - ht - xg4^2 - yg4^2 - zg4^2)^{\frac{1}{2}}, \\ d2 - x2 &= r2.\cos\psi - (r2^2.\cos^2\psi - y2^2 - z2^2 + 2.r2.y2.\sin\psi)^{\frac{1}{2}}, \end{aligned} \qquad \ldots (13)$$

where $gt = f4.(xg4 + r2.\cos\psi - d2) + g4.(yg4 - r2.\sin\psi) + h4.xg4,$

$ht = d2^2 - 2.d2.(xg4 + r2.\cos\psi) + 2.xg4.r2.\cos\psi - 2.yg4.r2.\sin\psi.$

Here $d2$ is the distance from the grating centre to the vertex of the focussing mirror.

A final co-ordinate transformation, to produce a system centred on the focussing mirror vertex with the x axis pointing in the direction of the

centre of curvature, is performed. This represents a linear transformation of d2 in the x_4 direction and then a rotation through $180^\circ - \psi$ about the z axis. The direction cosines (ρ, σ, τ) of ray III in the co-ordinate system with subscript 5 in Figure 1 become:-

$$\begin{aligned} \rho &= f4.\cos\psi - g4.\sin\psi, \\ \sigma &= f4.\sin\psi + g4.\cos\psi, \\ \tau &= -h4. \end{aligned} \qquad \ldots (14)$$

The point (x3, y3, z3) at which ray III falls on the focussing mirror becomes:-

$$\begin{aligned} x3 &= (d2 - x2).\cos\psi + y2.\sin\psi, \\ y3 &= (d2 - x2).\sin\psi - y2.\cos\psi, \\ z3 &= z2. \end{aligned} \qquad \ldots (15)$$

Reflection at the focussing mirror produces ray IV which has direction cosines given by (a, b, c) where:-

$$\begin{aligned} a &= -\rho + 2.qf.(x3 - r2)/r2, \\ b &= -\sigma + 2.qf.y3/r2, \\ c &= -\tau + 2.qf.z3/r2, \end{aligned} \qquad \ldots (16)$$

where $qf = \left[\rho.(x3 - r2) + \sigma.y3 + \tau.z3\right]/r2.$

If (x4, y4, z4) represents an arbitrary point on the reflected ray IV then we have:-

$$\begin{aligned} y4 &= y3 + \frac{b}{a}.(x4 - x3), \\ z4 &= z3 + \frac{c}{a}.(x4 - x3). \end{aligned} \qquad \ldots (17)$$

If x4 is the distance from the focussing mirror vertex to the focal plane then the equations (17) define the co-ordinates of the intersection of ray IV in the focal plane.

In practice, where slits are used in the spectrometer one focusses the exit slit to produce a minimum observed half-height width in the y direction (parallel to the direction of dispersion). Thus if the difference between the focal plane y co-ordinates for the ray from an object point at the centre of the entrance slit to the collimator vertex, traced through the system, and all other rays is found then we can perform a least squares determination to obtain the best focus. Let the central ray be denoted by the subscript 0 and let ky be close to unity then as the focal plane is close to r2/2 from the focussing mirror:-

$$x4 = ky.r2/2$$

and therefore:-

$$y4_0 = y3_0 + \frac{b_0}{a_0}.(ky.r2/2 - x3_0).$$

Now the aberration in the y direction is $y4 - y4_0$ thus we can show by least squares method that the best value of ky is given by:-

$$ky.r2/2 = \frac{-\sum_{\substack{\text{all}\\\text{rays}}} \left[y3 - y3_0 - \frac{b}{a}.x3 + \frac{b_0}{a_0}.x3_0\right].\left[\frac{b}{a} - \frac{b_0}{a_0}\right]}{\sum_{\substack{\text{all}\\\text{rays}}} \left[\frac{b}{a} - \frac{b_0}{a_0}\right]^2} . \qquad \ldots (18)$$

Equations (17) and (18) enable the position of each ray in the focal plane to be evaluated and the aberrations are given by the difference between these and the central ray co-ordinates.

Thus equations (1), (3) through (18) enable the geometrical aberrations to be evaluated. Because of the choice of scanning parameters on the collimating mirror the resulting spot diagram in the focal plane is an indication of the intensity distribution in the image. By the variation of p and q one can investigate the focal conditions for different entrance slit points and therefore the suitability of curved slits in the spectrometer.

Apart from the equations already given there is also the necessity of evaluating the order of the spectral line of given wavelength that most nearly satisfies the grating blaze conditions and the corresponding angle of incidence γ. This is done by inserting the grating constant d, wavelength

λ, angle between the incident and diffracted beams, β, and blaze angle ϕ into the following expression and finding the nearest integer to the result:-

$$\frac{d}{\lambda} . \left[\sin(\phi - \beta/2) + \sin(\phi + \beta/2)\right] .$$

This integer, n, would correspond to the order of the wavelength λ which most nearly satisfies the blaze properties. Finally the angle of incidence, γ, is evaluated from:-

$$d.\left[\sin\gamma + \sin(\gamma + \beta)\right] = n.\lambda.$$

A further requirement is a means of image width evaluation. This is done by three methods. The extreme width of the distribution is found together with the width of the distribution for $z = 0$, i.e. neglecting the aberrated rays that end up out of the x-y plane of the instrument. Lastly, twice the root mean square deviation of the distribution from the centre of gravity of the spot diagram is evaluated which, as Hill (ref. 6) points out, would be the approximate half maximum intensity width of a single slit diffraction pattern.

A computer program has been written to evaluate the aberrations using the equations given previously and written in ALGOL to run on the NPL KDF9. With the aid of the graphical output system the aberrations are exhibited as a spot diagram in the focal plane and a histogram to show the density of points in the y direction (this has never actually been used for any quantitative analysis). Using the Kidsgrove translator the computations take approximately 20 seconds to trace 256 rays through the system and each graph takes about 5 minutes to be plotted on the incremental plotter.

Calculation of the input parameters

It is now necessary to calculate the specific input parameters required for the 1.5 m instrument being constructed at NPL. This is a Czerny-Turner system where both mirrors have the same radii of curvature and a high blaze angle plane grating is used. In the system shown in Figure 4 we start with the symmetrical Ebert form in which the centres of curvature of the two spherical mirrors are coincident. The grating is used as shown with the normal on the entrance slit side. This results in a smaller projected grating width in the direction of the observed diffracted beam and therefore

leads to a lower attainable theoretical resolution (the latter being proportional to the projected grating width). However, under the present conditions this loss is adequately offset by the gain in dispersion and reduction of scattered light on the exit slit side. The perpendicular distance between the entrance slit and the line joining the grating centre and the centre of curvature of the mirrors is made as small as possible and this appears to be approximately 100 mm. The position of the grating on this line has been examined analytically and the focal curves are given by Mielenz (ref. 9) for different grating positions. As a result of this it appears best to put the grating 1215 mm from the mirrors which would result in a flat focal plane in the dispersion direction and a not too curved one in the direction parallel to the grating rulings. This setting is not at all critical especially as long slits are not being used.

Starting with a symmetrical system means the exit to entrance slit distance is 200 mm. Also the off-axis angles of the mirrors are the same ($\theta = \psi$). From Figure 4 we obtain the following relations between the parameters shown:-

$$\tan \alpha = \frac{100 - x}{1500},$$

$$2\theta = \alpha + \beta/2,$$

$$\tan(\beta/2 - \theta) = \frac{x}{3000},$$

$$\tan \beta/2 = \frac{x}{1215}. \qquad \ldots (19)$$

The angles α, β and θ are small and therefore we can approximate the above equations (19) and solve to give:-

$$\beta = 7.548^{\circ},$$

$$\theta = \psi = 2.274^{\circ},$$

$$x = 81.1 \text{ mm}.$$

The perpendicular distance p0 between the entrance slit and collimator axis is given by:-

$$1500.\sin 2\theta$$

$$= 59.47 \text{ mm}.$$

N.B. The values given here are based on slightly more accurate approximations made by considering parallel illumination and astigmatic imaging but the resulting image is not significantly affected by such small changes. It must also be remembered that in practice most dimensions cannot easily be set with an accuracy better than 0.1 mm and therefore there is no point in calculations based on figures more accurate than this.

Distances d1 and d2 are assumed to be 1215.0 mm which again is sufficiently accurate. The aperture of the system is governed by the grating which for the present case is a 52° blaze angle Echelle grating with 309 lines/mm and would represent a rectangular aperture of 110 mm wide and 102 mm high (the width corresponds to the grating being used on blaze and with part masked off). The collimator to entrance slit distance, f, measured along the collimator axis is taken as 1497.6 mm for parallel illumination of the grating as defined by equation (2) and as a variable parameter when investigating other forms of illumination.

The entrance slit points were also variable parameters. The y co-ordinate (p) was usually set at 59.47 mm (equal to p0) unless curved slits were investigated. Object points corresponding to 0, 2 and 5 mm along the entrance slit were considered, the latter representing the aberrations expected at the ends of 10 mm long slits.

Optimising the off-axis angle of the focussing mirror for the 1.5 m Echelle spectrometer

A symmetrical in-plane Ebert single mirror spectrometer suffers from a comatic image produced as a result of the incident and diffracted beams of the grating being of unequal width. The ratio of the incident to diffracted beam width is:-

$$\cos\gamma/\cos(\gamma + \beta)$$

where γ and β have their previous meaning.

Using analytical techniques Rosendahl (ref. 10) finds that optimum image width can be obtained if the off-axis angles of the focussing and

collimating mirrors, given by ψ and θ respectively, satisfy the relation:-

$$\sin \psi.\cos^3(\gamma + \beta) = \sin \theta.\cos^3 \psi. \qquad \ldots (20)$$

This result is obtained from work by Shafer et al. (ref. 3) who analysed a Czerny-Turner system of two mirrors with the added degree of freedom of allowing the radius of curvature of the collimator, R_1, and the focussing mirror, R_2, to differ. They obtain:-

$$R_2 = R_1[\sin \psi.\cos^3(\gamma + \beta)/\sin \theta.\cos^3 \gamma].$$

Shafer et al. point out that complete reduction of comatic aberration cannot be obtained by keeping $R_1 = R_2$ and simply adjusting the off-axis angle of the focussing mirror. However, although this is true the effect of optimising R_2 is relatively small and will be neglected here.

Thus, as we have the values of θ, γ and β we can calculate the theoretical value of ψ which should given optimum reduction in coma. Let $\theta = 2.274^\circ$, $\beta = 7.548^\circ$ and $\gamma = 48.285^\circ$. The latter is obtained from the results of calculating the angle of incidence from the blaze properties of the grating for $\lambda 150.0$ nm (this corresponds to the 34th order). Substituting these values into equation (20) gives:-

$$\psi = 3.78^\circ.$$

The ray trace program was run in order to examine this result. Runs were made with differing off-axis angles ψ for the focussing mirror whilst all other parameters were kept constant. The three image width parameters discussed earlier were evaluated for an object at the centre of the entrance slit and these were used to find the optimum angle ψ; the results are shown in Table 1 (this also includes data for the other two object points of + 2 and + 5 mm along the slit). Figure 5 shows the spot diagrams obtained and Figure 6 gives a plot of distribution width versus ψ for the object at the centre of the entrance slit. We observe that a minimum width occurs at about 3.625° for two of the distribution width parameters and at a somewhat smaller value nearer 3.5° for the extreme width parameter. These values agree favourably with the value of 3.78° using Rosendahl's $\cos^3$ relation.

According to Chandler (ref. 4), using a ray-tracing program that he used to optimise a 4 m instrument, the off-axis angle ψ may not satisfy the Rosendahl $\cos^3$ relation for best imagery. Rouse et al. (ref. 7) and Reader (ref. 8) have shown that this is not true and the results given here seem to substantiate their view.

Curved slits

The optimisation process carried out to find the best off-axis angle of the focussing mirror was performed by considering the object at the centre of the entrance slit. However, in practice we need to use finite slit lengths and therefore computations were also performed for objects corresponding to + 2 and + 5 mm along the entrance slit. Examination of the resultant spot diagrams shown in Figure 5 and the co-ordinates of the central ray, i.e. the one that hits the collimator vertex, in the focal plane show two major effects:-

1) The central ray focus is curved when using a straight entrance slit.
2) There is considerable astigmatism which gives rise to an image whose overall tilt with respect to the entrance slit direction varies according to the position of the object point along the entrance slit.

Fastie (ref. 11) showed that, for a symmetrical Ebert system, both of these effects could be eliminated by the use of circular slits whose radius of curvature equals half the separation of the entrance and exit slits thus enabling long slits to be used. However, this assumes the residual coma in the system, due to the grating, is negligible, i.e. a low blaze angle grating is used or the angle between incident and diffracted beams is small. Ray trace results at $\psi = 2.274^\circ$ show that, for the system described, residual coma is rather large. Correction of the latter means that we have an asymmetrical Czerny-Turner spectrometer in which case it is not as easy to see how curved slits will correct for 1) and 2) above. The easiest way to examine the suitability of curved slits is to consider the two effects above and the resulting imaging using the ray tracing and any other information available.

Spectral line curvature

It is well known (refs. 11, 12, 13) that a diffraction grating used with finite slit lengths gives rise to curvature of the image of a straight entrance slit because the slit does not lie on an isochromatic curve. With

reference to Figure 1 it is easy to see that the angle of incidence on the grating for rays hitting the centre of the grating increases as the object point is moved up the entrance slit. Because each ray satisfies the grating equation we see that the image of a straight slit is curved. This was pointed out by Fastie (ref. 11) when considering a symmetrical Ebert configuration. It was found that the curvature is such as to be concave to increasing wavelength. Stroke (ref. 12) gives an expression for the deviation Δx, of the image obtained from a straight entrance slit, from a straight line image as:-

$$\Delta x \simeq - \frac{[\sin \gamma + \sin(\gamma + \beta)]}{\cos(\gamma + \beta)} \cdot \frac{h^2}{2f} \qquad \ldots (21)$$

where γ and β have their usual meaning defined previously, h is the height of the object point above the slit centre and f is the focal length of the focussing mirror. Note that we should not expect the deviation, Δx, and hence the spectral line curvature to vary with off-axis angle of the focussing mirror.

Substituting the ray tracing parameters into equation (21) we find:-

$$\Delta x \simeq - 9.34 \times 10^{-4} h^2 .$$

For $h = 2$ and 5 mm:-

$$\Delta x_2 = - 3.73 \ \mu m,$$
$$\Delta x_5 = - 23.34 \ \mu m.$$

From the ray tracing results for a symmetrical Ebert configuration the co-ordinates of the central ray in the focal plane give:-

$$\Delta x_2 = - 3.7 \ \mu m,$$
$$\Delta x_5 = - 23.0 \ \mu m,$$

and for an optimised off-axis angle of 3.625° for the focussing mirror we obtain:-

$$\Delta x_2 = - 4 \ \mu m,$$
$$\Delta x_5 = - 23 \ \mu m.$$

As might be expected these results show that the inherent spectral line curvature due to the grating is the same for a symmetrical Ebert configuration as for an asymmetrical Czerny-Turner where we only alter the focussing mirror off-axis angle and the two mirrors have the same radius of curvature.

Now Fastie (ref. 11) showed that circular slits, whose diameter equals the separation of entrance and exit slits, have the property, for a symmetrical Ebert configuration, that object points anywhere along the entrance slit all present the same angle of incidence to the grating. This gives rise to a direct image relation between entrance and exit slits. Because optimisation of the system does not alter the collimator-grating configuration, this being the important factor as pointed out by Shafer et al. (ref. 3), we expect the same curved slits to satisfy the Ebert and asymmetrical configurations. This is easily checked by observing the co-ordinates of the central ray in the focal plane when we consider the variation of the parameter p such that the object points lie on a circular entrance slit. The radius of curvature of the slits was calculated as being 100.2 mm but the value of 100 mm was adopted, the difference being negligible. Table 2 shows the shift of the object point in the y_1 direction and the calculated shift of the corresponding image in the y_5 direction using ray tracing for the central ray. Extremely good agreement is found which shows that circular slits satisfy the inherent spectral line curvature of the grating.

Astigmatism and divergent illumination of the grating

The second effect to be considered is that of astigmatism resulting from two spherical mirrors being used off-axis. This means that a single object point on the entrance slit is imaged to a straight line in the focal plane. The tilt of this image from the entrance slit direction increases as the entrance slit object point is moved away from the slit centre. Fastie (ref. 11) showed that, for a symmetrical Ebert, perfect imaging is obtained using circular slits of radius of curvature equal to half the separation of the entrance and exit slits, so that an object point on the entrance slit is imaged as a straight line tangential to the exit slit. The problem of imaging in a system where the focussing mirror is tilted to partially compensate for residual coma is that increased astigmatism arises (compare the ray trace results for $\psi = 2.274^\circ$ and 3.625° shown in Figure 5) and also the astigmatic image is not straight. We can study the overall form of the tilt of the astigmatic image from the ray trace and compare this with the

tilt of the corresponding point on a curved slit. This can be done for the symmetrical Ebert and asymmetrical Czerny-Turner configurations. Table 3 shows the results with the tilt given in radians and for slits of 100 mm radius of curvature. The slits are seen to fit the tilt obtained in the Ebert but not the asymmetrical Czerny-Turner. These results are only indications of the slope and do not represent the best line that could be drawn through the distribution.

Superimposing a negligible width exit slit on the ray trace spot diagrams will give useful information. The circular slits only deviate by 1 μm at each end of a 1 mm length from a straight slit. Thus it was assumed that the exit slit could be represented by a straight slit, of the correct tilt, over an individual spot diagram. The intensity contained by a band of width Y, defined in Table 1, and tilt corresponding to a 100 mm radius of curvature exit slit was evaluated for object points 0, + 2 and + 5 mm along the entrance slit. Also the extreme ray deviations on each side of the band were evaluated together with the overall extreme width. Careful examination of the results given in Table 1 shows that there is a loss of intensity in the central region for object points away from the entrance slit centre. There is also an asymmetry in the extreme rays for the optimum off-axis angle of 3.625°. Examination of the spot diagrams, Figure 5, shows that there would be some advantage in reducing the astigmatism.

Bates et al. (ref. 14) show that illumination of the grating in a divergent beam can be used to reduce astigmatism without degrading the spectral resolution, because the astigmatism introduced by the grating compensates for that of the two mirrors. Using the optimised focussing mirror off-axis angle of $\psi = 3.625^{\circ}$, various ray tracings were made for different values of the parameter f (the x co-ordinate of the entrance slit with respect to the collimator vertex in the subscript 1 system). The results are shown in Figure 7 for the three object points along the entrance slit. Table 4 gives the astigmatic image length and the root mean square width for the object at the centre of the entrance slit as a function of f. This shows that astigmatism can be reduced to negligible proportions at the expense of a marginal broadening in the central peak of the distribution for a value of f = 1478.0 mm. This corresponded to a re-focussing movement at the exit slit of 24 mm, from the parallel illumination focal plane, in a direction away from the focussing mirror. Using this value for f, three runs were made at $\psi = 3.25^{\circ}$, 3.50° and 3.75° in order to investigate any change in image width or symmetry. Analysis of these results on the same

lines as Table 1 shows that again optimum off-axis angle ψ seems to be nearer 3.50° as shown in Table 5. Also using divergent illumination corresponding to f = 1478.0 mm leads to a rather more symmetrical tail on the distribution especially for object points towards the ends of a 10 mm slit length. This has been obtained at the cost of a slight increase in the central peak width which may or may not be justifiable.

We can summarise the divergent illumination asymmetrical Czerny-Turner as follows:-

1) A stigmatic system can be obtained by illumination of the grating with a slightly divergent beam and re-focussing on the exit slit.
2) This results in a slight increase in central peak width.
3) The asymmetry of the distribution does not increase greatly with slit length.
4) The loss in intensity as a result of divergent illumination on a finite grating aperture and using bounded mirror surfaces is about 3%. This is approximately balanced by the gain as a result of the system being stigmatic.
5) 100 mm radius of curvature circular slits eliminate the inherent spectral line curvature. N.B. A straight entrance slit with a specially curved exit slit would also be acceptable here.

References

1. BRAHDE, R. Astrophysica Norvegica, 1964, 10, 1.
2. YOSHINAGA, H., OKAZAKI, B. and TATSUOKA, S. J. opt. Soc. Amer., 1960, 50, 437.
3. SHAFER, A.B., MEGILL, L.R. and DROPPLEMAN, L. J. opt. Soc. Amer., 1964, 54, 879.
4. CHANDLER, G.G. J. opt. Soc. Amer., 1968, 58, 895.
5. EGGERS, D.F. and PETERSON, M.A. Appl. Optics, 1969, 8, 589.
6. HILL, R.A. Appl. Optics, 1969, 8, 575.
7. ROUSE, P.E., BRIXNER, B. and KLINE, J.V. J. opt. Soc. Amer., 1969, 59, 955.
8. READER, J. J. opt. Soc. Amer., 1969, 59, 1189.
9. MIELENZ, K.D. J. Res. Nat. Bur. Stand. C, 1964, 68,(4), 205.
10. ROSENDAHL, G. J. opt. Soc. Amer., 1962, 52, 412.
11. FASTIE, W.G. J. opt. Soc. Amer., 1952, 42, 641, 647.
12. STROKE, G.W. Handbuch der Physik, 29, edited by S. Flügge, Berlin, Springer, 1967, 426.
13. KUDO, K. J. opt. Soc. Amer., 1965, 55, 150.
    MINKOWSKI, R. Astrophys. J., 1942, 96, 306.
    RUPERT, C.S. J. opt. Soc. Amer., 1952, 42, 779.
14. BATES, B., McDOWELL, M. and NEWTON, A.C. J. Phys. E: Sci. Instrum., 1970, 3, 206.

BM

Focussing mirror off-axis angle degrees	Position of object along entrance slit mm	R µm	Y µm	Percentage of rays in width Y	Extreme rays occur at*		Extreme width ⁄ µm
					- ve µm	+ ve µm	
2.274	0	18.4	27.5	94	0	15	42.5
	2		27.5	94	0	17	44.5
	5		27.5	93	0	21	48.5
2.8	0	13.1	19.2	94	0	12	30.7
	2		19.4	95	0	13	32.4
	5		19.0	93	0	15	34.0
3.25	0	9.7	13.4	91	4.5	8	25.6
	2		13.4	86	6	8	27.4
	5		13.2	79	10	9	32.4
3.50	0	8.7	12.0	86	9	4.5	25.5
	2		12.0	84	12	5	29.0
	5		12.0	75	16	5	33.0
3.625	0	8.6	11.3	84	12	3	25.5
	2		11.4	79	15	3	29.4
	5		11.2	68	19	5	35.2
3.75	0	8.7	11.4	82	14	1	25.5
	2		11.4	79	17	1	29.4
	5		11.0	70	22	3	36.0
4.0	0	9.7	11.8	80	18	0	29.6
	2		11.8	75	21	0	32.8
	5		11.7	63	27	1	39.7

R Twice the root mean square deviation of the distribution from the centre of gravity.

Y Width of the distribution at $z = 0$ in the spot diagram co-ordinates.

⁄ The extreme width for an object point at the centre of the entrance slit is taken directly from the ray focal plane co-ordinates whereas the others are taken from the spot diagrams.

* This refers to rays falling outside a band of width Y.

Table 1. Optimising parameters for a 1.5 m Czerny-Turner spectrometer. Results relating to objects 2 and 5 mm along the entrance slit correspond to 100 mm radius of curvature slits.

Position of object along entrance slit mm	$\theta = \psi = 2.274^{\circ}$ Ebert		$\theta = 2.274^{\circ}$, $\psi = 3.625^{\circ}$ Asym. Czerny-Turner	
	Shift of object µm	Shift of image ≠ µm	Shift of object µm	Shift of image ≠ µm
2	- 0.020	+ 0.020	- 0.020	+ 0.020
5	- 0.125	+ 0.125	- 0.125	+ 0.124

≠ The signs are a result of the imaging and co-ordinate system used.

Table 2. Relation between the shift of the entrance slit object point in the y_1 direction and its image in the y_5 direction for both the Ebert and asymmetrical Czerny-Turner spectrometers. The object shift is measured from a straight slit and the image shift is measured from a straight slit whose central point coincides with the image of the entrance slit. The results refer to the changes in the y co-ordinates of the central ray (from object point to collimator vertex) traced through the system.

Position of object along entrance slit mm	Curved slit tilt	Symmetrical Ebert tilt	Asymmetrical Czerny-Turner tilt
2	0.020	0.022	0.015
5	0.050	0.052	0.030

Table 3. Astigmatic image tilt for the Ebert and Czerny-Turner configurations as compared with the tilt of a curved slit of 100 mm radius of curvature.

Entrance slit to collimator distance f mm	R µm	Astigmatic image length ≠ µm
1497.62	8.6	540
1490.0	8.8	360
1485.0	8.9	230
1482.0	9.0	160
1480.0	9.1	105
1478.0	9.1	50
1476.0	9.2	50
1474.0	9.3	110

≠ This parameter represents the extreme image length. On a density of distribution basis the best value of f would be nearer to 1476:0 mm, but this represents a slightly worse value of R and therefore the value 1478.0 mm was accepted as being the best value.

Table 4. Astigmatic image length and root mean square width of the distribution as a function of collimator to entrance slit distance, f, for an object point at the centre of the entrance slit and the focussing mirror off-axis angle of 3.625°. Figure 7 shows the spot diagrams to which these results refer.

Off-axis angle of focussing mirror degrees	Position of object along entrance slit mm	R μm	Y μm	Percentage of rays in width Y	Extreme rays occur at		Extreme width μm
					- ve μm	+ ve μm	
3.25	0	9.7	13.5	89	7	7	27
	2	9.8	14.0	87	7	10	30
	5	10.6	15.5	86	6	14	34
3.50	0	9.0	15.0	95	9	3	27
	2	9.2	15.0	95	9	6	30
	5	10.1	15.0	92	10	10	34
3.75	0	9.5	12.0	82	16	0	28
	2	9.6	12.0	80	17	1	30
	5	10.5	12.0	75	18	4	34

R and Y are defined in Table 1.

Table 5. Optimising the off-axis angle of the focussing mirror for the 1.5 m Czerny-Turner spectrometer when the grating is illuminated in divergent light in order to reduce astigmatism. The value of f is 1478.0 mm and 100 mm radius of curvature slits are assumed.

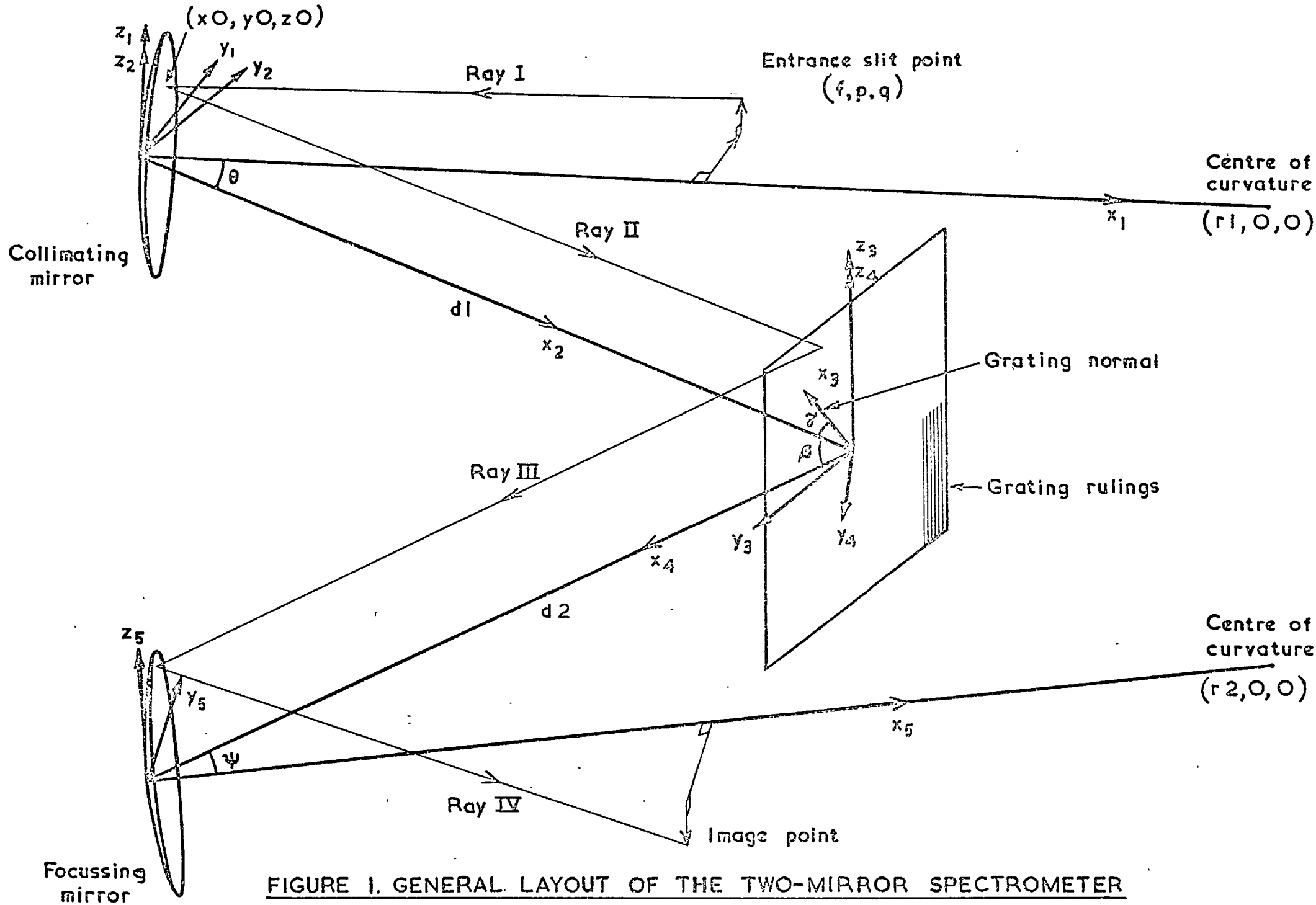

FIGURE 1. GENERAL LAYOUT OF THE TWO-MIRROR SPECTROMETER

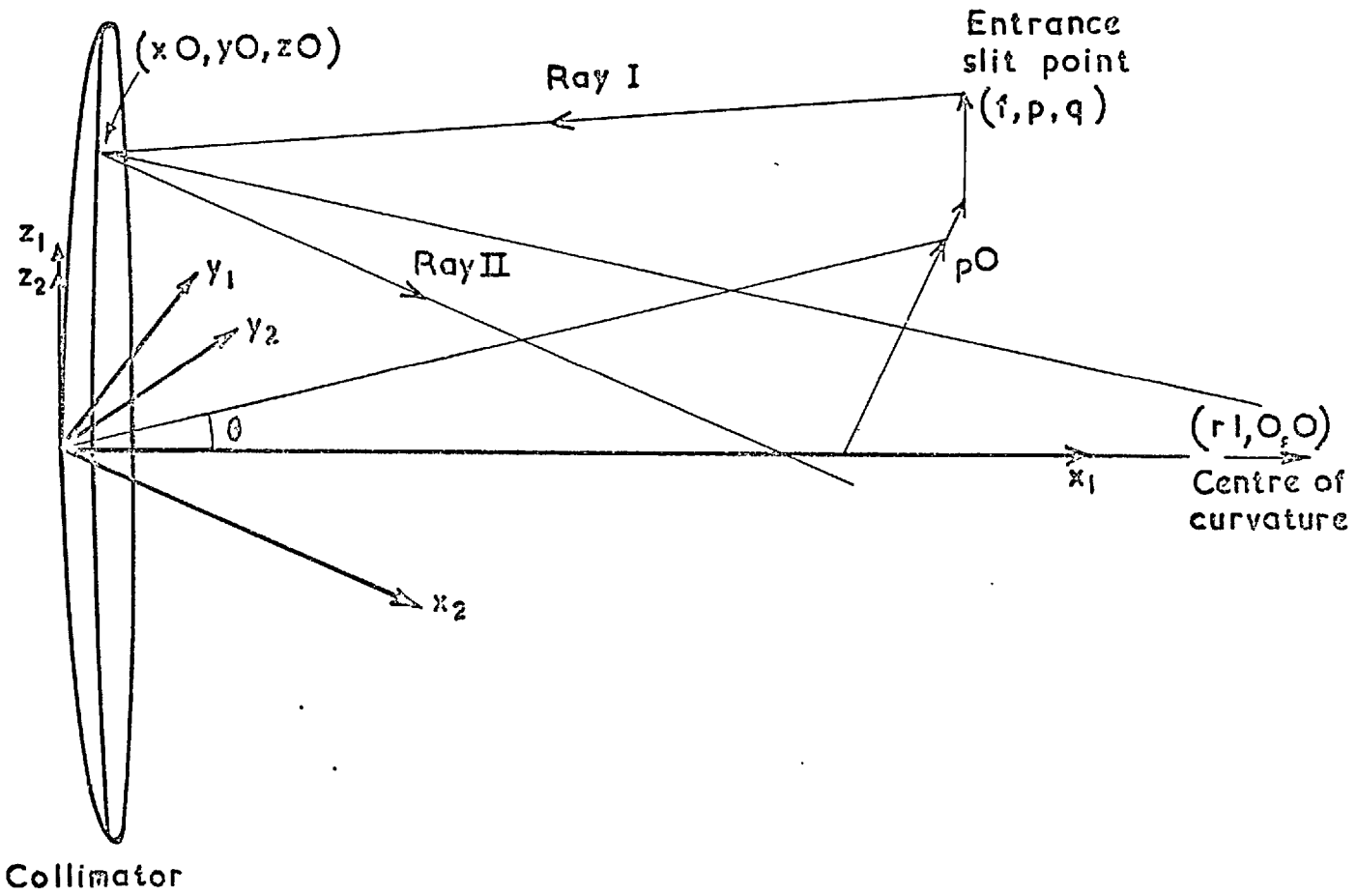

FIGURE 2. DETAILS OF THE COLLIMATOR

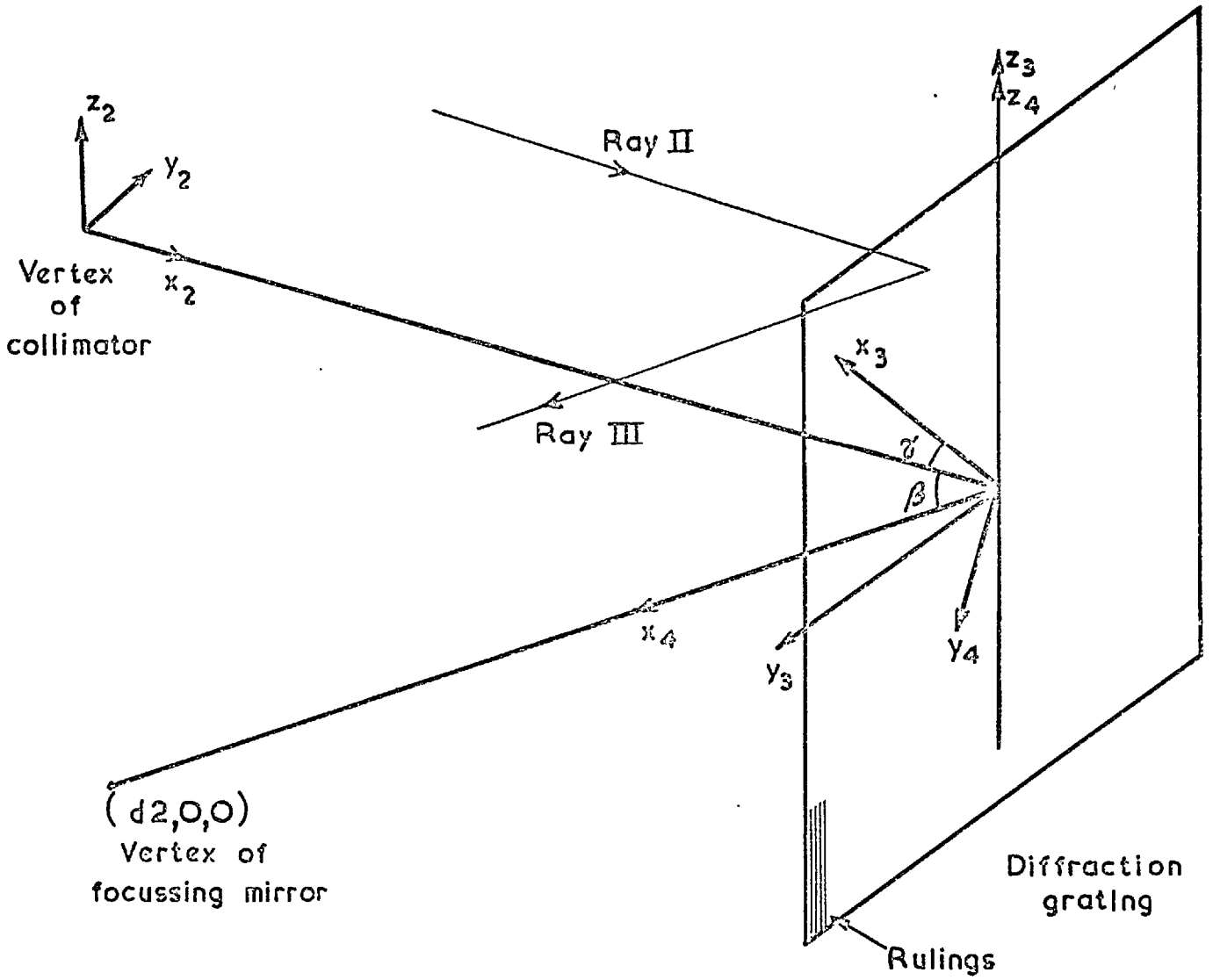

FIGURE 3. THE GRATING

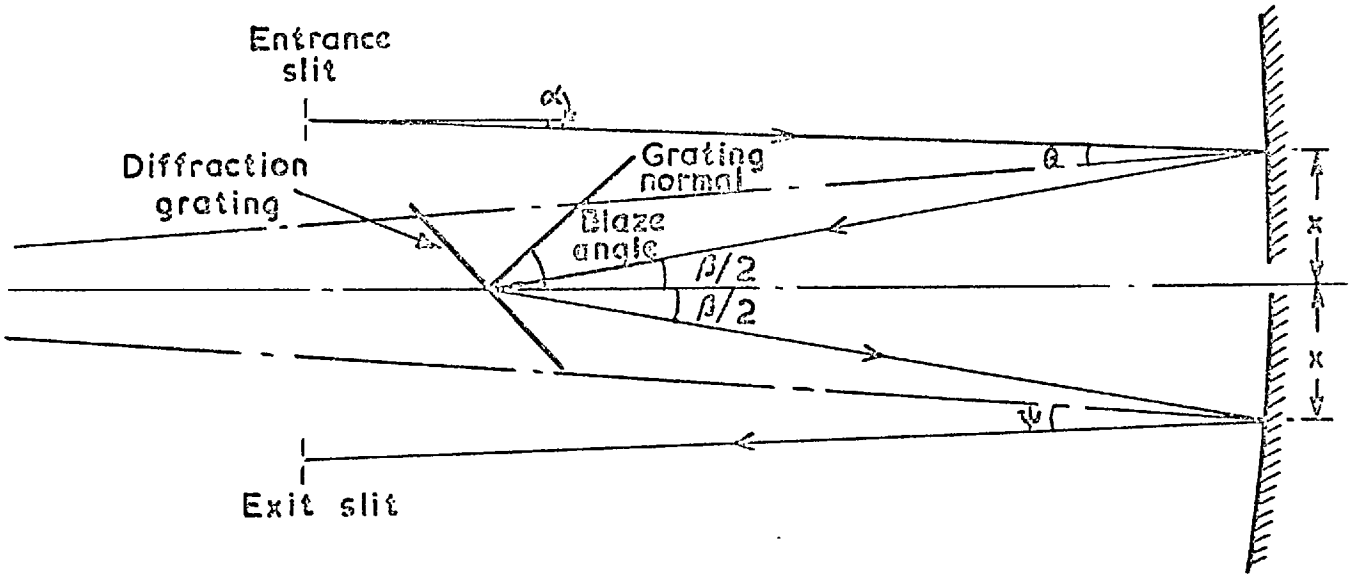

FIGURE 4. BASIC DESIGN PARAMETERS FOR THE LAYOUT OF THE SPECTROMETER

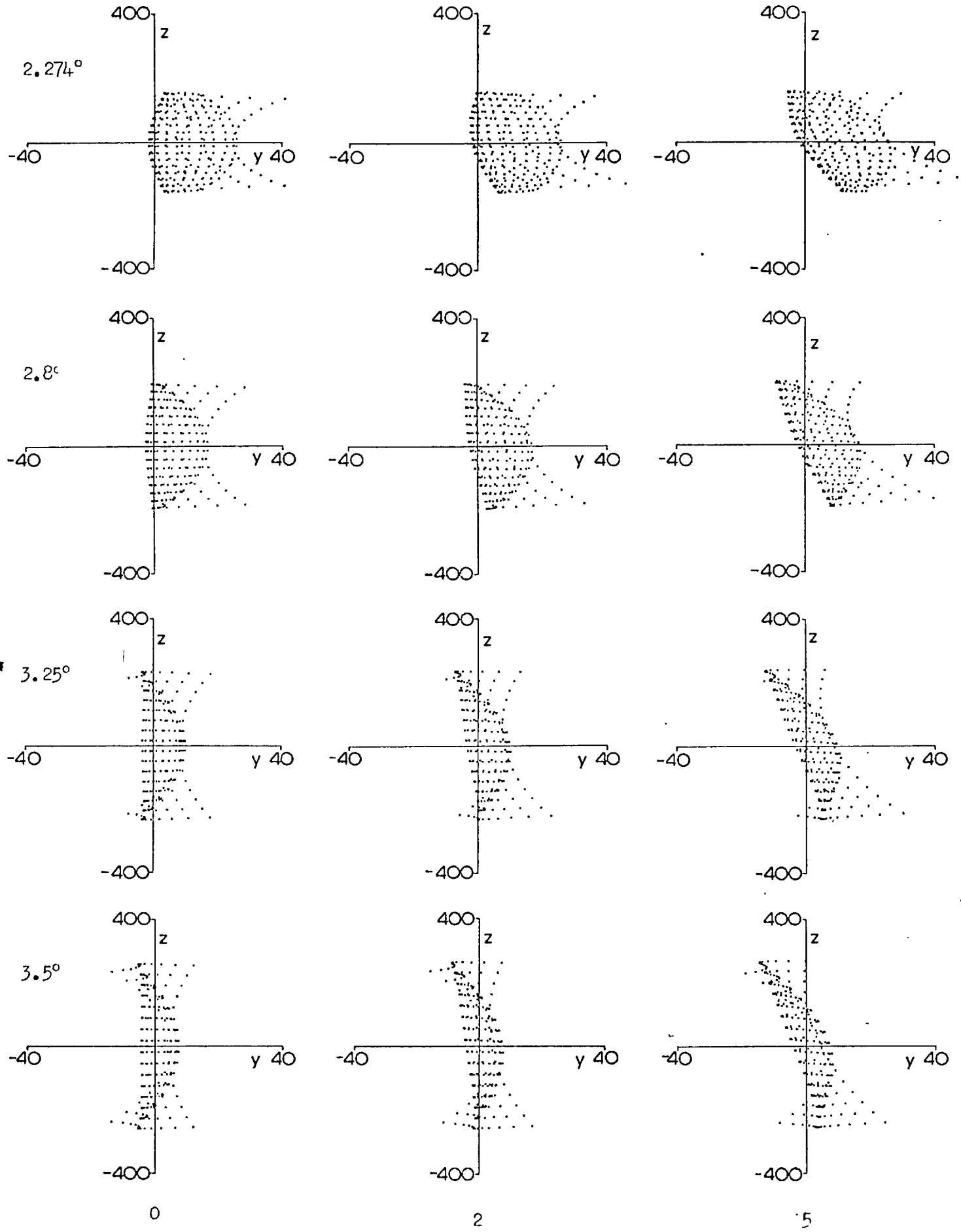

Figure 5. Ray tracing spot diagrams for the 1.5 m Echelle spectrometer showing the variation of image distribution with focussing mirror off-axis angle for three different object points along the entrance slit. Axes are marked in micrometres.

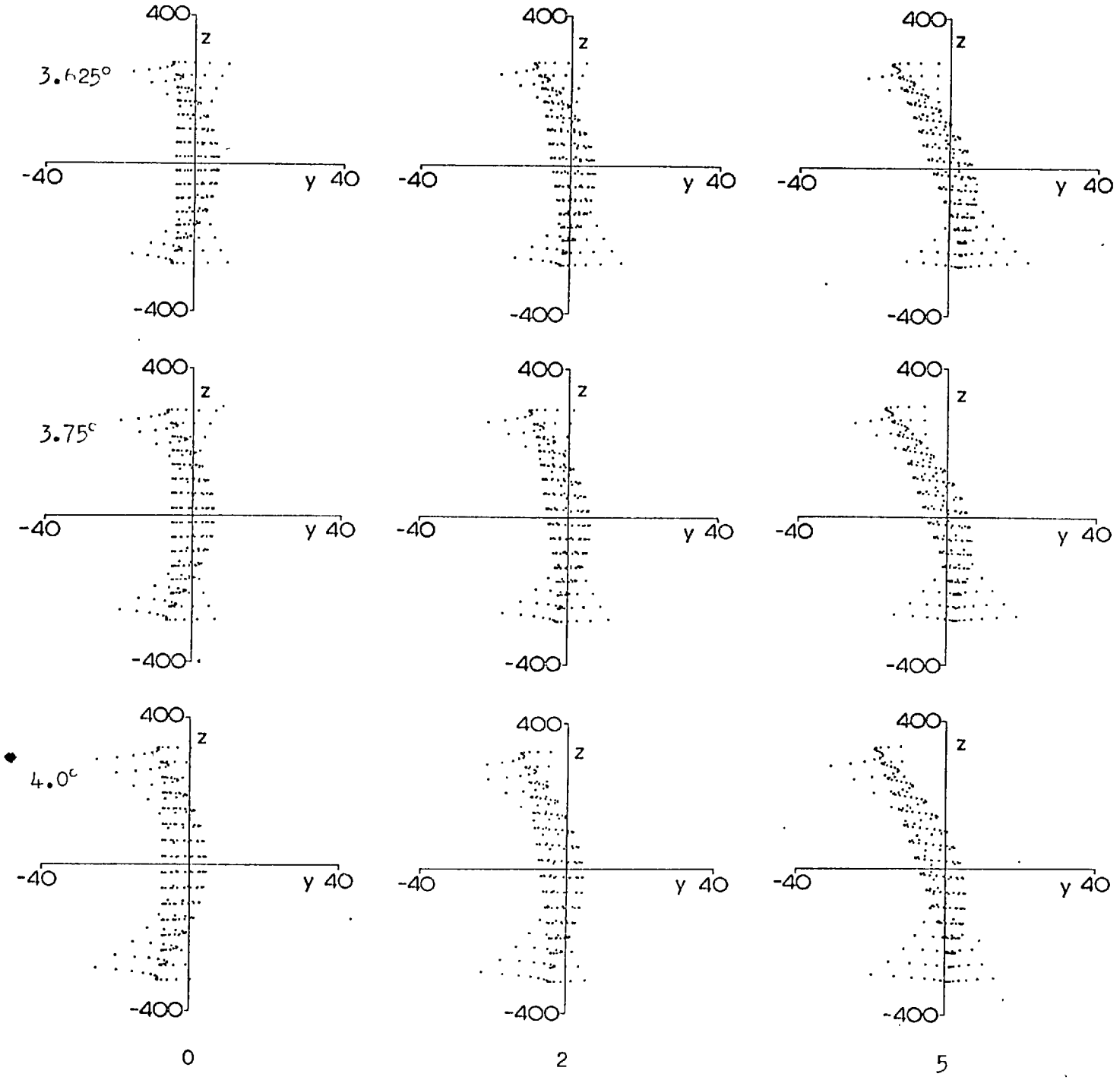

Position of object point along entrance slit in mm

Figure 5 (cont'd).

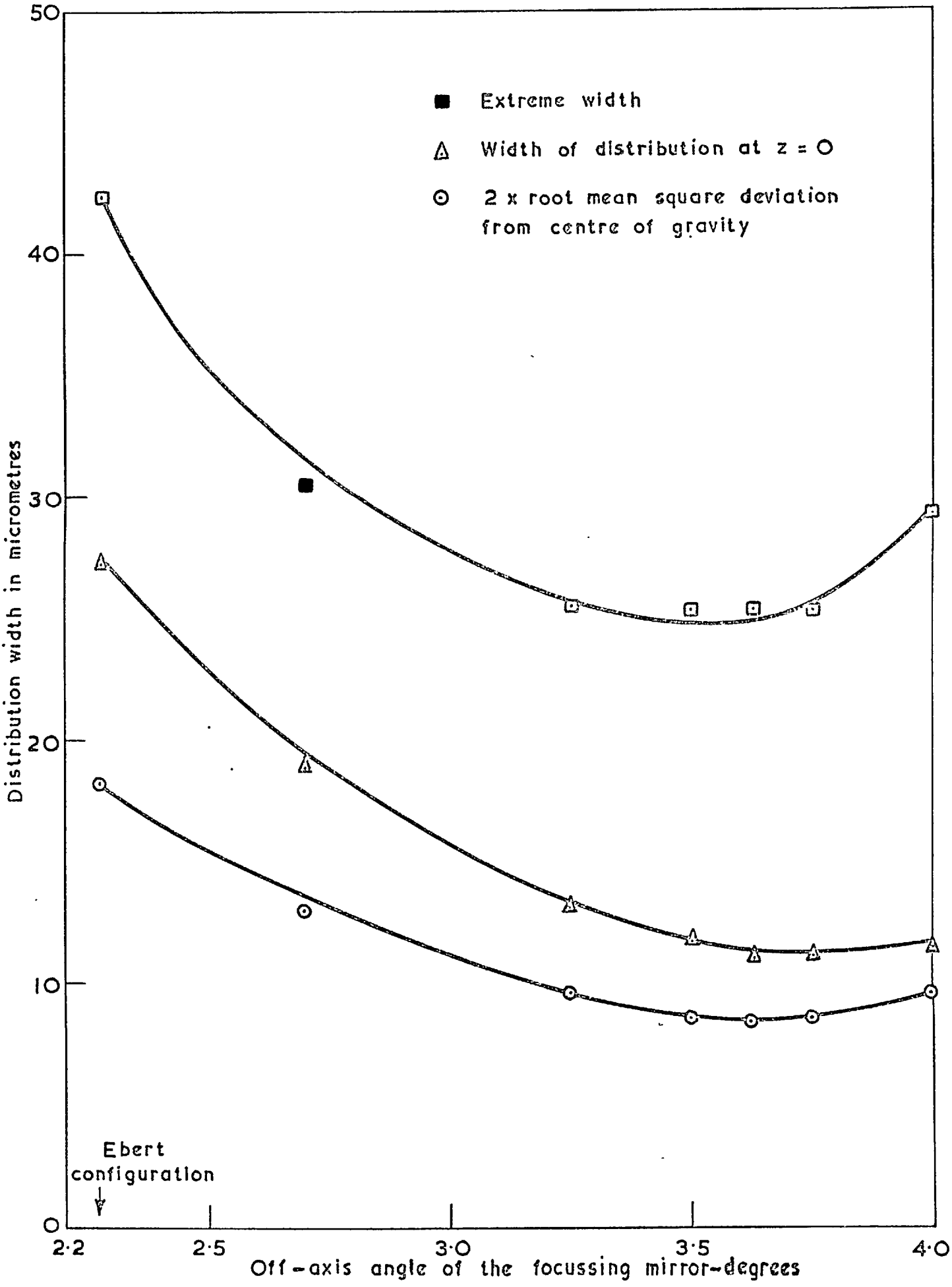

FIGURE 6. PLOT OF THE IMAGE DISTRIBUTION WIDTH FOR VARIOUS WIDTH EVALUATION PARAMETERS VERSUS THE OFF-AXIS ANGLE OF THE FOCUSSING MIRROR FOR AN OBJECT POINT AT THE CENTRE OF THE ENTRANCE SLIT

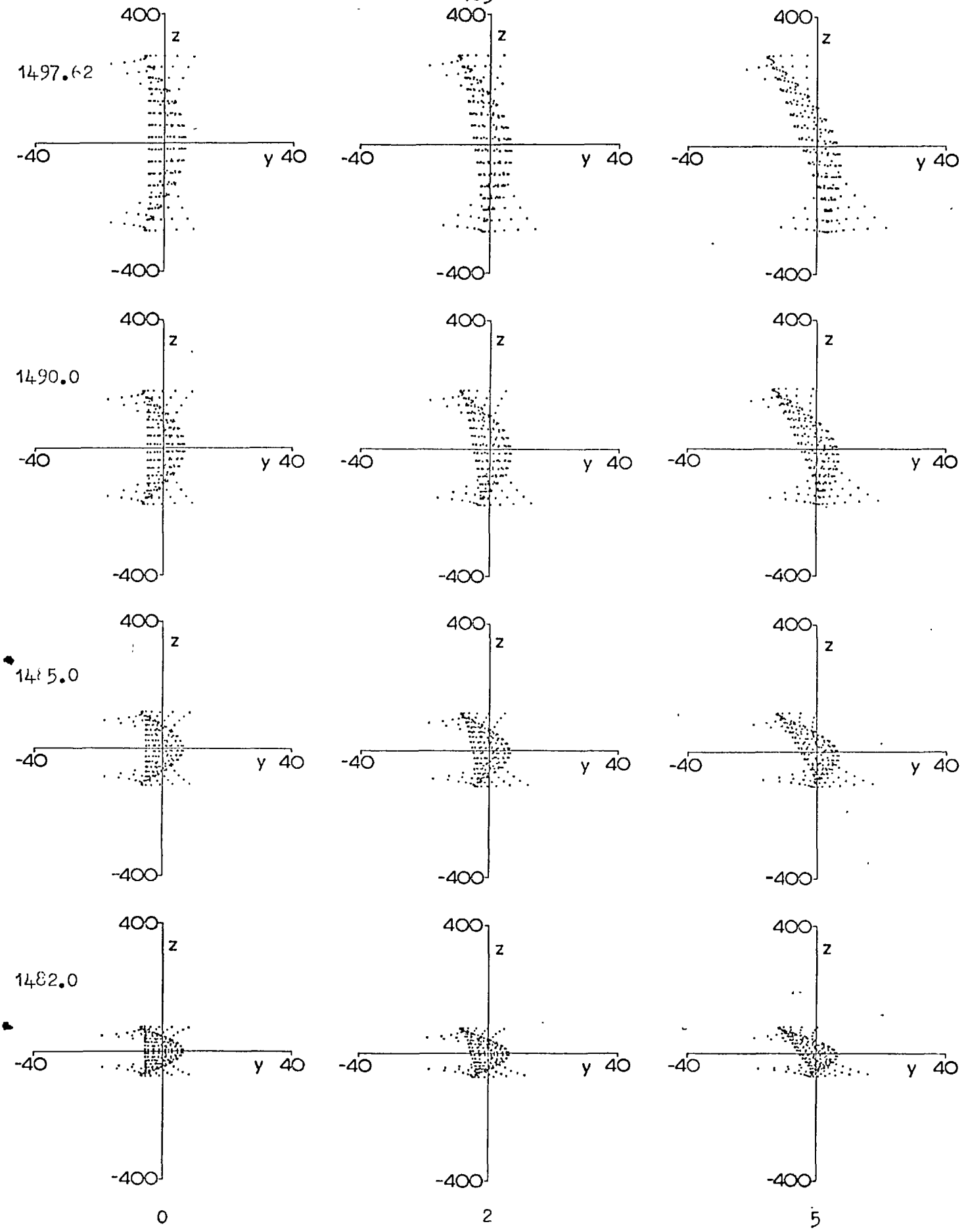

Position of object point along entrance slit in mm

Figure 7. Ray tracing spot diagrams showing the variation of astigmatic image distribution with entrance slit position, f, for three different object points along the entrance slit. Axes are marked in micrometres.

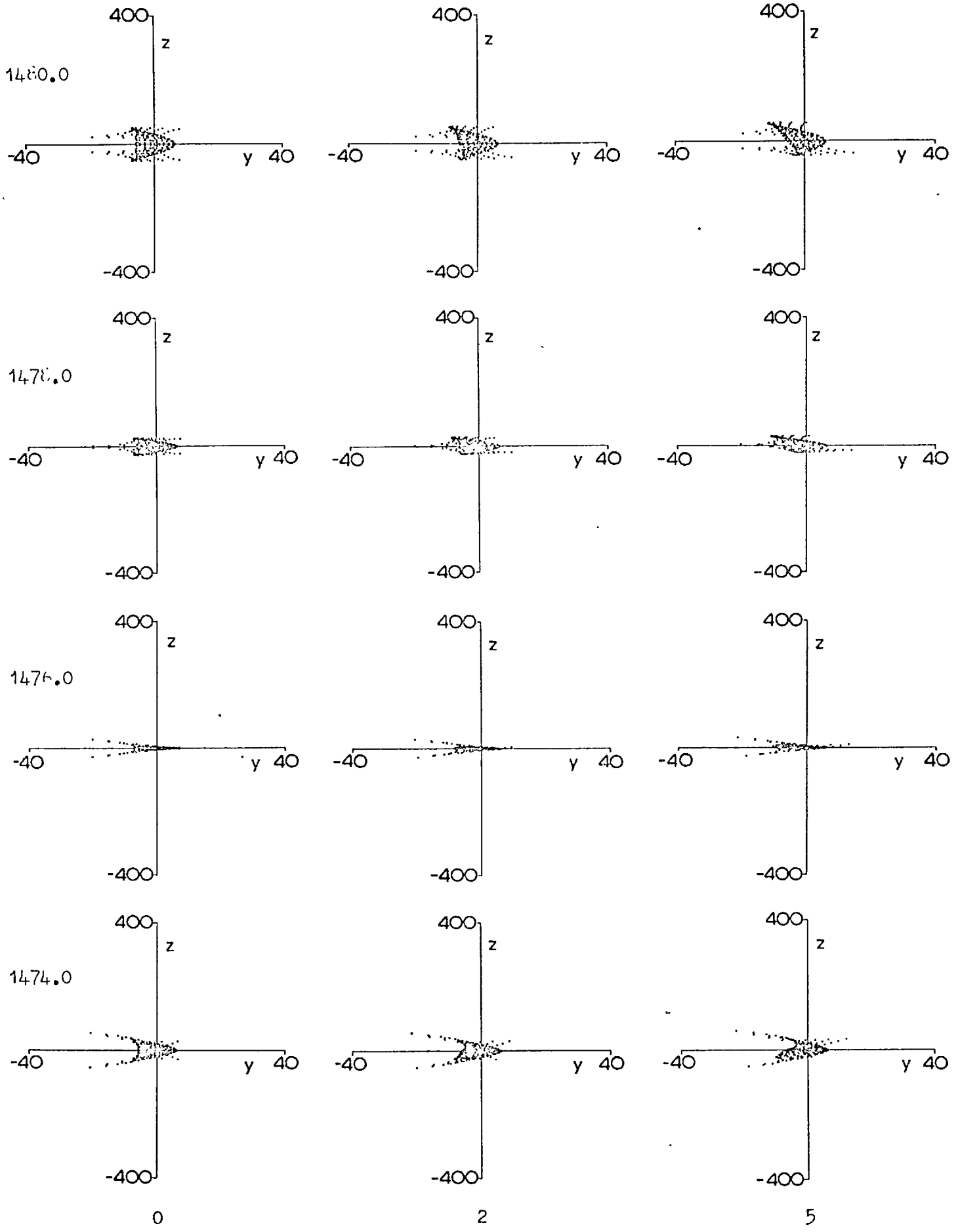

Position of object point along entrance slit in mm

Figure 7 (cont'd).

REFERENCES

Allen, C.W., 1955, Astrophysical Quantities, Athlone Press, London.

Andrew, K.L., Meissner, K.W., 1957, J. Opt. Soc. Am., 47, 850.

Andrew, K.L., Meissner, K.W., 1958, J. Opt. Soc. Am., 48, 31.

Andrew, K.L., Meissner, K.W., 1959a, J. Opt. Soc. Am., 49, 146.

Andrew, K.L., Meissner, K.W., 1959b, J. Opt. Soc. Am., 49, 1086.

Bacis, R., 1971, App. Opt., 10, 535.

Bacis, R., Danière, J., 1970, J. Phys. D., 3, 586.

Baranger, M., Mozer, B., 1961, Phys. Rev., 123, 25.

Bausch and Lomb Ltd., 1972, private communication.

Berry, H.G., Roesler, F.L., 1970, Phys. Rev. A., 1, 1504.

Borodin, V.S., Kagan, Yu. M., 1966, Zh. Tekhn. Fiz. [English translation:- Sov. Phys. - Tech. Phys., 1966, 11, 131].

Borodin, V.S., Kagan, Yu. M., Lyagushchenko, R.I., 1967, Zh. Tekhn. Fiz. [English translation:- Sov. Phys. - Tech. Phys., 1967, 11, 887].

Boyd, R.L.F., Twiddy, N.D., 1960, Proc. Roy. Soc., 259A, 145.

Cooper, J., 1966, Rep. Prog. Phys., XXIX, 35.

Czerny, M., Turner, A.F., 1930, Z. Phys., 61, 792.

Deverall, G.V., Meissner, K.W., Zissis, G.J., 1954, Phys. Rev., 95, 1463.

Ebert, H., 1889, Wiedem. Ann., 38, 489.

Edlén, B., 1963, Rep. Prog. Phys., XXVI, 181.

Fastie, W.G., 1952, J. Opt. Soc. Am., 42, 641.

Foley, H.M., 1946, Phys. Rev., 69, 616.

Freeman, G.H.C., Talim, S.P., 1970, N.P.L. Quantum Metrology Report No. 11.

Frish, S.E., Kagan, Yu. M., 1948, Zh. Eksp. Teor. Fiz., (Sov. Phys. J.E.T.P.), 18, 519.

Gartlein, C.W., 1928, Phys. Rev., 31, 782.

Gartlein, C.W., 1950, unpublished data supplied to C.E. Moore.

Griem, H., 1964, Plasma Spectroscopy, McGraw-Hill, New York.

Hannaford, P., 1972, J. Opt. Soc. Am., 62, 265.

Heilig, K., Reisner, D., Steudel, A., 1966, J. Opt. Soc. Am., 56, 1406.

Hindmarsh, W.R., Petford, A.D., Smith, G., 1967, Proc. Roy. Soc., 297A, 296.

Holtsmark, J., 1919, J. Ann. Phys., Lypz., 58, 577.

Humphreys, C.J., Paul, E., Jr., 1960, N.A.V.W.E.P.S. report No. 7157, 15; 1961, No. 7214, 23.

Jarrell, R.F., 1955, J. Opt. Soc. Am., 45, 259.

Jones, W.W., 1972, private communication.

Kaufman, V., Andrew, K.L., 1962, J. Opt. Soc. Am., 52, 1223.

Kaufman, V., Radziemski, L.J., Jr., 1966, J. Opt. Soc. Am., 56, 911.

Kaufman, V., Ward, J.F., 1966, J. Opt. Soc. Am., 56, 1591.

Kaufman, V., Minnhagen, L., 1972, J. Opt. Soc. Am., 62, 92.

Kaye, G.W.C., Laby, T.H., 1966, Tables of Physical and Chemical Constants, Longmans, London.

Kiess, C.C., 1940, J. Res. N.B.S., 24, 1.

Kreye, W.C., Roesler, F.L., 1970, J. Opt. Soc. Am., 60, 1100.

Kuhn, H.G., 1962, Atomic Spectra, Longmans, London.

Kuhn, H.G., Vaughan, J.M., 1964, Proc. Roy. Soc., 277A, 297.

Lang, R.J., 1928, Proc. Nat. Acad. Sci. U.S., 14, 32.

Lang, R.J., 1929, Phys. Rev., 34, 698.

Learner, R.C.M., 1968, J. Phys. E., 1, 589.

Lindholm, E., 1941, Ark. Mat. Astron. Fys., 28B, No. 3.

Lowe, R.M., 1972, private communication.

M.I.T. Wavelength Tables, 1939, John Wiley and Sons Inc., New York.

MacAdam, D.L., 1936, Phys. Rev., 50, 185.

Margenau, H., Lewis, M., 1959, Rev. Mod. Phys., 31, 569.

Medicus, G., 1965, J. App. Phys., 36, 435.

Meissner, K.W., Van Veld, R.D., Wilkinson, P.G., 1958, J. Opt. Soc. Am., 48, 1001.

Minnhagen, L., 1971, J. Opt. Soc. Am., 61, 1257.

Moore, Charlotte E., 1952, Atomic Energy Levels, N.B.S. (U.S.) Circ. No. 457, Vol. II.

Namioka, T., 1959, J. Opt. Soc. Am., 49, 446.

Patterson, H., Tomlin, D.H., 1962, Proc. Roy. Soc., 265A, 474.

Pery-Thorne, A., 1962, J. Quant. Spect. Rad. Trans., 2, 427.

Preston, R.C., 1970a, Optica Acta, 17, 857.

Preston, R.C., 1970b, J. Phys. E., 3, 737.

Preston, R.C., 1970c, N.P.L. Quantum Metrology Report No. 13.

Rao, K.R., 1929, Proc. Roy. Soc., 124A, 465.

Rao, K.R., Narayon, A.L., 1928, Proc. Roy. Soc., 119A, 609.

Radziemski, L.J., Jr., Andrew, K.L., 1965, J. Opt. Soc. Am., 55, 474.

Richter, C., 1928, Z. wiss. Phot., 25, 380.

Rowland, H.A., Tatnall, R., 1895, Astrophys. J., 1, 149.

Rowley, W.R.C., 1962, Com. Consult. Definition Metre, (Com. Int. Poids Mesures) 3^{e} session, 99.

Samson, J.A.R., 1967, Techniques of Vacuum Ultraviolet Spectroscopy, John Wiley, New York.

Shenstone, A.G., 1963, Proc. Roy. Soc., 276A, 293.

Stroke, G.W., 1967, Handbuch der Physik, 29, edited by S. Flügge (Berlin : Springer Verlag), 426.

Stuart, R.V., Wehner, G.K., 1964, J. App. Phys., 35, 1819.

Stuart, R.V., Wehner, G.K., Anderson, G.S., 1969, J. App. Phys., 40, 803.

Tako, T., Kōno, I., Ohi, M., 1962, Bull. Nat. Res. Lab. Metrology, Tokyo, 4, 1.

Van den Bosch, J.C., Klinkenberg, P.F.A., 1941, Proc. Ned. Akad. Wetensch. Amsterdam, 44, No. 5, 559.

Van Veld, R.D., 1951, M.S. thesis, Purdue university.

Van Veld, R.D., Meissner, K.W., 1956, J. Opt. Soc. Am., 46, 598.

Wilkinson, P.G., Andrew, K.L., 1963, J. Opt. Soc. Am., 53, 710.